First model independent measurement of the CKM angle γ using $B^{\pm} \to DK^{\pm}$ and $B^{\pm} \to D\pi^{\pm}$, $D \to 2\pi^{+}2\pi^{-}$ decays at LHCb

By

BENEDICT WESTHENRY

Department of Physics
UNIVERSITY OF BRISTOL

A dissertation submitted to the University of Bristol in accordance with the requirements of the degree of DOCTOR OF PHILOSOPHY in the Faculty of Science.

MAY 2023

Word count: 32,065

Abstract

The measurement presented in this thesis is that of the Cabibbo-Kobayashi-Maskawa (CKM) angle γ using $B^{\pm} \to D(\to 2\pi^{+}2\pi^{-})K^{\pm}$ and $B^{\pm} \to D(\to 2\pi^{+}2\pi^{-})\pi^{\pm}$ signal decays, where D represents the superposition of D^{0} and $\bar{D}^{0}$. A model independent approach is implemented for the measurement which utilises the distribution of signal events over the D meson decay phase space. The 2017 LHCb experiment dataset is used for the measurement. The CKM angle γ is determined to be $(38.8^{+30}_{-22})^{\circ}$. This is the first model independent measurement of the CKM angle γ in the $D \to 2\pi^{+}2\pi^{-}$ decay mode.

Dedication and acknowledgements

I would firstly like to thank my supervisor Jonas Rademacker. Your belief in me and support through the difficulties I've faced during my PhD, along with your constant enthusiasm and positivity have made a huge difference to my PhD experience. Your knowledge and expertise has been invaluable and I've thoroughly enjoyed our physics chats. I'm very grateful for the thesis feedback you provided to help improve and polish it. It has been a privilege to have you as my supervisor and I have learnt a great deal.

I would like to extend my thanks and appreciation to Claire Prouve for her mentorship, guidance and painstaking patience. You have more spent more hours than I can count helping and supporting me in a variety of different ways and I really cannot thank you enough. I am also enormously grateful to you for reading, rereading and rereading my thesis, often very quickly during unsociable hours and providing feedback in "Claire" level detail. I am very thankful to have had your support throughout my entire PhD.

I would like to thank Mark "the γ expert" Whitehead for his time, help and valuable input. I have no idea where you manage to store all the gems of (often niche) information that have helped me solve many of the issues I've been trying to work out. Your guidance and advice on all sorts of matters has been invaluable. Your ability to explain complex ideas in understandable formats is fantastic and has been a great help.

I feel incredibly lucky to have been able to have discussions with and input from the three truly astounding particle physicists above, and I am enormously grateful for the time and effort they have all dedicated towards helping me. They are all inspiring and I hope one day I can be at least a fraction as good a physicist as they are.

My thanks extends to the entire Bristol group for their support and friendship, particularly Richard and Lakshan and those in my cohort Sam E, David A and Nikos (looks like we might all make it!-touch wood), as well as my office mates over the years-Alex T, Srish, Sam MM , Esh, Florian, Rui and Charlotte (and Rob when he sits in his honorary chair)- and everlasting Briz LHCb members Kostas and Alex M, and students Jake R, Jake A and Jozie. Thanks to Kostas and Jozie for telling me to write my thesis- I hadn't thought of that, thank goodness you told me to. A nod to the "first years" Mei, Katie, Chris, Raul and Pieter for the pre-pandemic distractions. Thank you to Paras for offering his experience and advice when I've needed it. Thanks to David C, Keith and Magnus for their help when undertaking my work on TORCH. A special thank you to Martisse for brightening up my day whenever I am lucky enough to see her and being amazing in general.

I’ve also been lucky enough to make friends through the Data Intensive Sciences CDT and particularly thankful to my first year course buddies Virginia and Cale (who I also had a thoroughly enjoyable time on placement with at HIMR)- I wouldn’t have been able to get through the 1st year without you guys!- as well as Andrew. A big thanks to Ben H, Alex M, Steff H, Joel and Johannes for their help when us 1st years were very, very stuck. Another special thank you to Rosemary for all the administrative and moral support and always being very kind during times of high stress.

Thank you to the support from my non-particle physics friends particularly Callum and Amalia- the games nights with you have kept me sane during thesis writing- as well as Aaron and Charlie and my housemate in the first year of my PhD Lizzie.

Thanks to all those in the University of Bristol Athletics and Cross Country Society and Bristol Distance Project for keeping blood flowing to my brain and for nominating me for the University’s REDS Director’s award I received in 2022, I was very touched. It was one of the highlights of my time as a PhD student and it meant a great deal.

Thanks to Natalie, for being the most wonderful partner and supporting me through thick and thin during my PhD. Thank you for helping make the last few months of writing as stress free as possible and all the presentation feedback over the years, as well as proof reading my thesis. You’ve been a super helpful sounding board and provided unfaltering encouragement whenever I’ve needed it most. You’ve made life whilst undertaking a PhD (including through a pandemic) the most enjoyable.

Thank you to my loving family- Jan, Darren, Hannah and Siobhan- for supporting me through all my studies throughout my life and encouraging me to do the PhD in the first place. Thanks for being excited about my physics and listening to me explain my research even when you have no idea what I’m talking about.

AUTHOR'S DECLARATION

I declare that the work in this dissertation was carried out in accordance with the requirements of the University's Regulations and Code of Practice for Research Degree Programmes and that it has not been submitted for any other academic award. Except where indicated by specific reference in the text, the work is the candidate's own work. Work done in collaboration with, or with the assistance of, others, is indicated as such. Any views expressed in the dissertation are those of the author.

SIGNED: .... DATE: ....

Author's Contribution

The measurement presented in this thesis uses data collected by the LHCb experiment which is operated by the LHCb collaboration. The simulation samples are produced by the LHCb simulation group. The data and simulated samples have the LHCb software applied to it which is written by subgroups in the collaboration. A variety of subgroups within the collaboration have created, developed and maintained the detectors and software which have allowed this measurement to be performed. Some inputs used for this analysis have previously been measured by others within the collaboration, this is made clear within the thesis.

Chapters 4 to 9 detail the author's own work.

Table of Contents

Chapter 1

Introduction

The Standard Model of particle physics is one of the most successful and tested theories in physics. Particle physics experiments have been able to verify a wide range of predictions from the Standard Model, including the existence of the $W^{\pm}$ and Z^0 bosons, and the Higgs boson which was discovered by the CMS [1] and ATLAS [2] experiments forty years after its prediction.

Nonetheless, there are a multitude of phenomena the Standard Model does not provide an explanation for. The Standard Model does not include a formalism for gravity or explain the hierarchy of the fundamental interactions. Nor is there any way to account for dark matter and dark energy within the Standard Model. Of particular relevance to this thesis is the lack of explanation as to why the Universe contains a far greater amount of matter than antimatter. This extent of matter antimatter asymmetry observed in the Universe is not accounted by the source of charge-parity (CP) violation in the Standard Model.

Therefore, determining the CP-violating quantities within the Standard Model precisely is one of the key aims of flavour physics [3]. The CKM angle γ within the Unitary Triangle corresponds to the CP violating phase of $b \to u$ quark transitions [4] [5]. The analysis presented in this thesis is the model independent measurement of the CKM angle γ using $B^{\pm} \to DK^{\pm}$ decays and $B \to D\pi^{\pm}$ decays, with $D \to 2\pi^{+}2\pi^{-}$, where the the four pion final state is accessible to both the D^0 and $\bar{D}^0$ mesons. The CKM angle γ can be measured through the interference between $b \to u$ and $b \to c$ quark transitions in these decay channels. The decays are dominated by tree-level diagrams. Thus, $B^{\pm} \to DK^{\pm}$ decays can be very cleanly related to the underlying Standard Model parameter γ with a negligible theoretical irreducible error [6]. Consequently, measurements of the CKM angle γ using $B^{\pm} \to DK^{\pm}$ decays are pivotal to over-constraining the Unitary Triangle which is a key test of the consistency of the Standard Model. Moreover, it is a widely held view that tree diagrams are unlikely to be affected by New Physics whilst the contrary is expected in loop diagrams. However, it has been indicated that sizeable New Physics at tree level is also possible [7] [8]. Beyond Standard Model effects are likely to manifest differently in tree and loop diagrams, therefore comparing the differences in the results of the CKM angle γ between these methods could provide interesting insights. The sensitivity to γ can be improved by dividing the phase space of self-conjugate four pion final state into bins, and integrating over each bin. The parameters that are related to the D decay amplitudes across the five-dimensional phase space are a source of systematic uncertainty on γ . This uncertainty can be avoided by instead defining model independent parameters which can be measured separately. This is the first time the CKM angle γ has been measured in the $D \to 2\pi^+2\pi^-$ mode using this model independent approach.

This thesis is organised as follows:

- Chapter 2 provides an overview of the theory used for this analysis, including direct CP violation in the Standard Model, with particular focus on the CKM matrix and its CP violating phase γ. The chapter explains how the CKM angle γ can be measured through interference of $B^\pm \to D(\to 2\pi^+2\pi^-)h^\pm$ decays, where D represents the superposition of D^0 and $\bar{D}^0$, and $h^\pm$ is either $K^\pm$ or $\pi^\pm$. The formalism of the model independent approach is also outlined.

- Chapter 3 introduces CERN and the LHCb experiment and briefly explains the composite elements of the LHCb detector, and how they are involved in reconstructing particle tracks and identifying particle types.

- Chapter 4 describes a sensitivity study to establish the approximate sensitivity to the CKM angle γ achievable when measuring γ with the model independent method, using $B \to D(\to 2\pi^+2\pi^-)K$ decays at the LHCb experiment.

- Chapter 5 details the selections and background studies used in this analysis.

- Chapter 6 explains the simultaneous invariant global mass fit to $B^\pm \to D(\to 2\pi^+2\pi^-)K^\pm$ and $B^\pm \to D(\to 2\pi^+2\pi^-)\pi^\pm$ LHCb data, which is used to fix the shapes used for the probability density functions in the subsequent fit for the CP observables.

- Chapter 7 outlines the implementation of the simultaneous fit for the CP observables to $B^\pm \to D(\to 2\pi^+2\pi^-)K^\pm$ and $B^\pm \to D(\to 2\pi^+2\pi^-)\pi^\pm$ LHCb data across the four pion phase space bins, and details the CP observable results.

- Chapter 8 details the γ measurement extrapolated from the CP observable results.

Chapter 2

Theory

2.1 The Standard Model of Particle Physics

The Standard Model of particle physics[1] is a quantum field theory with a specific particle content and a particular symmetry group. Fermions and bosons describe all the matter and its physical interactions within the Standard Model.

Fermions have half integer spin and contain groups of particles known as leptons and quarks which are split into 3 generations according to mass. All lepton generations have an neutrino-type and electron-type particle with charges 0 and -1 respectively, whereas the quark generations have an down-type quark of charge -1/3 and a up-type quark of charge +2/3. Quarks experience the strong interaction, unlike leptons, and thus carry colour charge too. Table 2.1 summarises the fundamental fermion particles.

Bosons have integer spin and are the force carriers responsible for the electromagnetic, weak and strong interactions in the Standard Model. All three of these interactions must obey the conservation laws for example energy conservation and charge conservation.

All particles with non-zero charge can take part in the electromagnetic interaction which is mediated by photons. Photons are massless and without charge. The electromagnetic interaction is invariant under parity transformation P and charge conjugation C and is described by the $U(1)$ symmetry group.

[1] The Standard Model of Particle Physics section is based on References [9], [10], [11], [12] and [13].

Table 2.1: The Standard Model's fundamental fermions divided into quarks and leptons. Each particle also has a corresponding anti-particle with reverse additive quantum numbers and identical mass. Table inspired by Reference [11].

Fermions						
	Leptons			Quarks		
Generation	Type	Charge	Mass	Type	Charge	Mass
1	ν_e	0	< 2 eV/c^2	u	+2/3	2.3 MeV/c^2
1	e^-	-1	511.0 eV/c^2	d	-1/3	4.8 MeV/c^2
2	ν_μ	0	< 2 eV/c^2	c	+2/3	1.28 GeV/c^2
2	μ^-	-1	105.7 MeV/c^2	s	-1/3	95 MeV/c^2
3	ν_τ	0	< 2 eV/c^2	t	+2/3	173.5 GeV/c^2
3	τ^-	-1	1.78 GeV/c^2	b	-1/3	4.18 GeV/c^2

The neutral Z^0 boson as well as charged W^+ and W^- bosons mediate the weak interaction. The $W^\pm$ bosons have masses of 80 GeV/c^2 and the Z^0 boson has a mass of 91 GeV/c^2 and this results in the relative lack of strength of the weak interaction, compared to electromagnetic and strong interactions which are mediated by massless bosons. All fermions are able to undergo the weak interaction as they carry weak charge. The $W^\pm$ boson only couples to the left-handed fermion chiral states, whilst the Z^0 boson couples to both the chirality left-handed and chirality right-handed parts of all fermions with varying strengths. Consequently, the charged weak interaction maximally violates both charge conjugation and parity and is charge parity (CP) violating which is discussed further in Section 2.2. The weak interaction symmetry group is $SU(2)_L$.

The unification of the electromagnetic and weak interaction results in the electroweak interaction which is described by the $SU(2)_L \otimes U(1)_Y$ symmetry group. The spontaneous symmetry breaking of the electroweak symmetry group results in the Higgs boson, which has spin 0 and mass 125 GeV/c^2, and its corresponding Higgs field. The non-zero vacuum expectation value of the Higgs field yields to spontaneous symmetry breaking of the electroweak group leading to non-zero masses of the $W^\pm$ and Z^0 bosons. Furthermore, the Yukawa interactions between the Higgs field and the fermions leads to the masses of the fermions.

Lastly, eight massless gluons mediate the strong interaction. Only quarks (and gluons) participate in the strong interaction since they carry colour charge. However, the strength of the strong interaction becomes weaker at higher energy scales or equivalently as the quarks get very close together, this is known as asymptotic freedom. Moreover, gluons and quarks are exclusively bound together as hadrons since only objects with zero colour charge can exist because of a property called color confinement. The strong interaction is invariant under parity transformation P and charge conjugation C. However, it should be noted that the strong interaction Lagrangian contains a CP violating term. Experimental evidence suggests that this is zero, or at least extremely small, but it is not understood why this is so. This is known as the "strong CP problem." The strong interaction symmetry group is $SU(3)_C$.

The weak, electromagnetic and strong interactions properties are summarised in Table 2.2, and the combination of the 3 interactions describes the Standard Model symmetry group $SU(3)_C \otimes SU(2)_L \otimes U(1)_Y$.

Table 2.2: The fundamental interactions of the Standard Model. The lifetime is the order of the lifetime of particles that decay through the interaction in question. The cross section is the order of the cross section for the decays that proceed through the interaction in question. Table inspired by Reference [11].

Interaction	Relative Strength	Lifetime	Cross Section	Source	Force Carrier	Mass
Strong	1	10^{-23}s	10mb	colour charge	8 gluons	0
Electromagnetic	1/137	10^{-20}s	10μb	electric charge	photon	0
Weak	10^{-6}	10^{-10}s	10pb	weak charge	$W^{\pm}$	80 GeV/c^2
Weak	10^{-6}	10^{-10}s	10pb	weak charge	Z^0	91 GeV/c^2

The Standard Model of particle physics is widely regarded as highly successful, and experimentalists are still verifying Standard Model predictions. Recent examples include the discovery of the Higgs boson. However, the Standard Model does have multiple flaws. The final fundamental force, gravity, is not accounted for in the Standard Model. Moreover, there is no explanation for the cause of dark matter and dark energy or interactions with them. Nor is there a reason for three generations of quarks and leptons and it does not predict values for 21 independent parameters including the fermion masses, the Z^0 mass, the Higgs mass, coupling constant values, the mixing angles and the CP violating phase of the CKM matrix γ. Most pertinent to the analysis is the extent of the matter antimatter asymmetry in the Universe, which is not fully accounted for by the CP violation currently described in the Standard Model.

2.2 CP violation in the Charged Weak Interaction

There are three discrete space-time symmetries relevant to this thesis [11]:

- The charge conjugation operator C: converts a particle to its anti-particle by inverting the sign of all internal quantum numbers such as electric charge $Q \to -Q$.
- The parity operator P: inverts the spatial coordinates of a physical system $\mathbf{x} \to -\mathbf{x}$ but leaves axial vectors unchanged.
- The time inversion operator T: inverts the time coordinate $t \to -t$.

The CPT theorem [14] relates these three symmetries and requires any Lorentz-invariant Quantum Field Theory (QFT) to be symmetric under the application of all three operators at once. This does not mean that C, P and T symmetries cannot be broken independently, in fact it has been demonstrated experimentally that they are [15] [16] [17] [18] [19] [20] [21].

The application of the parity operator P followed by the charge conjugation operator C results in the charge-parity CP transformation. The CP transformation is discrete since both the C and P operators are discrete transformations themselves. The electromagnetic and strong interactions are both charge and parity invariant and therefore also CP invariant. However, the charged weak interaction maximally violates C and P . The CP violating phase within the CKM matrix means CP violation occurs within the charged weak interaction [9]. This is discussed further in Sections 2.2 and 2.3.

One of the key problems in the Standard Model of particle physics is the matter anti-matter asymmetry in the Universe [22]. CP violation accounted for in the Standard Model indicates a matter anti-matter asymmetry several orders of magnitude smaller than that which we observe in the Universe [23]. This indicates that CP violation needs to be accounted for by physics beyond the Standard Model. Therefore, it is critical to undertake CP violation measurements such as the measurement of CKM angle γ to determine if there are any indications of deviations from the Standard Model.

2.2.1 Direct CP Violation in the SM

As introduced in Section 2.1 there are three generations of up-type quarks (u, c, t), generalised as p, and the down-type quarks (d, s, b), generalised as q, described within the SM. The charged weak interaction of the $W^{\pm}$ boson couples up-type quarks and the down-type quarks. The corresponding quark states that couple to the $W^{\pm}$ boson labelled (u', c', t'), generalised as p', and (d', s', b'), generalised as q', are different to the mass eigenstates. A basis for the quark states can be used such that $(u, c, t) = (u', c', t')$ which defines (d', s', b') as $SU(2)$ partners of (u, c, t). The transformation from down-type quark q to q' [5] [4] [11] is

$$\begin{pmatrix} d' \\ s' \\ b' \end{pmatrix} = V_{CKM} \begin{pmatrix} d \\ s \\ b \end{pmatrix} = \begin{pmatrix} V_{ud} & V_{us} & V_{ub} \\ V_{cd} & V_{cs} & V_{cb} \\ V_{td} & V_{ts} & V_{tb} \end{pmatrix} \begin{pmatrix} d \\ s \\ b \end{pmatrix} \tag{2.1}$$

where V_{CKM} is the CKM matrix discussed in further depth in Section 2.3.

Hence, transformation from the adjoint down-type quark $\bar{q}$ and the adjoint up-type quark $\bar{q}'$ is

$$\begin{pmatrix} \bar{d}' & \bar{s}' & \bar{b}' \end{pmatrix} = \begin{pmatrix} \bar{d} & \bar{s} & \bar{b} \end{pmatrix} V_{CKM}^{\dagger}. \tag{2.2}$$

The charged weak current for an down-type quark transitioning to an up type quark and W^- boson via $q \to pW^-$ is

$$j^{\mu} \propto \bar{p}\gamma^{\mu}\frac{1}{2}(1-\gamma^5)q'. \tag{2.3}$$

Given Equation 2.1 it is possible to write the charged weak current for the $b \to uW^-$ transition as

$$j^{\mu}_{bu} = \bar{u}\left(-i\frac{g_W}{\sqrt{2}}\gamma^{\mu}\frac{1}{2}(1-\gamma^5)\right)V_{ub}b \tag{2.4}$$

where g_W is the weak coupling constant, γ^{μ} are the Dirac matrices and γ^5 is the product of the Dirac matrices multiplied by the imaginary number i, $\frac{1}{2}(1-\gamma^5)$ is known as the chirality left-handed projection operator P_L. The P_L operator provides the chirality left-handed component of a fermion. Consequently, only chirality left-handed components of fermions take part in the charged weak interaction. Similarly, according to Equation 2.4 the charged weak current for the $\bar{b} \to \bar{u}W^+$ transition is

$$j^{\mu}_{\bar{b}\bar{u}} = j^{\mu}_{ub} = \bar{b}V^*_{ub}\left(-i\frac{g_W}{\sqrt{2}}\gamma^{\mu}\frac{1}{2}(1-\gamma^5)\right)u \tag{2.5}$$

Therefore, if the CKM matrix was real, the vertex factors $\mathcal{V}_{bu}$ and $\mathcal{V}_{\bar{b}\bar{u}}$ would be equal to each other since

$$\mathcal{V}_{bu} = \left(-i\frac{g_W}{\sqrt{2}}\gamma^{\mu}\frac{1}{2}(1-\gamma^5)\right)V_{ub} \tag{2.6}$$

$$\mathcal{V}_{\bar{b}\bar{u}} = V^*_{ub}\left(-i\frac{g_W}{\sqrt{2}}\gamma^{\mu}\frac{1}{2}(1-\gamma^5)\right) \tag{2.7}$$

however, the CKM matrix has a complex phase thus, the vertex factors differ from one another and the charged weak interaction violates CP.

2.3 CKM Matrix

The CKM matrix describes the mixing of the three generation of quarks, when they undergo transitions taking place via a flavour-changing charged weak current mediated by a charged $W^{\pm}$ boson. As stated in Section 2.2.1 the generic form of the CKM matrix is

$$V_{CKM} = \begin{pmatrix} V_{ud} & V_{us} & V_{ub} \\ V_{cd} & V_{cs} & V_{cb} \\ V_{td} & V_{ts} & V_{tb} \end{pmatrix}, \tag{2.8}$$

where the CKM matrix element V_{pq} is proportional to the transition amplitude of a up-type quark p changing flavour to an down-type quark q. Conversely, the complex conjugate of the CKM matrix element V^{*}_{pq} is proportional to the transition amplitude of a anti up-type quark $\bar{p}$ to an anti down-type quark $\bar{q}$.

The CKM matrix is a three-dimensional, complex, unitary matrix, thus it has $3^2 = 9$ free, real parameters. However, the matrix only has four independent real parameters since five of the nine parameters can be absorbed into the non-physical phases of the quark mass eigenstates and weak eigenstates. The four remaining real parameters are the three mixing angles between the quark generations and a sole complex phase, which is responsible for direct CP violation in the Standard Model as discussed in Section 2.2.

2.3.1 CKM Matrix Parametrisation

The CKM parametrisation put forward by Chau and Keung [24]

$$V_{CKM} = \begin{pmatrix} c_{12}c_{13} & s_{12}c_{13} & s_{13}e^{-i\delta_{13}} \\ -s_{12}c_{23} - c_{12}s_{23}s_{13}e^{i\delta_{13}} & c_{12}c_{23} - s_{12}s_{23}s_{13}e^{i\delta_{13}} & s_{23}c_{13} \\ s_{12}s_{23} - c_{12}c_{23}s_{13}e^{i\delta_{13}} & -c_{12}s_{23} - s_{12}c_{23}s_{13}e^{i\delta_{13}} & c_{23}c_{13} \end{pmatrix} \tag{2.9}$$

is used as standard. The parameters, $s_{ij} \equiv sin(\theta_{ij})$, $c_{ij} \equiv cos(\theta_{ij})$ are the sine and cosine of the quark mixing angles and θ_{12} is the Cabibbo angle [4]. The CP violating phase is denoted δ_{13}.

The magnitude of the CKM matrix elements have been determined resulting in the PDG average values [25] of

$$|V_{CKM}| = \begin{pmatrix} 0.97373 \pm 0.00031 & 0.2243 \pm 0.0008 & 0.00382 \pm 0.0002 \\ 0.221 \pm 0.004 & 0.975 \pm 0.006 & 0.0408 \pm 0.0014 \\ 0.0086 \pm 0.0002 & 0.0415 \pm 0.0009 & 1.014 \pm 0.029 \end{pmatrix}. \tag{2.10}$$

A further parametrisation known as the Wolfenstein parametrisation [26] can be motivated by the hierarchy evident in the off-diagonal terms compared with the diagonal terms of magnitude of approximately 1 within Equation 2.10 in terms of Equation 2.9 which leads to $s_{13} \ll s_{23} \ll s_{12}$. Consequently, the matrix elements can be parametrised in terms of a power series in real parameter $\lambda \equiv s_{12} \simeq 0.23$ embodying the hierarchy. Therefore s_{12}, s_{23} and $s_{13}e^{-i\delta_{13}}$ are written as

$$\begin{aligned} s_{12} &= \lambda \\ s_{23} &= A\lambda^2 \\ s_{13}e^{-i\delta_{13}} &= A\lambda^3(\rho - i\eta) \end{aligned} \tag{2.11}$$

where A, ρ, η are real parameters. The other matrix elements follow from the parameters in Equation 2.11, unitary requirements and Equation 2.9. Thus, the Wolfenstein parametrisation of the CKM matrix up up to $\mathcal{O}(\lambda^3)$ is

$$V_{CKM} = \begin{pmatrix} 1-\frac{\lambda^2}{2} & \lambda & A\lambda^3(\rho - i\eta) \\ -\lambda & 1-\frac{\lambda^2}{2} & A\lambda^2 \\ A\lambda^3(1-\rho-i\eta) & -A\lambda^2 & 1 \end{pmatrix} + \mathcal{O}(\lambda^4). \tag{2.12}$$

This indicates that the CKM matrix elements V_{ub} and V_{td} have the largest CP violation because they are the only matrix elements which have imaginary components up to order $\mathcal{O}(\lambda^3)$. Furthermore, the Wolfenstein parametrisation of the CKM matrix as well as the magnitudes of the CKM matrix demonstrate that quark transitions within each of the three quark generations are favoured compared to the transitions between each of the generations [11]

2.3.2 The Unitary Triangle

The CKM matrix [9] is unitary such that $V^\dagger_{CKM}V_{CKM} = V_{CKM}V^\dagger_{CKM} = \mathbb{1}$, therefore the rows and columns of the CKM matrix can be related using orthogonality conditions

$$\sum_{i\in\{u,c,t\}} V_{ij}V^*_{ik} = \delta_{jk}\ ,\ j,k \in \{d,s,b\}, \tag{2.13}$$

$$\sum_{j\in\{d,s,b\}} V_{ij}V^*_{kj} = \delta_{ik}\ ,\ i,k \in \{u,c,t\}. \tag{2.14}$$

These relations lead to nine equations. Of the 6 equations which sum to zero the equation of interest in this analysis is

$$V_{ud}V^*_{ub} + V_{cd}V^*_{cb} + V_{td}V^*_{tb} = 0. \tag{2.15}$$

Equation 2.15 can be divided by $V_{cd}^{*}V_{cb}$ to give

$$\frac{V_{ud}V_{ub}^{*}}{V_{cd}V_{cb}^{*}} + 1 + \frac{V_{td}V_{tb}^{*}}{V_{cd}V_{cb}^{*}} = 0, \tag{2.16}$$

which is represented as the Unitary Triangle in the complex plane as shown in Figure 2.1. Thus, the three angles of the Unitary Triangle must be constrained by $\alpha + \beta + \gamma = 180°$. Consequently, a deviation from the Standard Model would be exposed if the measured angles within the Unitary Triangle do not sum to 180°. Therefore, over-constraining the parameters associated with the Unitary Triangle is a vital test of the Standard Model.

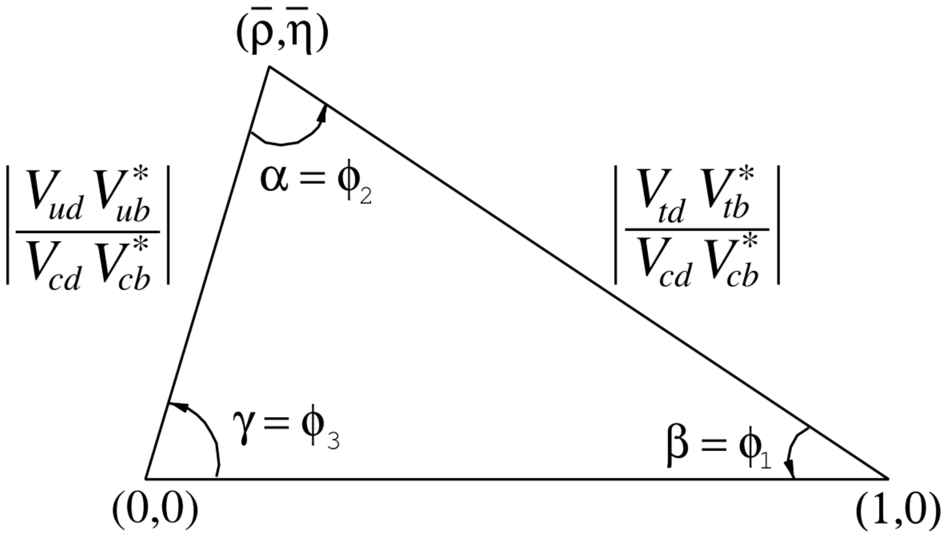

Figure 2.1: Representation of the Unitary Triangle in the complex plane, where $\bar{\rho} + i\bar{\eta} \equiv \rho(1-\lambda^2/2) + i\eta(1-\lambda^2/2)$. The angle γ corresponds to the complex phase within the CKM matrix in Equation 2.9. Figure from [25].

In this analysis the CKM angle γ is measured where

$$\gamma \equiv \arg\left(-\frac{V_{ud}V_{ub}^{*}}{V_{cd}V_{cb}^{*}}\right) = \arg\left(-\frac{V_{cb}V_{cd}^{*}}{V_{ub}V_{ud}^{*}}\right). \tag{2.17}$$

Therefore, by comparing Equation 2.17 with Equations 2.9 and 2.12, it can be seen that up to order $\mathcal{O}(\lambda^3)$ the CKM matrix element with the complex phase γ is the matrix element V_{ub}.

2.3.3 Current State of the Measurement of CKM Angle γ at LHCb

The LHCb experiment has a successful history of aiding the progress of sensitivity to γ, most recently producing the most precise combination of direct measurements of the CKM angle

γ from a single experiment $\gamma = (65.4^{+3.8}_{-4.2})^\circ$ [27]. This was the result of a combination of 15 independent LHCb analyses, and is within 1σ of the worldwide combination of indirect measurements by the CKM fitter group of $\gamma = (65.5^{+1.1}_{-2.7})^\circ$ [28]. Furthermore, the measurement from a single decay channel with the highest sensitivity to γ is also a LHCb analysis utilising the BPGGSZ approach (explained in Section 2.4.3), determining $\gamma = (68.7^{+5.2}_{-5.1})^\circ$ [29]. The contrast between the uncertainty associated with the best LHCb measurement from a signal decay channel, and that of the measurement from a combination of the channels across the LHCb experiment, demonstrate that gaining higher sensitivity to γ depends upon the combination of multiple different decay channels. Thus, further measurements are needed as inputs for direct measurement combinations to increase the sensitivity to the CKM angle γ.

The high sensitivity in previous combination measurements is largely a consequence of time independent measurements of direct CP violation in $B \to DK$ decays. This analysis utilises $B \to DK$ decays to measure γ and is discussed further is Section 2.4.

2.4 Model independent measurement of CKM Angle γ with $B \to DK$ and $B \to D\pi$ decays

$B^\pm \to DK^\pm$ decays are dominated by tree-level diagrams in Figures 2.3 and 2.4. Thus, $B^\pm \to DK^\pm$ decays can be very cleanly related to the underlying Standard Model parameter γ with a negligible theoretical irreducible error ($\lesssim \times 10^{-7}$) [6]. Consequently, measurements of the CKM angle γ using $B^\pm \to DK^\pm$ decays are pivotal to over-constraining the Unitary Triangle which is a key test of the consistency of the Standard Model. Moreover, it is a widely held view that tree diagrams are unlikely to be affected by New Physics whilst the contrary is expected in loop diagrams, however it has been indicated that sizeable New Physics at tree level is also possible [7] [8]. Beyond Standard Model effects are likely to manifest differently in tree and loop diagrams, therefore comparing the differences in the results of the CKM angle γ between these methods could provide interesting insights.

This section introduces the principle of measuring the CKM angle γ using $B^\pm \to DK^\pm$decays, details the model-independent BPGGSZ [30] [31] [32] [33] measurement approach and explains the inclusion of $B^\pm \to D\pi^\pm$as a additional signal channel.

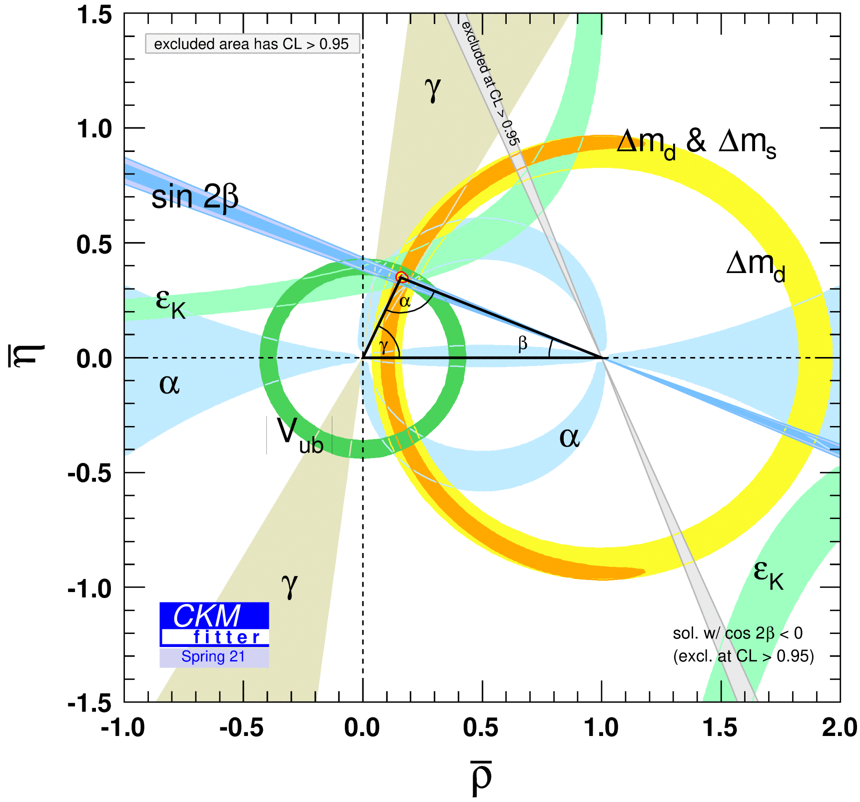

Figure 2.2: Current constraints on the Unitary Triangle parameters as determined by the CKM Fitter group using a combination of different sources. The shadeds areas are constraints on the different parameters. Figure from [28].

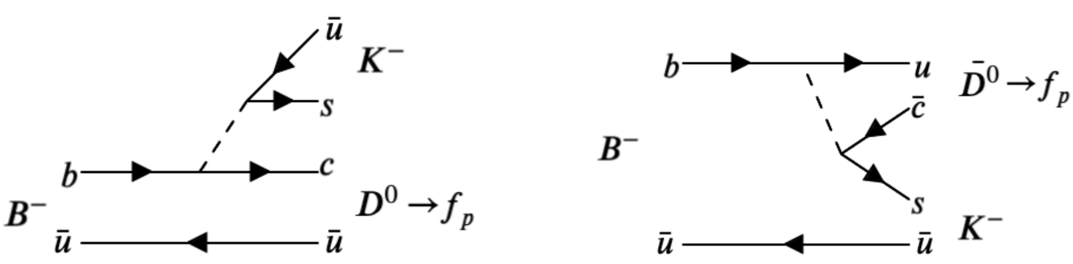

Figure 2.3: The $B^- \to D^0 K^-$ decay (left) and $B \to \bar{D}^0 K^-$ decay (right) dominant Feynman diagrams. The $B^- \to \bar{D}^0 K^-$ decay amplitude incorporates the $V_{ub} = |V_{ub}|e^{-i\gamma}$ matrix elements. The $B^- \to D^0 K^-$ decay also has a contribution from an internal diagram which is suppressed.

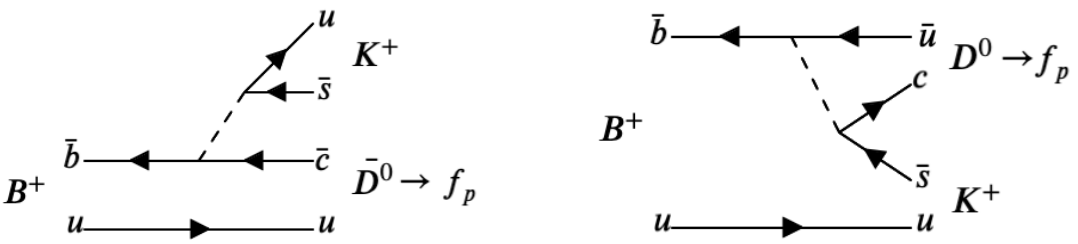

Figure 2.4: The $B^+ \to D^0K^+$ decay (left) and $B^+ \to \bar{D}^0K^+$ decay (right) dominant Feynman diagrams. The $B^+ \to D^0K^\pm$ decay amplitude incorporates the $V_{ub}^* = |V_{ub}|e^{+i\gamma}$ matrix element. The $B^+ \to D^0K^+$ decay also has a contribution from an internal diagram which is suppressed.

2.4.1 Principle of Measurement

The following section describes the principles behind measuring the CKM angle γ using $B^\pm \to DK^\pm$ decays.

Within the CKM matrix in Equation 2.9 the complex phase δ_{13} corresponds to the CKM angle γ up to order $\mathcal{O}(\lambda^3)$. Amplitudes defined in the form $\mathscr{A} = Ae^{i\phi}$, where A is real and ϕ is the complex phase, have observables proportional to $\mathscr{A}\mathscr{A}^* = AA$, for example the decay width observable Γ. Interference between two amplitudes from the same decay is required to gain sensitivity to the complex phase and hence the CKM angle γ. When this occurs for amplitudes $\mathscr{A}_1 = A_1e^{i\phi_1}$ and $\mathscr{A}_2 = A_2e^{i\phi_2}$, the decay width Γ can be written as

$$\Gamma \propto (\mathscr{A}_1 + \mathscr{A}_2)(\mathscr{A}_1 + \mathscr{A}_2)^* = A_1^2 + A_2^2 + 2A_1A_2\cos(\phi_1 - \phi_2) \quad (2.18)$$

where the third term is the interference term and the ϕ_1 and ϕ_2 complex phases can be measured.

In $B^\pm \to DK^\pm$ decays it is possible for $B^\pm$ meson to decay by $B^\pm \to D^0K^\pm$ and $B^\pm \to \bar{D}^0K^\pm$ decays as shown in Figures 2.3 and 2.4. Therefore, it is possible for interference to occur between the two decay amplitudes $B^\pm \to D^0K^\pm$ and $B^\pm \to \bar{D}^0K^\pm$ providing the D^0 and $\bar{D}^0$ mesons both decay to the same final state as demonstrated in Figure 2.5. Consequently, the complex phase difference between the 2 decay amplitudes in each of the B^+ and B^- decays can be obtained.

In this analysis, both the D^0 and $\bar{D}^0$ mesons are reconstructed in the self-conjugate multi-body final state $2\pi^+2\pi^-$. A four-body multi-body final state with zero spin corresponds to a five-dimensional phase space. The D^0 meson decay's strong phase and magnitude change

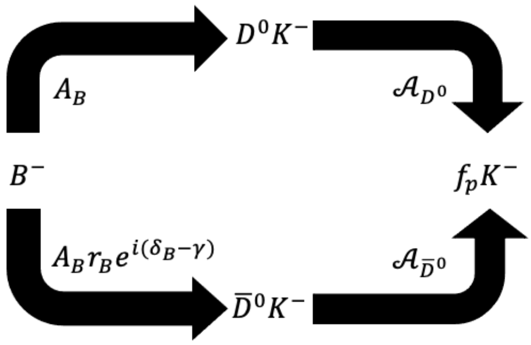

Figure 2.5: The interference between $B^+ \to D^0K^+$ and $B^+ \to \bar{D}^0K^+$ decays (left) as well as between $B^- \to D^0K^-$ and $B^- \to \bar{D}^0K^-$ decays (right), which occurs providing the D meson is reconstructed in a final state which is accessible to the D^0 and the $\bar{D}^0$.

over the five-dimensional phase space. Thus, the $B^\pm \to DK^\pm$ decay and $B^\pm \to \bar{D}K^\pm$ decay amplitudes' interference can be established over the D meson decay phase space. Consequently, γ can be determined at every point of the D decay phase space, and increased sensitivity to γ attained compared to measurements of γ integrated over the whole phase space.

In this analysis the model independent BPGGSZ approach is implemented. In this model-independent method the measurement of γ is determined at different points over the 5-dimensional phase space of the D meson decay, increasing the sensitivity to γ. The significant systematic uncertainty associated with modelling the complex strong phase of the D decay amplitude across the five-dimensional phase space of the four-body decay is avoided by undertaking a model independent approach. This is achieved by separating the D decay phase space into bins and integrating the decay rate over each bin. The resulting D decay quantities are called hadronic parameters some of which can been measured model independently. The BPGGSZ method is discussed further in Section 2.4.3.

2.4.2 The CKM Angle γ as an observable in $B \to DK$ tree level decays

The leading contribution of the B amplitudes can be derived from Feymann diagrams such as in Figure 2.3 for the B^- decay. Thus, as shown in Figure 2.5 the B^- decay amplitudes can be established using

$$\mathscr{A}(B^- \to D^0K^-) = A_B \tag{2.19}$$

$$\mathscr{A}(B^- \to \bar{D}^0K^-) = A_Br_Be^{i(\delta_B-\gamma)} \tag{2.20}$$

where r_B is the ratio of the magnitudes of the amplitudes and δ_B is the strong phase difference between the amplitudes. CP conjugation of the decay amplitudes will lead to a sign change of the CP violating weak phase difference γ between the amplitudes. Thus, as shown in Figure 2.5 the B^+ decay amplitudes are

$$\mathscr{A}(B^+ \to \bar{D}^0 K^+) = A_B \tag{2.21}$$

$$\mathscr{A}(B^+ \to D^0 K^+) = A_B r_B e^{i(\delta_B+\gamma)}. \tag{2.22}$$

The D^0 and $\bar{D}^0$ meson decays are reconstructed in a final state $f(\hat{p})$, thus the decay amplitudes can be defined as

$$\mathscr{A}(D^0 \to f(\hat{p})) = A^f_{\hat{p}} e^{i\delta^f_{\hat{p}}} \tag{2.23}$$

$$\mathscr{A}(\bar{D}^0 \to f(\hat{p})) = \bar{A}^f_{\hat{p}} e^{i\bar{\delta}^f_{\hat{p}}} \tag{2.24}$$

where $A^f_{\hat{p}}$ and $\bar{A}^f_{\hat{p}}$ are real and $\delta^f_{\hat{p}}$ and $\bar{\delta}^f_{\hat{p}}$ are the strong phases of the D^0 and $\bar{D}^0$ decays. The parameter $\hat{p}$ is defined as a point in the phase space of the $D \to f$ decay. When the assumption that CP violation is negligible in $D \to f$ decays is applied, the two D meson decay amplitudes can be related to each other

$$\mathscr{A}(\bar{D}^0 \to f(\hat{p})) = \mathscr{A}(D^0 \to f(\bar{\hat{p}})) \tag{2.25}$$

where the CP conjugate of point $\hat{p}$ is $\bar{\hat{p}}$, in this case the charges and the three momenta are the opposite for all the particles in the final state.

The respective total amplitudes of the B^- and B^+ decays can be written as a coherent superposition of the two decay paths in each decay

$$\mathscr{A}(B^- \to D(\to f(\hat{p}))K^-) = \mathscr{A}(B^- \to D^0 K^-)\mathscr{A}(D^0 \to f(\hat{p})) + \mathscr{A}(B^- \to \bar{D}^0 K^-)\mathscr{A}(\bar{D}^0 \to f(\hat{p})) \tag{2.26}$$

$$\mathscr{A}(B^+ \to D(\to f(\hat{p}))K^+) = \mathscr{A}(B^+ \to D^0 K^+)\mathscr{A}(D^0 \to f(\hat{p})) + \mathscr{A}(B^+ \to \bar{D}^0 K^+)\mathscr{A}(\bar{D}^0 \to f(\hat{p})). \tag{2.27}$$

The decay rate Γ of each of the B^- and B^+ decays can be established by squaring Equations 2.26 and 2.27 respectively

$$\Gamma(B^- \to D(\to f(\hat{p}))K^-) \propto |\mathscr{A}(B^- \to D^0K^-)\mathscr{A}(D^0 \to f(\hat{p})) + \mathscr{A}(B^- \to \bar{D}^0K^-)\mathscr{A}(\bar{D}^0 \to f(\hat{p}))|^2 \tag{2.28}$$

$$\Gamma(B^+ \to D(\to f(\hat{p}))K^+) \propto |\mathscr{A}(B^+ \to D^0K^+)\mathscr{A}(D^0 \to f(\hat{p})) + \mathscr{A}(B^+ \to \bar{D}^0K^+)\mathscr{A}(\bar{D}^0 \to f(\hat{p}))|^2. \tag{2.29}$$

It is possible to write these decay rates in terms of the amplitudes defined in Equations 2.19 to 2.24

$$\begin{aligned}\Gamma(B^- \to D(\to f(\hat{p}))K^-) &\propto |A^f_{\hat{p}} e^{i\delta^f_{\hat{p}}} + r_B e^{i(\delta_B-\gamma)}\bar{A}^f_{\hat{p}} e^{i\bar{\delta}^f_{\hat{p}}}|^2 \\ &\propto A^{f\,2}_{\hat{p}} + r_B^2\bar{A}^{f\,2}_{\hat{p}} + 2A^f_{\hat{p}}\bar{A}^f_{\hat{p}}(x_-\cos(\Delta\delta^f_{\hat{p}}) + y_-\sin(\Delta\delta^f_{\hat{p}}))\end{aligned} \tag{2.30}$$

$$\begin{aligned}\Gamma(B^+ \to D(\to f(\hat{p}))K^+) &\propto |r_B e^{i(\delta_B+\gamma)}A^f_{\hat{p}} e^{i\delta^f_{\hat{p}}} + \bar{A}^f_{\hat{p}} e^{i\bar{\delta}^f_{\hat{p}}}|^2 \\ &\propto r_B^2 A^{f\,2}_{\hat{p}} + \bar{A}^{f\,2}_{\hat{p}} + 2A^f_{\hat{p}}\bar{A}^f_{\hat{p}}(x_+\cos(\Delta\delta^f_{\hat{p}}) - y_+\sin(\Delta\delta^f_{\hat{p}}))\end{aligned} \tag{2.31}$$

where $\Delta\delta^f_{\hat{p}} = \delta^f_{\hat{p}} - \bar{\delta}^f_{\hat{p}}$ is the strong phase difference between the D decays and the CKM angle γ is included within the CP observables $x_\pm = r_B\cos(\delta_B \pm \gamma)$ and $y_\pm = r_B\sin(\delta_B \pm \gamma)$. Therefore, providing the strong phase difference is not equal to zero and the D^0 and $\bar{D}^0$ mesons decay to the same final state, the CKM angle γ is observable in the difference of the B^+ and B^- decay rates.

The CP observables $x_\pm$ and $y_\pm$ are ordinarily established simultaneously, which then allows γ, δ_B and r_B to be extracted. This process is industry standard due to the CP observables being statistically better behaved. Whereas, $\Delta\delta^f_{\hat{p}}$, $\bar{A}^f_{\hat{p}}$ $A^f_{\hat{p}}$ of the D meson decays at point $\hat{p}$ in the four pion phase space need to be measured separately. This can be achieved using a model-dependent or model-independent method. The model-dependent method determines the D decay related quantities by using a D meson decay amplitude-model, which describes every infinitesimal point in D meson phase space. However, this approach leads to a significant systematic uncertainty associated with modelling the complex strong phase of the D decay amplitude across the five-dimensional phase space of the four-body decay. The model-independent BPGGSZ approach circumvents the significant systematic uncertainty by separating the D decay phase space into bins, and integrating the decay rate over each bin. The resulting D decay related quantities are called hadronic parameters which can be measured model independently. Thus, Equations 2.30 and 2.31 can be rewritten in terms of the hadronic parameters as detailed in the next section.

2.4.3 BPGGSZ Method of $D \to 2\pi^+2\pi^-$

There are a number of different final states the D meson can be reconstructed in which are dependent on the method used for the measurement and are described below.

- The ADS method [34]: The method reconstructs the D^0 meson in a Cabbibo favoured final state and the $\bar{D}^0$ is reconstructed in a Cabibbo suppressed or visa versa.
- The GLW method [35]: The D meson is reconstructed in a CP eigenstate.
- The BPGGSZ method [30] [31] [32] [33]: The method reconstructs the D meson in a self-conjugate multi-body final state.

The BPGGSZ method was proposed by Bondar, Poluektov, Giri, Grossman, Soffee, Zupan [30] [31] [32] [33], and at the time of writing has produced the highest sensitivity to γ by any single measurement [29]. As previously explained in Sections 2.4.1 and 2.4.2 the model independent BPGGSZ method for $\mathrm{D} \to 2\pi^+2\pi^-$ is being used in this analysis to measure the CKM angles γ. The approach measures γ within different bins across the four pion phase space to increase the sensitivity to γ. Since the BPGGSZ approach is a model independent method the D meson decay amplitude related quantities, $\Delta\delta^f_{\hat{p}}$, $\bar{A}^f_{\hat{p}}$ $A^f_{\hat{p}}$, are replaced by model independent hadronic parameters which are measured independently, as previously mentioned in Section 2.4.2. The hadronic parameters are defined below.

The yields in bin i for the $D^0 \to f$ and $\bar{D}^0 \to f$ decays are denoted K^f_i and $\bar{K}^f_i$ respectively and are known as the flavour tagged yields. They are expressed as

$$K^f_i = \int_i |A^f_{\hat{p}}|^2 \phi(\hat{p}) d\hat{p} \tag{2.32}$$

$$\bar{K}^f_i = \int_i |\bar{A}^f_{\hat{p}}|^2 \phi(\hat{p}) d\hat{p} \tag{2.33}$$

where the density of states at the point in phase space $\hat{p}$ is $\phi(\hat{p})$. Once normalised the flavour-tagged yields provide the flavour-tagged fraction of the yields in bin i

$$T^f_i = \frac{K^f_i}{\sum_i K^f_i} \tag{2.34}$$

$$\bar{T}^f_i = \frac{\bar{K}^f_i}{\sum_i \bar{K}^f_i} \tag{2.35}$$

where $\sum_i T_i^f = 1$ and $\sum_i \bar{T}_i^f = 1$.

The average amplitude-weighted cosine, c_i^f, and average amplitude-weighted sine, s_i^f, of the strong phase in bin i are defined as

$$c_i^f = \frac{1}{\sqrt{K_i^f \bar{K}_i^f}} \int_i |A_{\hat{p}}^f||\bar{A}_{\hat{p}}^f| \cos(\Delta\delta_{\hat{p}}^f)\phi(\hat{p})d\hat{p} \tag{2.36}$$

$$s_i^f = \frac{1}{\sqrt{K_i^f \bar{K}_i^f}} \int_i |A_{\hat{p}}^f||\bar{A}_{\hat{p}}^f| \sin(\Delta\delta_{\hat{p}}^f)\phi(\hat{p})d\hat{p} \tag{2.37}$$

Consequently, integrating the decay rates over the phase space of bin i means Equations 2.30 and 2.31 can be expressed as

$$\Gamma(B^- \to D(\to f(\hat{p}))K^-) \propto T_i^f + r_B^2 \bar{T}_i^f + 2\sqrt{T_i^f \bar{T}_i^f}(c_i^f x_- + s_i^f y_-) \tag{2.38}$$

$$\Gamma(B^+ \to D(\to f(\hat{p}))K^+) \propto \bar{T}_i^f + r_B^2 T_i^f + 2\sqrt{T_i^f \bar{T}_i^f}(c_i^f x_+ - s_i^f y_+). \tag{2.39}$$

In reality the experimental phase space acceptance $\eta(\hat{p})$ will not be identical to the LHCb acceptance if the hadronic parameters are measured using data from a different experiment, and will vary over the phase space so should be taken into account. Thus, Equations 2.34 and 2.35 can instead be expressed as

$$F_i^f = \frac{\int_i |A_{\hat{p}}^f|^2 \phi(\hat{p})\eta(\hat{p})d\hat{p}}{\sum_i \int_i |A_{\hat{p}}^f|^2 \phi(\hat{p})\eta(\hat{p})d\hat{p}} \tag{2.40}$$

$$\bar{F}_i^f = \frac{\int_i |\bar{A}_{\hat{p}}^f|^2 \phi(\hat{p})\eta(\hat{p})d\hat{p}}{\sum_i \int_i |\bar{A}_{\hat{p}}^f|^2 \phi(\hat{p})\eta(\hat{p})d\hat{p}} \tag{2.41}$$

where F_i^f and $\bar{F}_i^f$ are the flavour-tagged fractions of the D^0 and $\bar{D}^0$ decays in bin i where $\eta(\hat{p})$ accounts for any phase space acceptance effects. It has been shown previously that the hadronic parameter inputs c_i and s_i measured using CLEO-c data can be treated as if they are the equivalent c_i and s_i which would be correct for the LHCb phase space acceptance [29]. As a result, Equations 2.38 and 2.39 can be modified to be

$$\Gamma(B^- \to D(\to f(\hat{p}))K^-) \propto F_i^f + r_B^2 \bar{F}_i^f + 2\sqrt{F_i^f \bar{F}_i^f}(c_i^f x_- + s_i^f y_-) \tag{2.42}$$

$$\Gamma(B^+ \to D(\to f(\hat{p}))K^+) \propto \bar{F}_i^f + r_B^2 F_i^f + 2\sqrt{F_i^f \bar{F}_i^f}(c_i^f x_+ - s_i^f y_+) \tag{2.43}$$

where the CKM angle γ is included within the CP observables $x_\pm = r_B \cos(\delta_B \pm \gamma)$ and $y_\pm = r_B \sin(\delta_B \pm \gamma)$.

It is beneficial to utilise the self-conjugate $2\pi^+2\pi^-$ final state of the D meson to define pairs of bins such that bin $+i$ and bin $-i$ map onto one another under a CP transformation. Thus, a point $\hat{p}$ in bin $+i$ has a corresponding CP conjugate point $\bar{\hat{p}}$ in bin $-i$. Therefore, the definition of CP conjugate bin pairs alongside Equation 2.25 and $\Delta\delta^f_{\hat{p}} = -\Delta\delta^f_{\bar{\hat{p}}}$ means the hadronic parameters relations between bin $+i$ and $-i$ are

$$\begin{aligned} K^f_{-i} &= \bar{K}^f_i, & \bar{K}^f_{-i} &= K^f_i \\ T^f_{-i} &= \bar{T}^f_i, & \bar{T}^f_{-i} &= T^f_i \\ F^f_{-i} &= \bar{F}^f_i, & \bar{F}^f_{-i} &= F^f_i \\ c^f_{-i} &= c^f_i, & s^f_{-i} &= -s^f_i. \end{aligned} \tag{2.44}$$

Additionally, the third relation above relies on the assumption that there are no charge asymmetries within the detector so $\eta(\hat{p}) = \eta(\bar{\hat{p}})$ can be applied.

The hadronic parameter relations and proportionality constants h_{B^-} and h_{B^+} can be inserted into the Equations 2.42 and 2.43 to express the number of B^+ and B^- events in bin i as

$$N_i^{B^- \to DK^-} = h_{B^-}(F_i + r_B^2 F_{-i} + 2\sqrt{F_i F_{-i}}(c_i x_- + s_i y_-)), \tag{2.45}$$

$$N_i^{B^+ \to DK^+} = h_{B^+}(F_{-i} + r_B^2 F_i + 2\sqrt{F_i F_{-i}}(c_i x_+ - s_i y_+)), \tag{2.46}$$

and when substituted for bin $-i$

$$N_{-i}^{B^- \to DK^-} = h_{B^-}(F_{-i} + r_B^2 F_i + 2\sqrt{F_{-i} F_i}(c_i x_- - s_i y_-)), \tag{2.47}$$

$$N_{-i}^{B^+ \to DK^+} = h_{B^+}(F_i + r_B^2 F_{-i} + 2\sqrt{F_{-i} F_i}(c_i x_+ + s_i y_+)). \tag{2.48}$$

Since the final state, $D \to 2\pi^+2\pi^-$ is the same throughout the analysis the f superscript notation has been dropped and will continue to not be written explicitly.

Therefore, $B^\pm \to DK^\pm$ can be used to measure the CKM angle γ without any dependency on a D meson amplitude decay model. The model independent hadronic parameters c_i, s_i, T_i and $\bar{T}_i$ were previously measured with CELO-c data for multiple binning schemes in Reference [36] using quantum correlated $D\bar{D}$ decays. The binning scheme which provided the highest sensitivity to γ following a sensitivity study, discussed in Chapter 4, was chosen for the measurement in this analysis.

2.4.4 Inclusion of $B \to D\pi$ as a Signal Channel

The $B^\pm \to D\pi^\pm$ decay is similar kinematically to the $B^\pm \to DK^\pm$ decay. Therefore, it is possible to measure γ using $B^\pm \to D\pi^\pm$ decays, analogously to the theory and method discussed for $B^\pm \to DK^\pm$ decays previously with the same multi-body final state. Consequently, Equations 2.45 and 2.46 can also be written in terms of the $B \to D\pi$ channel such that

$$N_i^{B^- \to D\pi^-} = h_{B^-}^{D\pi}(F_i + r_B^2 F_{-i} + 2\sqrt{F_i F_{-i}}(c_i x_-^{D\pi} + s_i y_-^{D\pi})) \tag{2.49}$$

$$N_i^{B^+ \to D\pi^+} = h_{B^+}^{D\pi}(F_{-i} + r_B^2 F_i + 2\sqrt{F_i F_{-i}}(c_i x_+^{D\pi} - s_i y_+^{D\pi})) \tag{2.50}$$

where the F_i, c_i and s_i are identical to those of the $B \to DK$ decay because the D meson decays to the same $2\pi^+2\pi^-$ final state . However, the $x_\pm$ and $y\pm$ parameters will be different as r_B and δ_B will not be the same for the two decay channels. For clarity, they will be denoted as r_B^{DK} and δ_B^{DK} in the $B^\pm \to DK^\pm$ decay channel and $r_B^{D\pi}$ and $\delta_B^{D\pi}$ in the $B^\pm \to D\pi^\pm$ channel. Thus, the CP observables will also be denoted as $x_\pm^{DK}$, $y_\pm^{DK}$ and $x_\pm^{D\pi}$, $y_\pm^{D\pi}$ for the two decay channels respectively. Inclusion of the $B^\pm \to D\pi^\pm$ channel results in eight CP observables across the two decay channels which contain five physics parameters. The parameter $\xi^{D\pi}$ is introduced in order to reduce the numbers of degrees of freedom

$$\xi^{D\pi} = \frac{r_B^{D\pi}}{r_B^{DK}} e^{(i(\delta_B^{D\pi} - \delta_B^{DK}))}. \tag{2.51}$$

Therefore $x_\pm^{D\pi}$ and $y_\pm^{D\pi}$ can be reparameterised in terms of nuisance parameters

$$x_\xi^{D\pi} = \mathscr{R}(\xi^{D\pi}) \tag{2.52}$$

$$y_{\xi}^{D\pi} = \mathscr{I}(\xi^{D\pi}) \tag{2.53}$$

such that

$$x_{\pm}^{D\pi} = x_{\xi}^{D\pi} x_{\pm}^{DK} - y_{\xi}^{D\pi} y_{\pm}^{DK} \tag{2.54}$$

$$y_{\pm}^{D\pi} = x_{\xi}^{D\pi} y_{\pm}^{DK} + y_{\xi}^{D\pi} x_{\pm}^{DK}. \tag{2.55}$$

As ξ is independent of γ all the CP violation information is included in the $x_{\pm}^{DK}$ and $y_{\pm}^{DK}$ CP observables for both the $B \to DK$ and $B \to D\pi$ channels.

The ratio of the B decay amplitudes $r_B^{D\pi}$ and r_B^{DK} are expected to be approximately 0.005 and 0.1 respectively [37] and the sensitivity to γ is proportional to the ratio of the B decay amplitudes. Therefore, the sensitivity to γ is far greater in the DK channel.

Although, there is not a large gain in the sensitivity to γ, the inclusion of $B \to D\pi$ channel is also useful for other purposes. The c_i and s_i inputs have already been measured model independently, hence it is feasible to fit for the F_i hadronic parameters, as well as the $x_{\pm}^{DK}$, $y_{\pm}^{DK}$, $x_{\xi}^{D\pi}$, $y_{\xi}^{D\pi}$ CP observables simultaneously to the LHCb DK and $D\pi$ data samples in Chapter 7 . Thus, changes in the phase space acceptance $\eta(\hat{p})$ will cancel and an independent measurement for F_i using a control channel is not required. This eliminates any demand for a simulation based efficiency correction which can lead to a large systematic uncertainty [29] . Moreover, since CP violation is included in the $D\pi$ yield parameterisation the F_i parameters determined in the fit to both channels will not have an systematic effect caused by CP violation in the $D\pi$ channel.

2.5 The Binning Schemes for the D Meson Decay Phase Space

The hadronic parameters (which are solely related to the D decays) were previously measured with CELO-c data for five different binning schemes in Reference [36] using quantum correlated $D\bar{D}$ decays. The D^0 and $\bar{D^0}$ decay amplitudes vary over the multi-body phase space, as a result the same occurs for the weighted cosine c_i and sine s_i of the strong phase difference in the interference term. Therefore, the bins should be defined to prevent dilution of the overall interference across each bin, so optimal sensitivity can be achieved [36]. Reference [36] measured the Equal $\Delta\delta_p^{4\pi}$, Variable $\Delta\delta_p^{4\pi}$, Optimal, Optimal-alternative, and Alternate binning schemes. The Equal and Variable $\Delta\delta_p^{4\pi}$ binning schemes are based on the strong phase difference. The alternate binning scheme uses the relative magnitudes of the two decay channel amplitudes as well as considering the division of the strong phase difference across the bin. The Optimal and Optimal-alternative binning schemes are defined to optimise the expected sensitivity to γ in $B^{\pm} \to DK^{\pm}$ decays [36]. Each binning scheme has a varying total number of bins n_{bins}, where n_{bins} = 4, 8, 12, 16 or 20. The total number of bins is derived from there being i positive bins (denoted i_{max}) and i negative bins for each B charge such that $n_{bins} = 4i_{max}$ (see Chapter 4). As an example the Optimal-alternative hadronic parameter binning scheme for n_{bins} = 20 determined in Reference [36] is laid out in Table 2.3.

Table 2.3: Hadronic parameters for the Optimal-alternative binning scheme with n_{bins}=20 [36].

Optimal-alternative binning

i	c_i	s_i	T_i	$\overline{T}_i$
1	0.279 ± 0.143 ± 0.101	-0.379 ± 0.291 ± 0.104	0.096 ± 0.005 ± 0.002	0.032 ± 0.004 ± 0.005
2	0.622 ± 0.095 ± 0.059	-0.486 ± 0.237 ± 0.072	0.123 ± 0.006 ± 0.004	0.055 ± 0.004 ± 0.003
3	0.969 ± 0.057 ± 0.038	-0.089 ± 0.162 ± 0.038	0.202 ± 0.007 ± 0.005	0.164 ± 0.007 ± 0.003
4	0.463 ± 0.099 ± 0.046	0.245 ± 0.215 ± 0.067	0.134 ± 0.006 ± 0.005	0.077 ± 0.005 ± 0.004
5	-0.332 ± 0.138 ± 0.041	0.484 ± 0.263 ± 0.132	0.074 ± 0.005 ± 0.002	0.043 ± 0.004 ± 0.003
$\tilde{F}_+^{4\pi}$	0.771 ± 0.021 ± 0.010			
Q	0.760 ± 0.057 ± 0.017			

Chapter 3

The LHCb Experiment

The Large Hadron Collider Beauty Experiment (LHCb) is one of the four large experiments at the Large Hadron Collider (LHC), within the Centre for European Nuclear Research (CERN). The aim of LHCb is to investigate heavy flavour physics and search for evidence of beyond Standard Model physics in CP violation, as well as rare decays of beauty and charm hadrons [38].

The LHC is the largest particle collider in the world. The approximately 27 km long circular accelerator collides 2 proton beams travelling in opposite directions to produce a maximum centre-of-mass energy $\sqrt{s}$ of 14 TeV. The locations where the proton beams are brought to collision (collision points) are those of the experiments, such as the LHCb detector, spread around the circumference of the LHC.

This chapter describes the LHCb detector in the Run 2 data taking period providing a general overview, before outlining the tracking systems subdetectors and particle identification system. Furthermore, the 3 level trigger system and trigger lines are introduced as well as the LHCb software.

3.1 The LHC

The LHC is located under the Swiss-French border and is the most powerful particle accelerator on Earth at this point in time. To maintain the circulation of protons in the LHC ring, super conducting dipole magnets are used, where liquid helium is used to keep the temperature of the magnets at the required level. Opposite magnetic fields are induced in the 2 beampipes and then the proton beams are collided. In Run 1 the collision centre of mass energies were

7 TeV in 2011 and 8 TeV in 2012. Subsequently, in Run 2 $\sqrt{s}$ was equal to 13 TeV for 2015 to 2018. To reach these collision energies a series of particle accelerators gradually increase the energy. To begin with protons derived from ionised hydrogen are accelerated by a linear accelerator called LINAC2 to 50MeV. Subsequently successive synchrotrons known as the Proton Synchrotron Boost (BOOSTER), the Proton Synchrotron (PS) and the Super Proton Synchrotron (SPS), accelerate the protons to 1.4 GeV, 25 GeV and then 450 Gev beam energies, respectively. After, the protons are passed to the LHC which accelerates them further up to their target energies, this corresponds to each beam reaching an energy 6.5 TeV in Run 2. Once the proton bunches reach the target energies superconducting magnets are used to collide the beams. Collisions can occur for a number of hours, once completed the beam dump facility is utilised. The major LHC experiments including LHCb are illustrated in Figure 3.1.

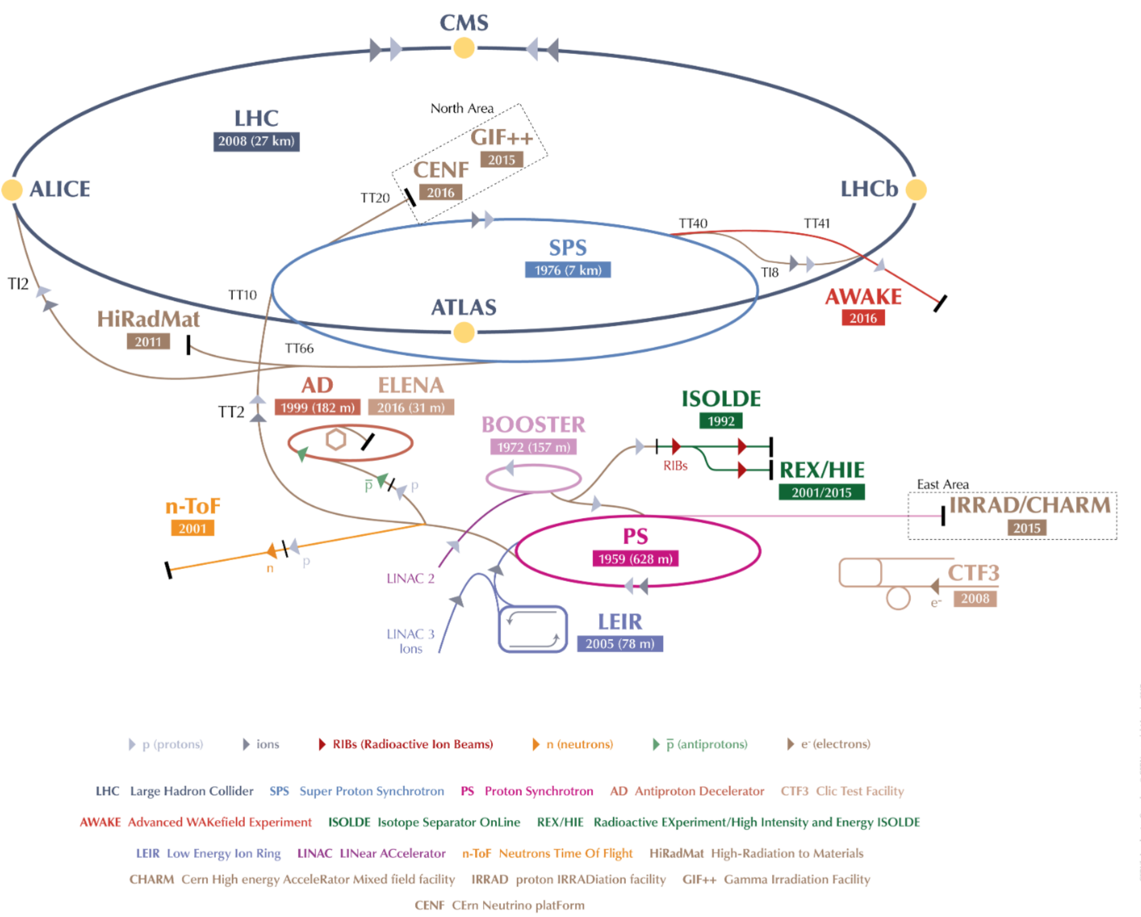

Figure 3.1: The LHC accelerator complex. The linear accelerators and synchrotrons accelerate the proton beams and pass them to the LHC ring (dark blue.) The major experiments are located at different collision points on the LHC ring. Other experiments have their beams provided by smaller machines. Figure from [39].

3.2 The LHCb Detector

The LHCb detector is a single arm forward spectrometer [40] designed to take advantage of the kinematics of the production of $b\bar{b}$ quark pairs, which leads to them being predominately forward or backward boosted as shown in Figure 3.2. Consequently, the LHCb detector acceptance is between 10 mrad and 300 mrad in the bending horizontal plane, and 10 mrad and 250 mrad in the non-bending vertical plane. Both planes' acceptance also correspond to pseudorapidity η between 1.8 and 5 or 2 and 5 respectively, where $\eta = -\ln(\tan(\frac{\theta}{2}))$.

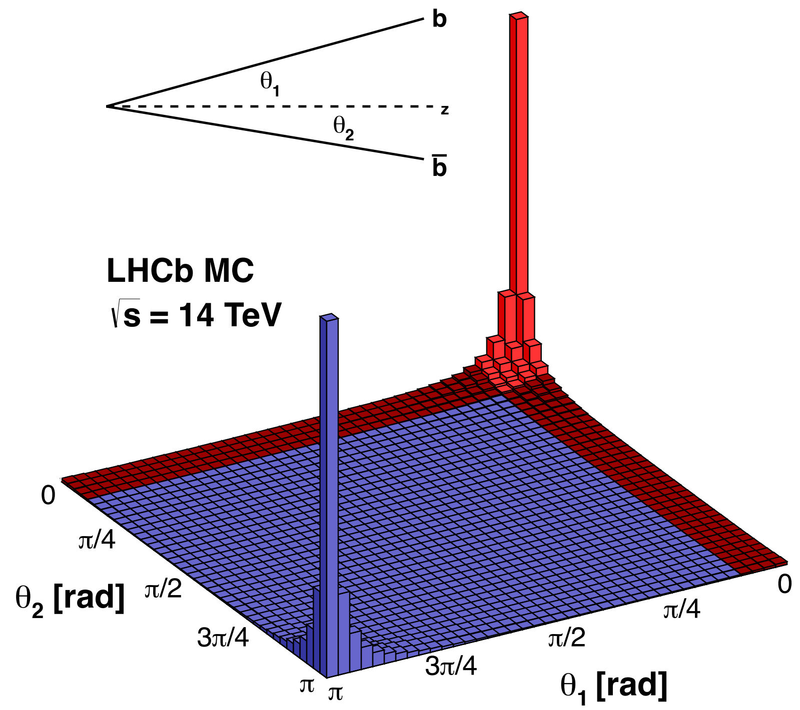

Figure 3.2: LHCb simulations of $b\bar{b}$ pair production as a function of opening angle (θ_1 is the b opening angle and θ_2 is the $\bar{b}$ opening angle) with a pp centre of mass energy of 14TeV. The acceptance of the LHCb detector is highlighted in red. Figure from [41].

Proton-beams are displaced with respect to one another at the collision point using corrector magnets, to alter the beam overlap when colliding. This provides LHCb with control of the number of pp interaction per bunch crossing, thus LHCb can tune the proton beans from the LHC in order to ensure uniform average luminosity.

Multiple subdetectors, providing effective triggering and particle identification as well as precision tracking and vertexing, are combined together to result in the overall LHCb detector as demonstrated in Figure 3.3. These are discussed in more detail within this chapter.

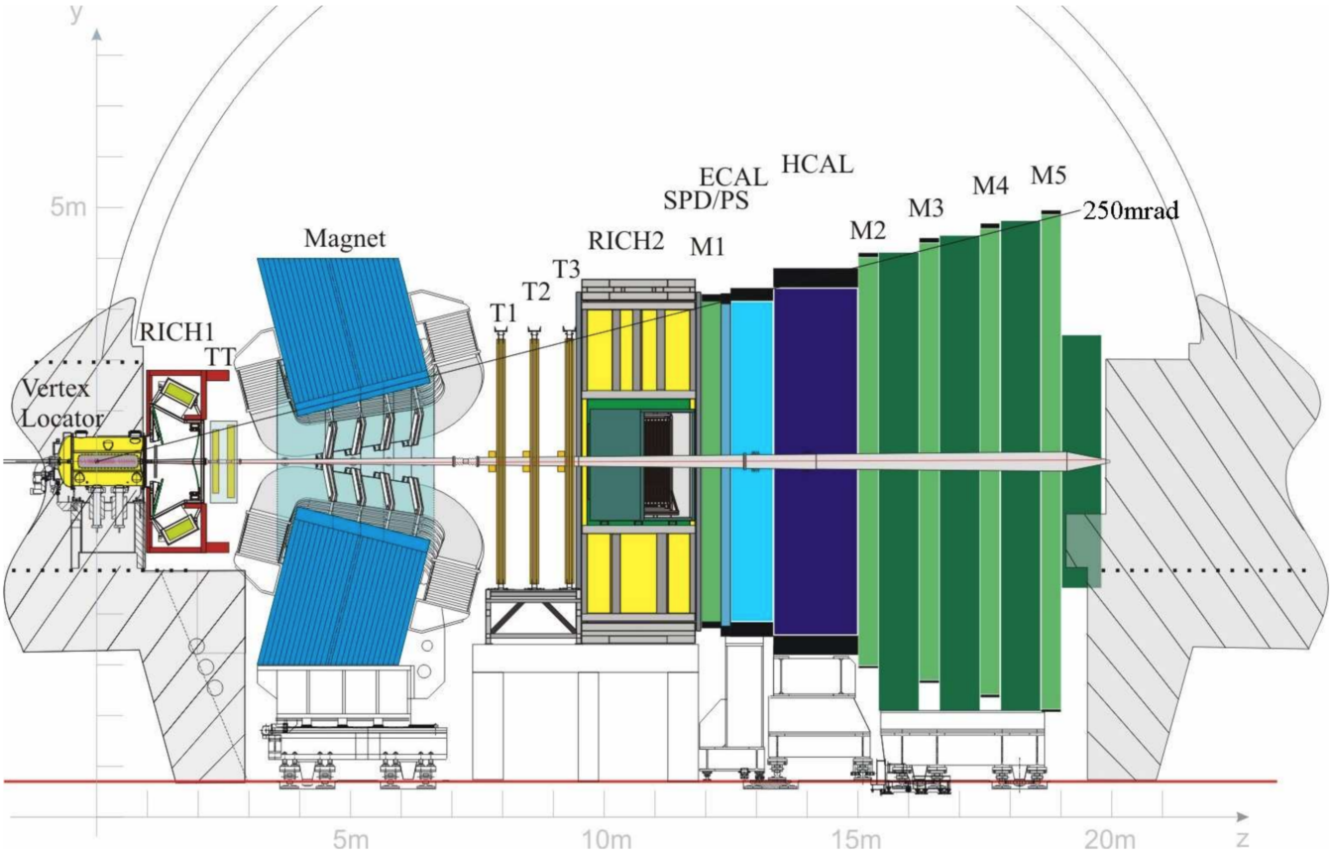

Figure 3.3: The cross-section of the LHCb detector. The pp collision point is at the origin and the z-axis is along the beam. Figure from [38].

3.2.1 The LHCb Tracking System

In order to perform high precision measurements of b and c decays LHCb requires a state of the art tracking system. The tracking system detects charged particle tracks and determines their momenta and reconstructs the production and decay vertices of the tracks.

The tracking system is composed of the Vertex Locator (VELO), the Magnet, the Silicon Tracker (ST) and the Outer Track (OT) [38]. The Tracker Turcenis (TT) and the Inner Tracker (IT) within the tracking stations (T1, T2 and T3) are the elements of the Silicon Tracker. The outer element of the tracking stations is the Outer tracker. The components of the tracking system can be observed in Figure 3.3

3.2.1.1 The Vertex Locator

The Vertex Locator (VELO) [42] contains successive two-sided, semi-circular silicon modules, laid out over approximately 1 metre under vacuum in the beam direction, to measure r and ϕ coordinates using R and Φ silicon strip sensors respectively as demonstrated in Figure 3.4. The silicon modules consist of retractable halves so they can be automatically opened during beam injection, then aligned and closed to within 7mm from the beam when the beam is stable for collisions. The VELO surrounds the pp interaction point and therefore provides the accurate location of the primary vertex (PV) and the impact parameters (IP) of the tracks.

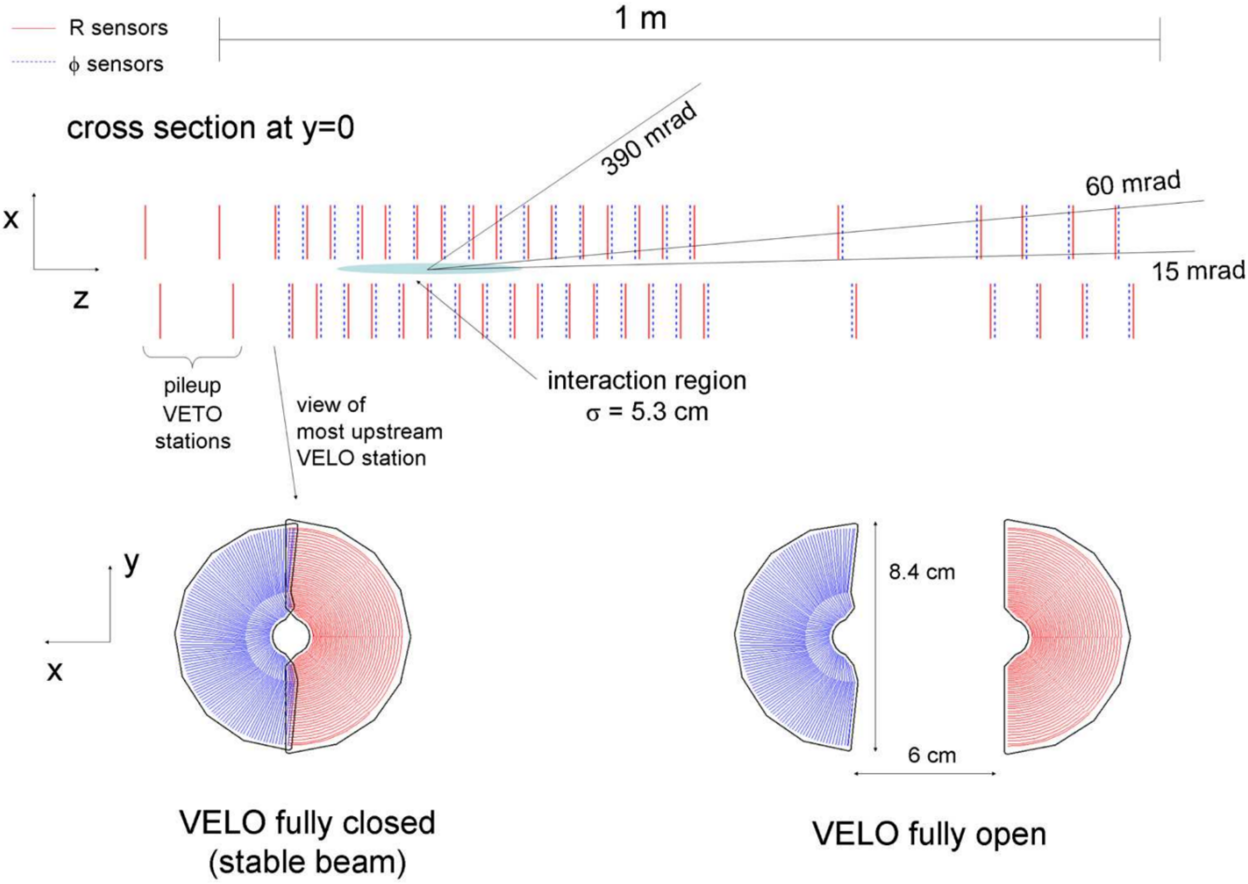

Figure 3.4: The VELO silicon sensors. Top: View from above of the silicon modules. Bottom: View in the x-y plane of a VELO module, Φ sensors (blue) and the R sensors (red). The fully closed module (left) and the fully retracted module (right). Figure from [38].

3.2.1.2 The Magnet

The LHCb Magnet [43] is located between the VELO and the tracking stations. It is a dipole magnet which creates an integrated magnetic field of 4 Tm perpendicular to the beam line. As a result, it is possible to obtain information about the momenta of charged particles passing through the magnet using the curvature of the particles' tracks. Furthermore, to reduce the impact of potential asymmetric acceptance effects, the direction of the magnetic field is repeatedly flipped such that both directions are applied in equal proportions during data taking periods.

3.2.1.3 The Silicon Tracker

The Silicon Tracker (ST) [44] includes the Tracker Turicensis (TT) and the Inner Tracker (IT) and all utilise silicon microstrips, with a pitch of approximately 200 μm, to provide single-hit spatial resolution of 50 μm. The TT and the three other composite stations of the IT all have the microstrips designed in four detection layers. The geometry of the detection layers is denoted $(x-u, v-x)$, where the x layer corresponds to vertical strips, and the u and v layers each correspond to a rotation of $-5°$ and $5°$ with respect to the x layer. Detection layers used in the TT and IT are shown in Figures 3.5 and 3.6, respectively.

The TT reconstructs all particles including those with low momentum which exit the detector acceptance when passing through the magnet, as well as longer-lived particles which decay after the VELO. Moreover, it measures the transverse momentum of tracks with a large impact parameter to provide information for the trigger. The IT covers the inner region of the T1 to T3 tracking stations where the particle flux is high compared to the outer regions.

3.2.1.4 The Outer Tracker

The Outer Tracker (OT) [45] is composed of three straw-tube drift chambers which cover the outer region of the T1-T3 tracking stations. Despite straw-tube drift chambers having a far lower granularity compared to silicon detectors, they are used in the outer tracker since the particle flux is lower compared to the inner regions and it reduces costs.

Similarly, to the TT and IT each OT station has 4 layers, and the tubes are in the same geometric configuration as the silicon strips as the ST. There are two staggered sub-layers of 4.9mm straw-tubes within each detector layer, containing a gas with a composition of 70% argon and 30% carbon dioxide. The gas mixture results in fast drift times (<50 ns) and high drift-coordinate resolution of 20μm.

3.2.1.5 Reconstruction of Tracks

The hits in the VELO, the TT and T1 to T3 are combined using track reconstruction algorithms to reconstruct the particle tracks [46] [47]. All tracks in an event with sufficient detector hits are reconstructed. There are multiple track categories dependent on which subdetector(s) they register hits in as outlined in Figure 3.7.

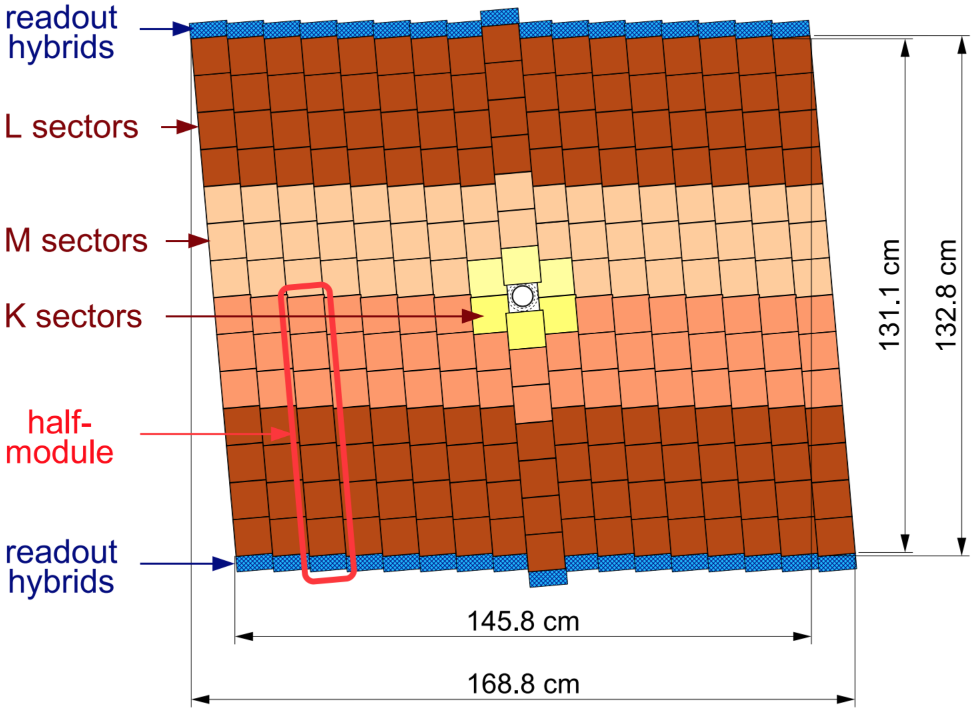

Figure 3.5: The third detection layer of the TT. The blue corresponds to the readout hybrids, the yellow represent sensors read out individually, the light brown are sensors bonded together in groups of two or three and the dark brown are sensors bonded together in groups of 4. Figure from [38].

- Long tracks: These are tracks which have traversed the entire detector with hits in all the tracking subdetectors. Thus, they have precise momentum information and defined vertices. Consequently, these are the most helpful tracks for a physics analysis.
- Upstream tracks: These tracks register hits in the VELO and TT only. This indicates they are likely to be low momentum tracks deflected outside the detector acceptance by the magnet. Therefore, they provide limited momentum information.
- Downstream tracks: These tracks register hits in the TT and T1 to T3 but are absent in the VELO. They are often tracks of the daughters of long-lived particles such as the daughters of the K_s^0 because the K_s^0 typically does not decay until after the VELO.
- T tracks: These tracks only record hits in the T1-T3 hit stations. They are frequently created in secondary interactions.
- VELO tracks: These tracks are registered in the VELO only, often because they are pointing in the backward direction or have a large angle. Although, they do not provide momentum information they are used to determine the primary vertex.

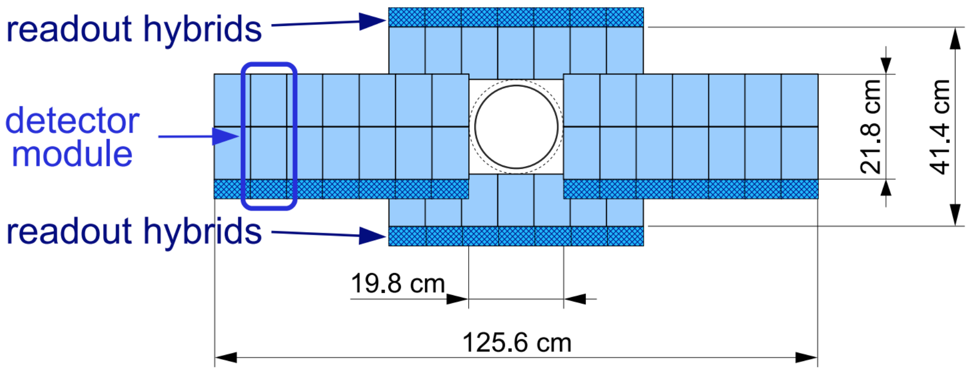

Figure 3.6: Detector layer of the second IT station in the x-y plane with the beampipe in centre. Figure from [38].

3.2.2 The LHCb Particle Identification System

LHCb employs two Ring Imaging Cherenkov (RICH) detectors , the calorimeter, and muon stations to provide particle identification capabilities [38]. The outputs from the constituents of the LHCb particle identification system are combined into particle identification variables described in Section 3.2.2.4

3.2.2.1 The RICH detectors

The key aim of the two RICH [48] detectors is to identify and separate charged pions and kaons over the entire momentum spectrum. It also provides information to identify muons, electrons and protons.

Charged particles travelling faster than the speed of light within a particular medium emit Cherenkov radiation [49]. The direction of travel of the Cherenkov photons is such that they are produced in a cone. The Cherenkov angle θ_C of photons can be defined as:

$$cos(\theta_C) = \frac{1}{n\beta} = \frac{\sqrt{m^2c^2 + p^2}}{np} \tag{3.1}$$

where n is the refractive index of the medium, $\beta = v/c$, v is the speed of the particle, c is the speed of light, m is the mass of the particle and p is the momentum of the particle. Thus, the Cherenkov angle is related to the particle's momentum as can be seen in Figure 3.8 . The RICH detectors measure the Cherenkov angle, the refractive index of each of the RICH radiators is known, and the tracking system determines the particle momentum. Therefore, the particle mass can be calculated and used to identify the particle.

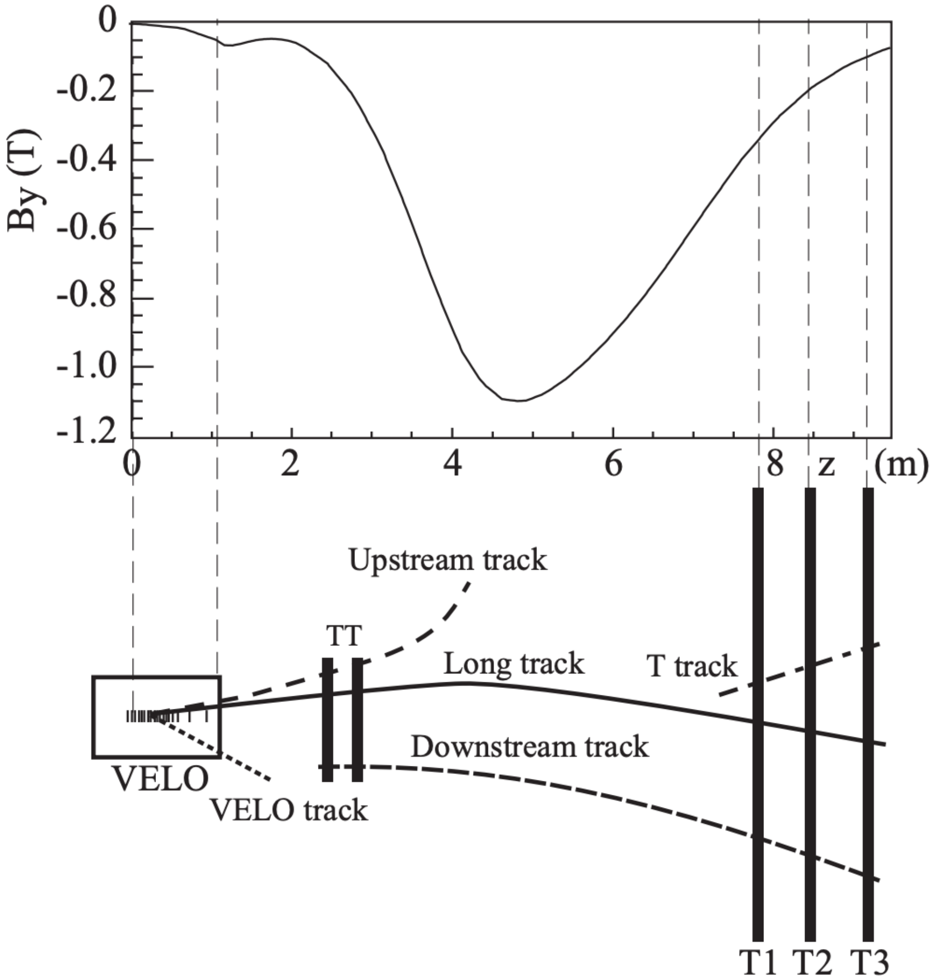

Figure 3.7: Top: The magnetic field component B_y along the beam axis (z-direction). Bottom: A schematic of the 5 different LHCb track categories. Figure from [46].

The first RICH detector (RICH1) is designed to identify low momentum particles. It encompasses the full angular acceptance of the LHCb detector, and is located between the VELO and the TT because the magnet may deflect low momentum tracks outside of the acceptance. RICH1 is used to distinguish charged particles in the momentum range between 1 GeV/c and 60 GeV/c using C_4F_{10} gas as illustrated in Figure 3.8.

The second RICH detector (RICH2) is designed to identify high momentum particles. Higher momentum particles have smaller polar angles [38], thus RICH2 has a reduced angular acceptance, compared to RICH1, of 15 mrad to 120 mrad in the horizontal (bending) plane and 15 mrad to 100 mrad in the vertical (non-bending) plane. Furthermore, RICH2 is positioned between the magnet and tracking stations since it is less probable that high momentum particles will be deflected by the magnet. RICH2 is used to discriminate between charged particles in the momentum range 15 GeV/c to 100 GeV/C using CF_4 gas as shown in Figure 3.8.

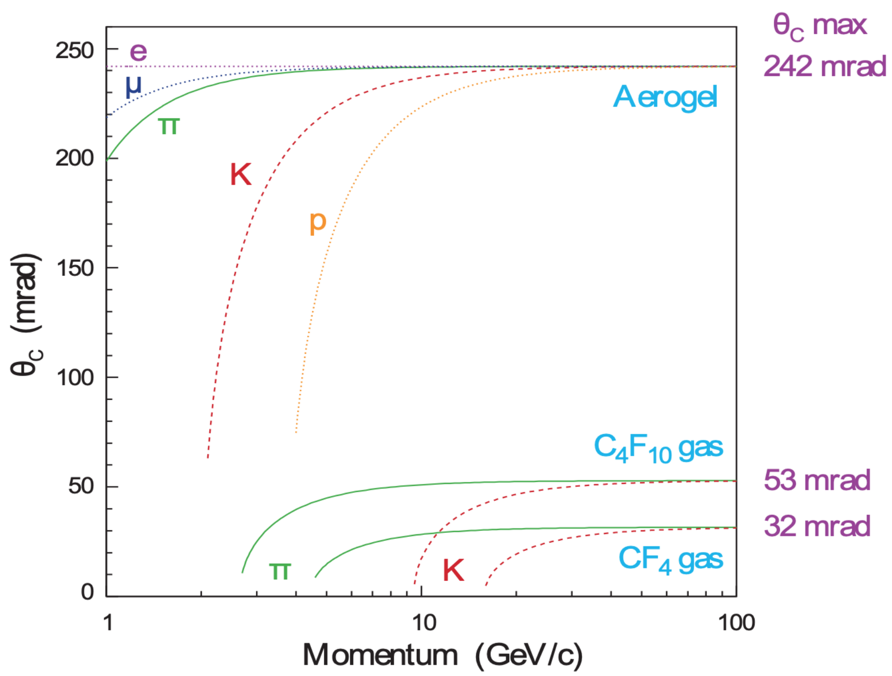

Figure 3.8: Cherenkov angle related to particle momentum for the RICH radiators. Note that silica aerogel was used in Run 1 only and removed for Run 2. Figure from [38].

Figure 3.9 shows that both RICH1 and RICH2 reflect Cherenkov photons, produced by charged particles, onto cylindrical Pixel Hybrid Photo Detectors (HPD) . This is achieved by utilising the spherical primary and flat secondary mirrors.

3.2.2.2 The Calorimeters

The LHCb calorimeter system [50] includes a Preshower detector (PS), a Scintilating Pad Detector (SPD), an electromagnetic calorimeter (ECAL) and a hadronic calorimeter (HCAL). The calorimeter is able to obtain the energy and positions of neutral particles such as π^0 particles and photons and identify them. Moreover, the calorimeter is also used to identify electrons and hadrons. The information determined by the calorimeter is an important input for the LHCb L0 hardware trigger.

The SPD and PS are made of a 15mm thick plastic scintillators and are positioned prior to the ECAL and HCAL, with a 2.5 X_0 (where X_0 is the radiation length) thick sheet of lead in between them as shown in Figure 3.10 [50]. As can be seen in Figure 3.10 only charged particles deposit energy at the SPD, then the lead converter separates electrons from back-

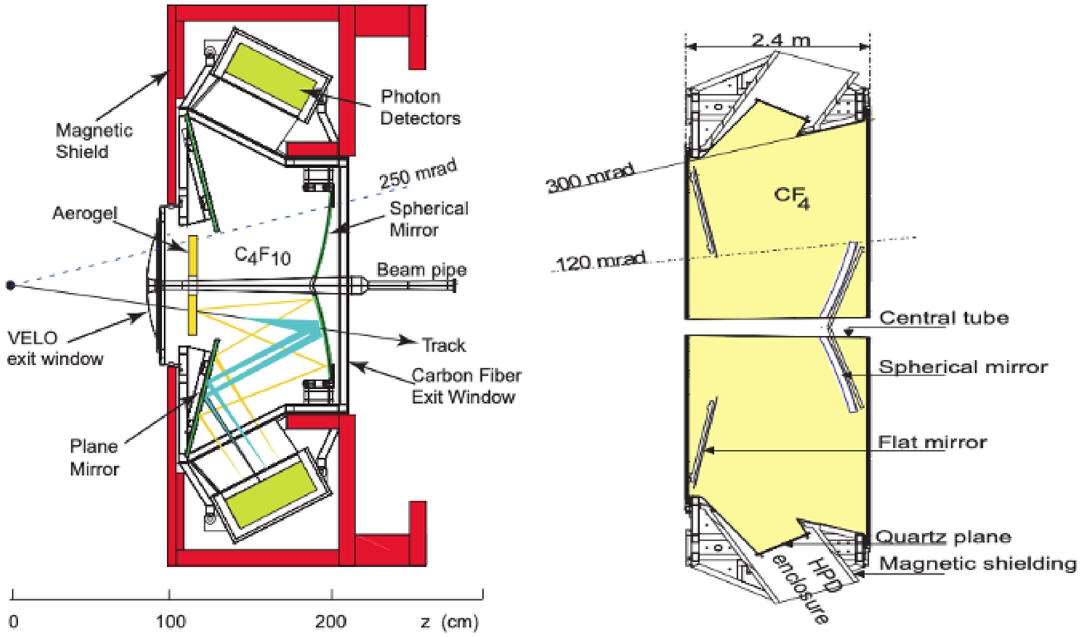

Figure 3.9: RICH1 detector (left) and RICH2 detector (right). Figures from [38].

ground pions and causes the electrons and photons to produce electromagnetic showers which deposit energy in the PS and ECAL. In order to fully contain the electromagnetic showers the ECAL is 25 X_0 thick. The ECAL has 66 alternating layers of 2mm thick lead sheets and 4mm thick polystyrene scintillators, where the scintillation light is transmitted to Photo-Multipliers (PMT) using wavelength-shifting (WLS) fibres. As well as aiding the identification of photons and electrons, the ECAL can also reconstruct neutral pions by identifying pairs of photons.

The HCAL is 5.6 λ_i (where λ_i is the radiation length) thick and arranged in alternating layers of 1cm thick iron sheets and 3mm thick doped polysterene scintillators. Hadrons interact with the nuclei of the atoms forming the iron sheet inducing hadronic showers. Scintillation light is transmitted by WLS fibres to PMTs similarly to the ECAL. The absence of a track associated to the cluster of hits in the calorimeters is used to discriminate neutral particles from charged particles.

3.2.2.3 The Muon Chambers

Muon candidates are identified using information from each of the five muon stations (M1-M5) as can be seen in Figure 3.11. This information is also used as input for muon triggering in the L0-trigger [51].

- M1: Measures the transverse momentum, hence it is placed between RICH2 and the

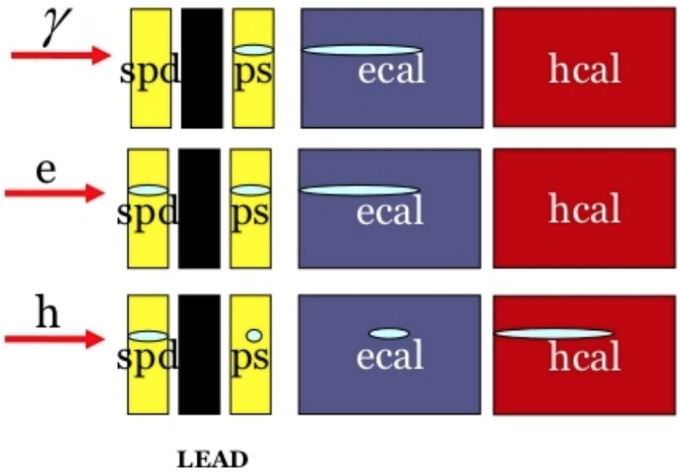

Figure 3.10: Calorimeter schematic. The lead layer is thick enough to cause electromagnetic showers. Figure from [50].

Calorimeter subdetectors.

- M2 and M3: provide high quality spacial resolution of tracks. They are positioned after the calorimeters.
- M4 and M5: Provides particle identification information. They are located after M2 and M3.
- M2 to M5: Are all separated by 80cm thick iron sheets, which stop high energy hadrons reaching the muon stations. Thus, only muons with a enough momentum reach the muon stations.

Each muon station is split into four regions (R1-R4) as can be seen in Figure 3.12. The granularity in the regions reduce radially as the expected particle density decreases. All muon stations are multi-wire proportional chambers (MWPC), apart from R1 of M1 which are triple-GEM (Gas Electron Multiplier) chambers [52] due to the expected radiation damage because of the particle rate at this point.

3.2.2.4 The Particle Identification Variables

The outputs from the subdetectors within the particle identification system are used to determine two different sets of discriminative variables for an events' final state tracks [53].

Outputs from the subdetectors for each track are compared to the expected outputs for a variety of particle species to provide a likelihood for each particle hypothesis. These likelihoods are multiplied together for each particle type and used to calculate the first set of discriminant

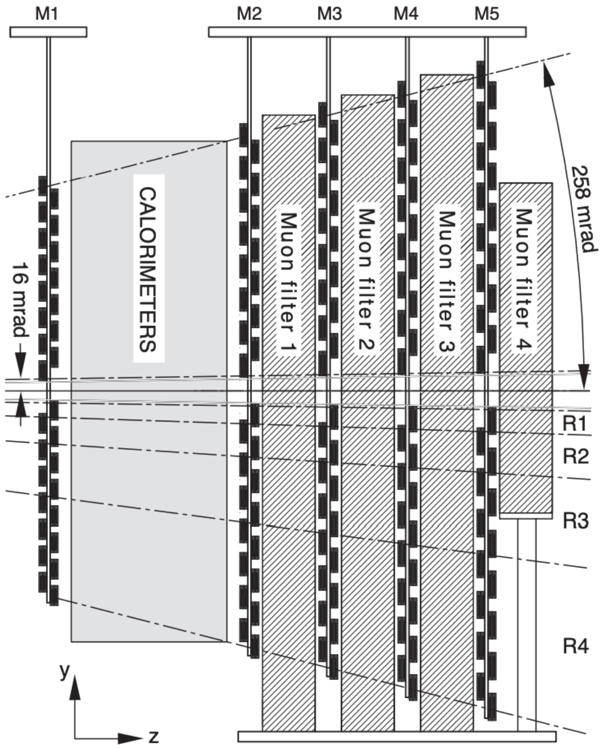

Figure 3.11: Sideview of the muon stations. Figure from [38].

variables which is the Difference in the Log Likelihood (DLL) between particular particle hypotheses X and Y :

$$DLL_{X-Y} = \log \mathscr{L}_X - \log \mathscr{L}_Y \tag{3.2}$$

where the reference particle Y is often a pion, because these are the most likely particles to be produced in $p-p$ collisions.

An artificial neural network takes a variety of inputs from PID system subdetectors and tracking system outputs including the DLL variables. The output of the neural network is the second set of discriminant variables, they are normalised between 0 and 1 and thus known as the ProbNN variables, and each one represents the probability of a particular particle hypothesis. Simulation samples resampled such that they correspond to the occupancy of events in the data are used to train the neural network.

The information from the particle identification subdetectors are combined, however it is worth noting that kaon and pion identification variables calculation largely relies on information from the RICH detectors, whilst electrons and neutral particle identification variables

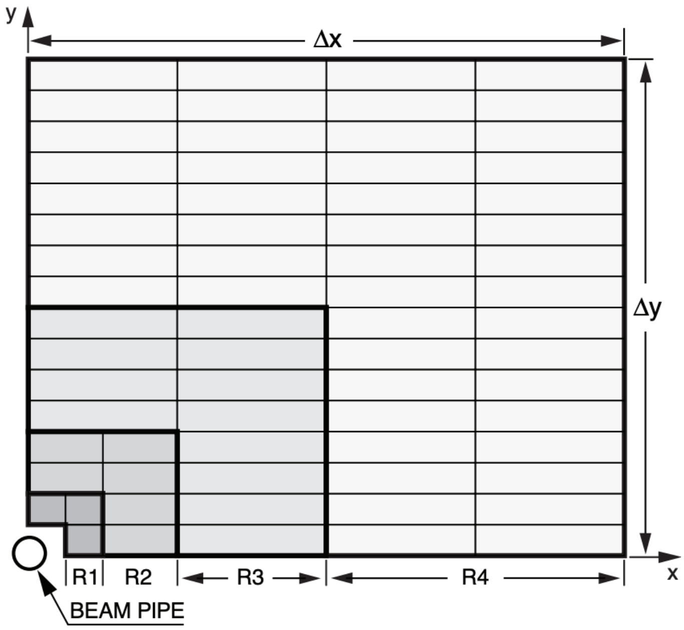

Figure 3.12: The front view of a muon station quadrant split into four regions R1 to R4. Each rectangle is a chamber. Figure from [38]

depend heavily on information from the calorimeter, and the muon particle identification variable is particularly reliant on the muon system.

3.2.2.5 LHCb Performance

The LHCb detector can achieve an impact parameter resolution of approximately $200\mu m$ and a decay time resolution of approximately $45fs$.

The average relative momentum resolution of the tracking system is:

$$\frac{\Delta p}{p} \approx 0.5\% \tag{3.3}$$

The ECAL and HCAL have relative energy resolutions of

$$\frac{\Delta E}{E} \approx \frac{10\%}{\sqrt{E[GeV/c]}} \oplus 1\% \tag{3.4}$$

and

$$\frac{\Delta E}{E} \approx \frac{80\%}{\sqrt{E[GeV/c]}} \oplus 1\% \tag{3.5}$$

respectively. Moreover, LHCb has significant kaon-pion separation power, where a kaon efficiency of approximately 95% and pion misidentified fraction of approximately 5% can be obtained for $p > 1GeV$.

3.3 The LHCb Trigger System

The maximal LHC bunch collision rate of 40 MHz is too great for every event to be reconstructed because of computing time and other data acquisition (DAQ) systems constraints. Moreover, the LHCb storage capacity would also not be sufficient to store the data in its entirety. Therefore, the LHCb trigger system is required to reduce the visible bunch crossing rate from 25 MHz to 3.5 kHz, 5 kHz and 12.5 kHz for 2011, 2012 and Run 2 respectively, using selections designed to retain as many likely B meson and Charm meson events as possible, whilst eliminating likely background events. This is achieved using the Level-0 (L0) hardware trigger and then the High Level Software Trigger (HLT) [38].

3.3.1 The LHCb Level-0 Trigger

The LHCb level-0 hardware trigger [38] cuts the bunch crossing rate from 40 MHz to 1 MHz using information from the muon stations and calorimeter which have rapid read out times (less than 4 micro seconds). B hadrons impart a large amount of transverse kinetic energy to its daughter particles. Consequently, the L0 triggers on events which have deposited high amounts of transverse energy in the calorimeter or muon stations. Moreover, the VELO and SPD provide the L0 pileup information, which is used to remove events with too large a number of tracks.

Transverse energy thresholds vary for the data taking year and different particle types - hadrons, muons, electrons and photons [55] [56] [57]. Thus, there are the L0 Hadron, L0 Photon, L0 Electron, L0 Dimoun and L0 Muon trigger lines. In this analysis the L0 Hadron line is the most important. The transverse energy threshold is the highest for the L0 Hadron line and is the sum of the transverse energy in the HCAL and corresponding ECAL cells. The trigger line is activated by clusters in the HCAL which meet the criterion.

3.3.2 The LHCb High Level Trigger

Events which are selected by the L0 hardware trigger then have to pass the software based High Level Trigger which is composed of 2 stages, the first stage is HLT1 and the second stage is HLT2 [38].

The HLT1 conducts partial event reconstruction using information from the VELO, the tracking system and the muon particle identification stations. The HLT1 line confirms the L0

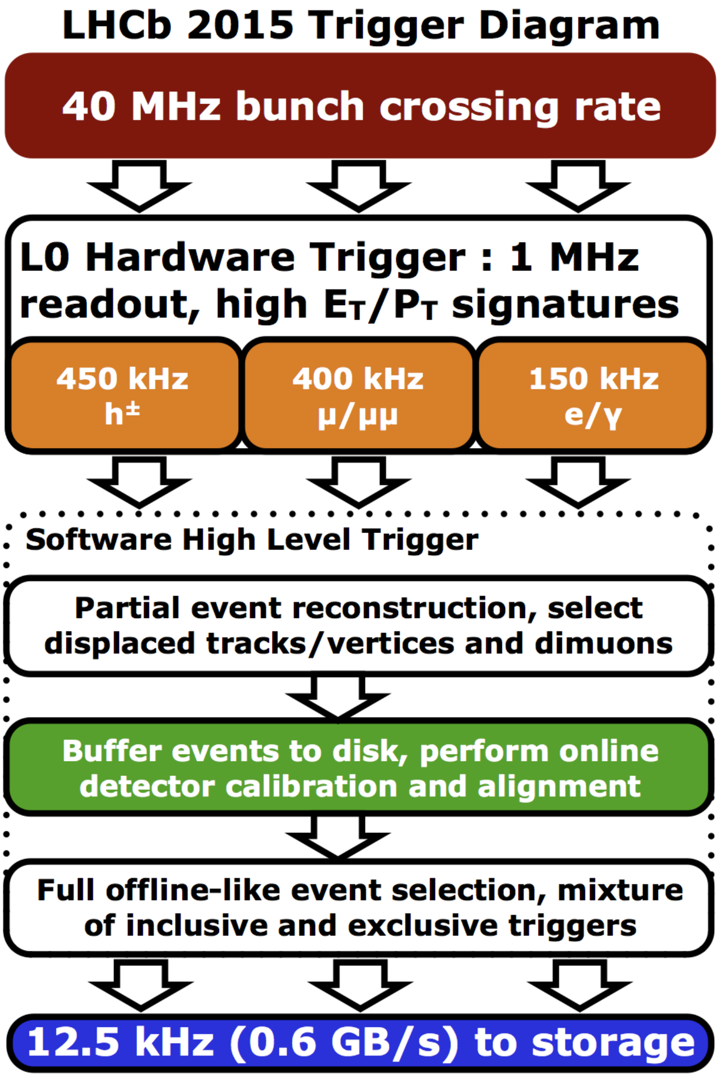

Figure 3.13: The Trigger scheme for Run 2. Figure from [54].

trigger decision by reconstructing tracks in the VELO, and identifying primary vertices and potential secondary vertices, and applying cuts on the impact parameter, momentum, transverse momentum and/or track quality. For this analysis the decays of interest are $B^{\pm} \to Dh^{\pm}$, thus the HLT1 trigger lines HLT1TrackMVA and HLT1TwoTrackMVA are applied [58]. HLT1TrackMVA triggers on events with a minimum of one track with high transverse momentum and a large impact parameter with respect to the primary vertex. HLT1TwoTrackMVA triggers on secondary vertices which are displaced from the primary vertex and formed from two tracks. The HLT1 trigger lines used in this analysis are discussed further in Section 5.2.

The HLT2 undertakes a full event reconstruction of the remaining events after HLT1 to reduce the data rate to 12.5KHz, so it can be stored permanently offline. The HLT2 uses all the detector tracking and particle identification information to reconstruct all tracks in an event, as well as intermediate particles and displaced vertices. Subsequently, a variety of sets of cuts can be applied, dependent of the HLT2 line, which are predominantly aimed at identifying B and D meson decays. This analysis uses the HLT2 trigger lines designed to identify the topology consistent with a B meson decay, these lines are known as HLT2 topological N-body lines [58]. The HLT2 topological N-body lines use a Boost Decisison Tree [59] to search for 2, 3 and 4 track vertices, with significant transverse momentum and large displacement from the primary vertex. Discrepancies between the total momentum of the N tracks and the hypothetical B meson momentum are taken into consideration, in order to compensate for missed tracks. Further information regarding BDTs can be found in section 5.6. The HLT2 trigger lines used in this analysis are discussed further in Section 5.2.

The Run 2 HLT2 event reconstruction is greatly improved due to optimised selection algorithms, upgraded computing resources, and real-time alignment and calibration of the systems within LHCb detector as illustrated in Figure 3.13. An added benefit of the real-time alignment and calibration sub-stage is that these events can be used in the Turbo stream [57], without additional offline reconstruction.

3.3.3 The LHCb Turbo Stream

In Run 2 the HLT2 reconstruction and offline reconstruction both perform identically. As a result, the candidates selected by the HLT2 can be saved to disk in the Turbo stream [60] and used directly, without additional offline reconstruction by Brunel outlined in Section 3.5. This functionality is achievable because of the real-time alignment and calibration of the detector. This is useful if all the reconstructions required for an analysis have already been undertaken by HLT2. However, some physics objects for example tracks and vertices or detector responses that aren't used by the trigger to form part of the selected decay are removed. The physics objects used to reconstruct candidates selected by the trigger are saved for the Turbo lines, which are analogous to the HLT2 lines. The software TESLA, outlined in Section 3.5, processes the Turbo stream events by extracting the physics objects reconstructed in HLT2 and converts them for physics analysis.

3.4 The LHCb Stripping

A stripping line is a set of loose cuts designed to check that an event has candidates which can be combined to form the signal decay in question. Their purpose is to retain a high proportion of signal events, whilst eliminating as many background events as possible. The stripping is required to shorten computing time. The LHCb software DaVinci executes the stripping, this is discussed further in Section 3.5. The stripping lines used in this analysis of $B^{\pm} \to D(\to 2\pi^{+}2\pi^{-})h^{\pm}$ decays, is B2D0PiD2HHHH to select $B^{\pm} \to D\pi^{\pm}$ decays and B2D0KD2HHHH to select $B^{\pm} \to DK^{\pm}$ decays, with the D meson decaying to a 4-body hadronic final state. The stripping is discussed in more detail in Section 5.3.

3.5 The LHCb Software

A variety of software frameworks, integrated into the Gaudi framework, process data at LHCb [61] [62]. A different application is responsible for each stage of data event processing, and the main applications are detailed below. GAUSS and BOOLE are used to produce simulated data, which can then be treated the same as real data. Subsequently, MOORE, BRUNEL, (TESLA) and DAVINCI are responsible for event reconstruction.

- GAUSS: is a simulation application which generates particles and simulates the subsequent detector response [63] . Within the application Pythia [64] generates the proton-proton collisions creating $b\bar{b}$ quark pairs, EvTGen [65] then describes the B meson decay in question and the detector response to the particles is simulated using Geant4 [66] [67].

- BOOLE: receives the Gauss output and simulates the digitisation of the data output from the subdetectors, to provide the identical format to the the LHCb data from the output of LHCb DAQ system.

- MOORE: whilst data taking occurs online subdetector and global reconstruction in HLTT1 and HLT2 is undertaken by Moore. The offline reconstruction undertaken by BRUNEL is the same as the reconstruction in MOORE for Run 2.

- BRUNEL: uses pattern recognition to undertake offline subdetector and global reconstruction for data and Monte Carlo. When BRUNEL undertakes global reconstruction on Monte Carlo it associates reconstructed tracks with the particles generated in Gauss. This procedure is called truth matching, if it is not possible to match a track reconstructed in BRUNEL to a generated particle (from Gauss) it is classed as a Ghost track and provided the particle identification number 0. The treatment of Ghost tracks is discussed further in Section 5.5.1.

- TESLA: uses the physics objects created by Moore in HLT2 to process the events in the Turbo stream.

- DAVINCI: performs offline analysis including executing the stripping and reconstruction of defined decay chains of particles [68]. Following this full offline analysis can be undertaken. When DaVinci is applied to simulated data it assigns a background category to each event. A reconstructed decay chain which meets the threshold of overlapping hits to the identical decay chain in the generated Monte Carlo (from Gauss), would be classified as a signal category and thus receives the Background category identification 0. Use of background categories is discussed in Section 5.5.1.

CHAPTER 4

SENSITIVITY STUDY

The sensitivity to CKM angle γ is established using pseudo-experiments. This Chapter outlines the sensitivity study strategy, the choice of fit parameters used, the predicted sensitivity to CKM angle γ for LHCb Run 1 + Run 2 dataset and the resulting choice of binning scheme for the D meson decay phase space used in the further measurement.

4.1 Sensitivity Study Strategy

The $D \to 2\pi^+2\pi^-$ decay has a 5 dimensional phase space which is divided into bins and γ or $x_\pm$ and $y_\pm$ are measured in every bin. The number of signal events are calculated in each bin i, where the total number of bins is n_{bins}. The total number of bins is derived from there being i positive bins and i negative bins for each B charge. The number of signal events in each of the $\frac{n_{bins}}{2}$ $B^- \to D(\to 2\pi^+2\pi^-)K^-$ decay bins and in each of the $\frac{n_{bins}}{2}$ $B^+ \to D(\to 2\pi^+2\pi^-)K^+$ decay bins are calculated using:

$$N_i^{B^-} \to DK^- = h_{B^-}(T^f_{-i}r_B^2 + T^f_i + 2\sqrt{T^f_i T^f_{-i}}(c^f_i x_- + s^f_i y_-)) \tag{4.1}$$

and

$$N_i^{B^+} \to DK^+ = h_{B^+}(T^f_i r_B^2 + T^f_{-i} + 2\sqrt{T^f_i T^f_{-i}}(c^f_i x_+ - s^f_i y_+)), \tag{4.2}$$

where the CKM angle γ is a constituent in $x_\pm = r_B cos(\delta_B \pm \gamma)$ and $y_\pm = r_B sin(\delta_B \pm \gamma)$, and h_{B^-}, h_{B^+} are independent proportionality constants, and T^f_i c^f_i and s^f_i are the hadronic parameters previously measured using CLEO-c data [36].

Table 4.1: The expected total $B^{\pm} \to D^0(\to 2\pi^+2\pi^-)K^{\pm}$ event yields for LHCb data taking periods.

Data taking Period	Expected $B^{\pm} \to D^0(\to 2\pi^+2\pi^-)K^{\pm}$ Yields
Run 1	1500
2016	2200
Run 1 + Run 2	9000
Future	20000

The expected total $B^{\pm} \to DK^{\pm}$, $D \to 4\pi^{\pm}$ event yield at LHCb for Run 1, 2016, combined Run 1 and Run 2, and in future are estimated and laid out in Table 4.1. The expected total Run 1 and 2016 yields are from [69], and the Run 2 and future yields are extrapolated from the 2016 yield using expected integrated luminosity for the data taking periods. The sensitivity study strategy in each pseudo-experiment is as follows:

- The number of signal events in each bin are predicted by equations 4.1 and 4.2, with $r_B = 0.1$, $\delta_B = 143°$, $\gamma = 73.5°$. The independent normalisation parameters are calculated, such that the total number of $B^{\pm} \to D(\to 2\pi^+2\pi^-)K^{\pm}$ decays corresponds to the expected total yield for the data taking period in question. The predicted number of signal events in each bin are randomly fluctuated according to the Poisson distribution.

- The Poisson fluctuated event yields in each bin are used to generate Gaussian $B^{\pm}$ mass distributions. Hence, the number of $B^{\pm}$ mass distributions generated (n_{gauss}), is the same as the number of bins (n_{bins}).

- A simultaneous extended maximum-likelihood fit to all n_{gauss} mass peaks is then implemented. Separate fits are performed for parameters $\{x_{\pm}, y_{\pm}\}$ and $\{\gamma, \delta_B, r_B\}$ respectively- these parameters and the independent normalisation parameters are permitted to float in the fit.

- The fits are performed with two different hadronic parameter settings: one in which the hadronic parameters (T_i^f c_i^f and s_i^f) are fixed, and one in which they are constrained according to their uncertainties and correlation. The constrained hadronic parameters are varied according to their covariance matrix.

- In the case of the fixed hadronic parameters the uncertainties from the fit on γ or $x_{\pm}$, $y_{\pm}$ are the statistical uncertainties $\sigma(stat)$. Whereas, when the hadronic parameters are constrained the uncertainties from the fit on γ or $x_{\pm}$, $y_{\pm}$ are the combination of $\sigma(stat)$ and hadronic parameter uncertainties $\sigma(had)$.

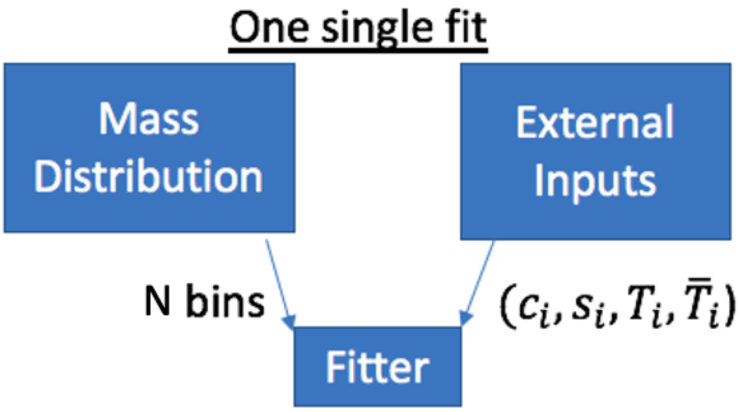

Figure 4.1: Mechanics of the single fit using generated mass distributions and hadronic inputs previously measured from CLEO-c data [36].

4.2 Bias Studies

Both the fits for $\{\gamma, \delta_B, r_B\}$ and $\{x_{\pm}, y_{\pm}\}$ are investigated for bias using pull studies of 100 pseudo-experiments for the expected combined Run 1 and Run 2 event yields laid out in Table 4.1. All five binning schemes, with n_{bins} = 20, were implemented as outlined in Section 2.5. In the case of fixed hadronic parameter inputs no bias is observed in any of the pulls in either $\{\gamma, \delta_B, r_B\}$ and $\{x_{\pm}, y_{\pm}\}$ fits. However, when the hadronic parameter inputs are constrained in the $\{\gamma, \delta_B, r_B\}$ fit, significant bias in the r_B parameter is observed in all the binning schemes as can be seen in Table 4.2. The least bias is found in the Equal $\Delta\delta_p^{4\pi}$ binning and the largest bias in the Alternate binning. The fit for $\{x_{\pm}, y_{\pm}\}$, with constrained hadronic parameters, establishes potential small bias in the Equal $\Delta\delta_p^{4\pi}$, Optimal-alternative and Optimal binning schemes and finds significant bias in y_- in the Variable $\Delta\delta_p^{4\pi}$ and Alternate binning schemes as shown in Table 4.3.

To investigate both the stark difference in bias between the two fitters and bias between the binning schemes, likelihood scans for 1 pseudo-experiment and the Run1+Run2 event yield were used. Figure 4.2 highlights the ambiguities arising from the cosine and sine terms in the fit for $\{\gamma, \delta_B, r_B\}$- the two primary maxima in both plots are to be expected from the cyclical nature of the trigonometric terms, whilst the two secondary maxima in the Alternate binning scheme were more prevalent than in the Equal $\Delta\delta_p^{4\pi}$ binning scheme. Hence, the reduced performance in the Alternate binning scheme case.

The likelihood scans for the $\{x_{\pm}, y_{\pm}\}$ fit in Figure 4.3 demonstrates how replacing the trigonometric and r_B terms with the $x_{\pm}$ and $y_{\pm}$ eliminates the ambiguities in the Equal $\Delta\delta_p^{4\pi}$ binning. Thus, the improved performance of the $\{x_{\pm}, y_{\pm}\}$ fit. However, the multiple peaks remaining in

Table 4.2: Pulls results, from 100 pseudo-experiments for the fit for $\{\gamma, \delta_B, r_B\}$ and $n_{bins} = 20$.

Bias Studies for $\{\gamma, \delta_B, r_B\}$.						
Binning scheme	γ mean	γ width	δ_B mean	δ_B width	r_B mean	r_B width
Equal $\Delta\delta_p^{4\pi}$	0.106 $\pm$0.1075	1.075 $\pm$0.0764	0.168 $\pm$0.1185	1.185 $\pm$0.0842	0.4385 $\pm$0.0877	0.877 $\pm$0.0623
Variable $\Delta\delta_p^{4\pi}$	-0.602 $\pm$0.1725	1.725 $\pm$0.1226	-0.181 $\pm$0.2591	2.591 $\pm$0.1841	-0.456 $\pm$0.0870	0.870 $\pm$0.0618
Optimal-alternative	0.189 $\pm$0.1052	1.052 $\pm$0.0748	0.058 $\pm$0.2025	2.025 $\pm$0.1439	0.644 $\pm$0.0872	0.872 $\pm$0.0620
Optimal	0.024 $\pm$0.1926	1.926 $\pm$0.1369	0.139 $\pm$0.2043	2.043 $\pm$0.1452	0.581 $\pm$0.1061	1.061 $\pm$0.0754
Alternate	-0.257 $\pm$0.1963	1.963 $\pm$0.1395	0.031 $\pm$0.2615	2.615 $\pm$0.1858	-0.660 $\pm$0.1063	1.063 $\pm$0.0755

Table 4.3: Pulls results, from 100 pseudo-experiments for the fit for $\{x_\pm, y_\pm\}$ and $n_{bins} = 20$.

Bias Studies for CP observables								
Binning scheme	x_+ mean	x_+ width	x_- mean	x_- width	y_+ mean	y_+ width	y_- mean	y_+ width
Equal $\Delta\delta_p^{4\pi}$	0.021 $\pm$0.0956	0.956 $\pm$0.0679	0.079 $\pm$0.0915	0.915 $\pm$0.0650	0.105 $\pm$0.0965	0.965 $\pm$0.0686	0.279 $\pm$0.0967	0.967 $\pm$0.0687
Variable $\Delta\delta_p^{4\pi}$	0.068 $\pm$0.1119	1.119 $\pm$0.0795	0.003 $\pm$0.0878	0.878 $\pm$0.0624	-0.069 $\pm$0.1052	1.052 $\pm$0.0748	-0.573 $\pm$0.1444	1.444 $\pm$0.1026
Optimal-alternative	-0.141 $\pm$0.0867	0.867 $\pm$0.0616	0.062 $\pm$0.1127	1.127 $\pm$0.0801	-0.083 $\pm$0.1034	1.034 $\pm$0.0735	0.109 $\pm$0.1020	1.020 $\pm$0.0725
Optimal	-0.169 $\pm$0.0924	0.924 $\pm$0.0657	-0.008 $\pm$0.0996	0.996 $\pm$0.0708	-0.042 $\pm$0.1007	1.007 $\pm$0.0716	0.061 $\pm$0.1031	1.031 $\pm$0.0733
Alternate	0.057 $\pm$0.0988	0.988 $\pm$0.0695	0.125 $\pm$0.0921	0.921 $\pm$0.0654	0.026 $\pm$0.1362	1.362 $\pm$0.0968	-0.467 $\pm$0.1698	1.698 $\pm$0.1207

Alternate binning scan provide a reason for its reduced performance even in the $\{x_\pm, y_\pm\}$ fit.

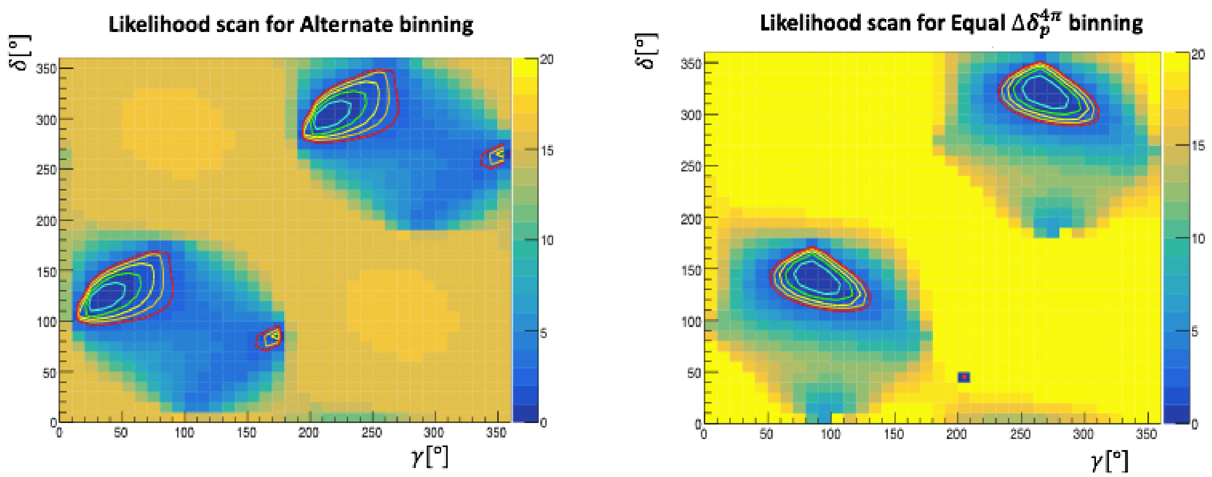

Figure 4.2: γ versus δ_B scans of $-2(\log(\mathscr{L}) - \log(\mathscr{L}_{max})$, with 10° intervals, for 1 pseudo-experiment, Run1+Run2 yield and Alternate binning scheme (left) and Equal $\Delta\delta_p^{4\pi}$ binning scheme (right) with $n_{Bins} = 20$.

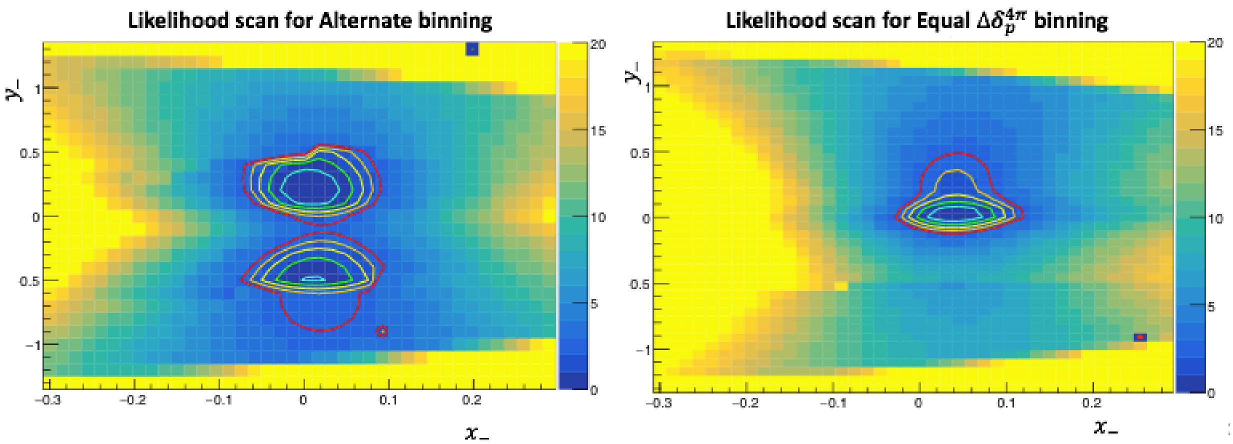

Figure 4.3: x_- versus y_- scans of $-2(\log(\mathscr{L}) - \log(\mathscr{L}_{max})$, with 0.01 intervals, for 1 pseudo-experiment, Run1+Run2 yield and Alternate binning scheme (left) and Equal $\Delta\delta_p^{4\pi}$ binning scheme (right) with $n_{Bins} = 20$.

4.3 Sensitivity

The sensitivity to $x_\pm$ and $y_\pm$, is established from fits to 100 pseudo-experiment datasets simulated as described above.

4.3.1 Sensitivity for data taking periods

The sensitivity to $x_\pm$ and $y_\pm$ as well as γ for each data taking period in Table 4.1 is established for the three least bias binning schemes with $n_{bins} = 20$ discussed in the previous Section.

The errors are lower when the hadronic parameters are fixed compared to when they are constrained as illustrated in Figures 4.4 and 4.5. Figures 4.4 and 4.5 also demonstrate that the sensitivity to $x_\pm$ and $y_\pm$ as well as the statistical sensitivity to γ is expected to improve with greater event yields.

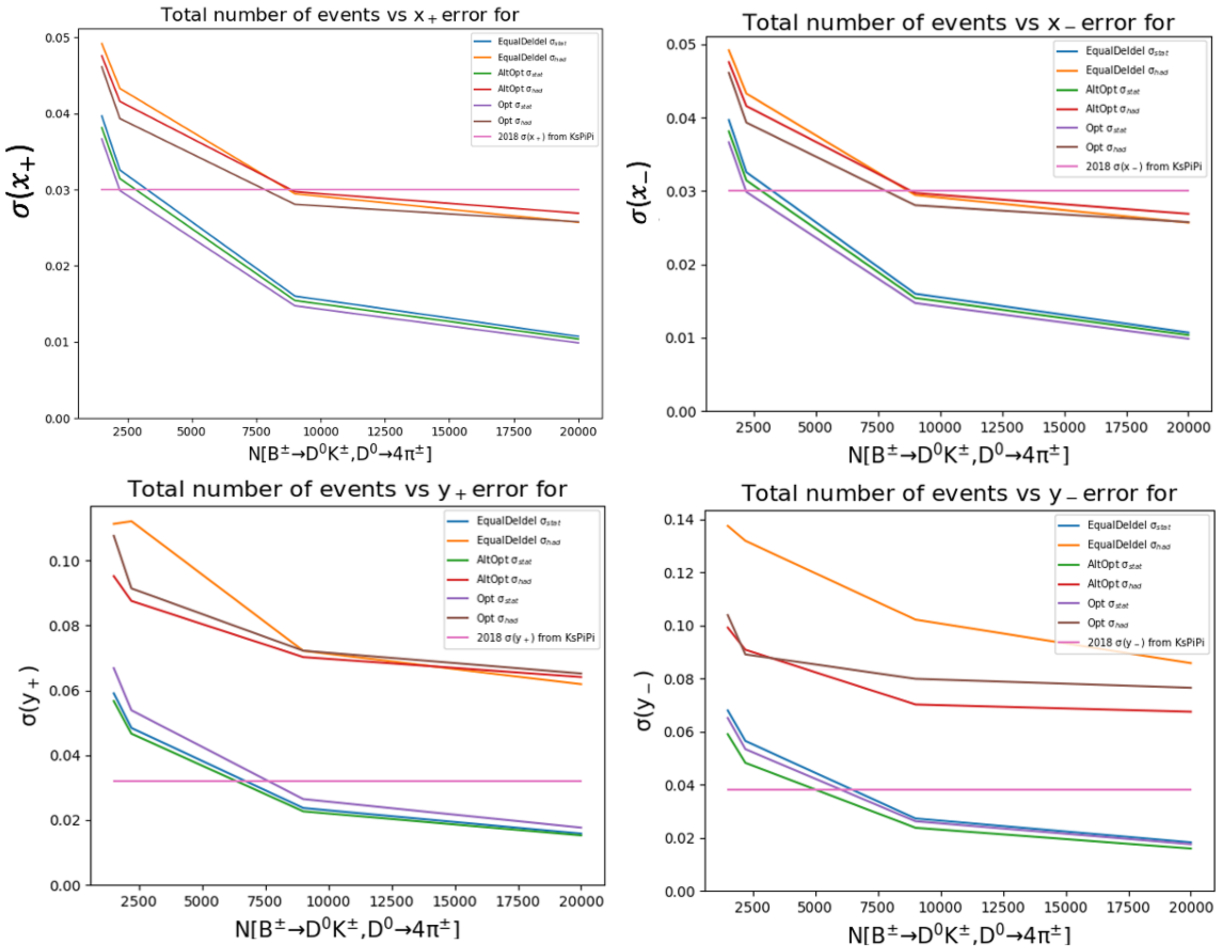

Figure 4.4: Investigation into $x_\pm$ and $y_\pm$ sensitivity based on 100 pseudo-experiments and data taking period yields in Table 4.1 for the Equal $\Delta\delta_p^{4\pi}$, Optimal-alternative and Optimal binning schemes with and without constrained hadronic parameters and n_{bins}=20. Values determined without MINOS.

4.3.2 Sensitivity for Run 1 + Run 2 Yield

The sensitivity to $x_\pm$ and $y_\pm$, for the combined expected Run 1 and Run 2 event yield are determined for the three least biased binning schemes and their associated total number of bins. The Optimal-alternative with n_{bins} = 12, Optimal with n_{bins} = 16 and Optimal with n_{bins}

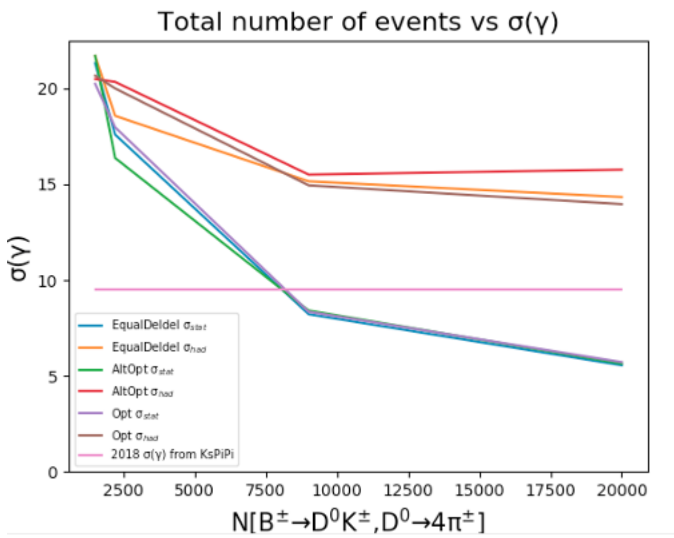

Figure 4.5: Investigation into γ sensitivity based on 100 pseudo-experiments and data taking period yields in Table 4.1 for the Equal $\Delta\delta_p^{4\pi}$, Optimal-alternative and Optimal binning schemes with and without constrained hadronic parameters n_{bins}=20. Values determined without MINOS.

= 20 binning schemes are the three most sensitive binning schemes as shown in Table 4.4. As all three binning schemes have similar sensitivity the Optimal-alternative with n_{bins} = 12 binning scheme is chosen as the binning scheme for the measurement since it has fewer bins and is more straightforward. Table 4.4 shows that the expected sensitivity using the Optimal-alternative with n_{bins} = 12 binning scheme are $\sigma(x_+)$ = 0.03258, $\sigma(x_-)$ = 0.03128, $\sigma(y_+)$ = 0.1018, $\sigma(y_-)$ = 0.06993. No significant bias is observed in pull studies for the Optimal-alternative with n_{bins} = 12 binning scheme.

Figure 4.5 shows that at the expected combined Run 1 and Run 2 event yield all the n_{bins} = 20 binning schemes, with their respective fixed/constrained hadronic inputs, have similar sensitivity to γ. Hence, it appears a sensitivity to γ of approximately 15° is achievable for the Run 1 + Run 2 dataset.

Table 4.4: Sensitivity study results from 100 pseudo-experiments for the CP observables across the Equal $\Delta\delta_p^{4\pi}$, Optimal-alternative and Optimal binning schemes, with constrained hadronic parameters and varying total number of bins in each binning scheme. Values determined with MINOS.

CP observables sensitivity study				
Number of bins	x^+ error	x^- error	y^+ error	y^- error
Equal $\Delta\delta_p^{4\pi}$ binning scheme				
20	0.02954	0.03049	0.1162	0.1578
16	0.03385	0.04020	0.2999	0.3281
12	0.03533	0.03594	0.2783	0.3551
8	0.04683	0.05205	0.2802	0.3297
4	0.04892	0.02865	0.1432	0.1045
Optimal-alternative binning scheme				
20	0.02568	0.03980	0.1187	0.07159
16	0.03122	0.03550	0.1011	0.1249
12	0.03258	0.03128	0.1018	0.06993
8	0.05260	0.05769	0.3006	0.2637
4	0.07061	0.1582	0.2851	0.1481
Optimal binning scheme				
20	0.02559	0.03033	0.0741	0.1012
16	0.02915	0.03639	0.05319	0.1127
12	0.03629	0.03342	0.2079	0.1549
8	0.03853	0.04162	0.2251	0.1963
4	0.08214	0.07485	0.2482	0.2308

Chapter 5

Selection and background Studies

The event candidates have selections applied at the trigger and stripping line levels prior to a set of offline rectangular cuts known as preselections. After this a multi-variate method known as a Gradient Boosted Decision Tree is used to remove combinatorial background. Finally, further cuts for particle identification and background suppression are applied. These selections are discussed further in this Chapter and are based on the following variables:

- χ^2 - the χ^2/ndf of the track fit associated to the particle.
- χ^2_{vtx} - the χ^2_{vtx}/ndf of the decay vertex fit of the particle.
- χ^2_{IP} - the difference in χ^2 between the primary vertex (PV) reconstruction with and without the particle under consideration. Small χ^2_{IP} values indicate the track is likely to have originated from the PV which means it is likely a prompt track [70].
- χ^2_{SV} - the displaced vertex fit quality.
- p_T - the transverse momentum.
- p - the particle momentum.
- $DLL_{K-\pi}$ - The log-likelihood difference between the K and π hypotheses
- m_D - the invariant mass of D meson candidates.
- $m_{B^\pm}$ - the mass of B meson candidates.
- P_{ghost} - Probability that a track is a ghost.

- $\tau_{B^{\pm}}$ - the decay time of the B meson.
- χ^2_{FD} - the χ^2 of the flight distance of a particle, is defined as:

$$\chi^2_{FD} = \frac{FD^2}{\sigma^2_{FD}}, \tag{5.1}$$

  where FD is the flight distance of the particle, and is the distance between its primary vertex and decay vertex. The uncertainty on the particles flight distance is denoted σ_{FD}.
- FD_{sig_z} - the significance of the flight distance in the z direction, is calculated as:

$$FD_{sig_z} = \frac{z^{particle}_{decay\ vtx} - z^{particle}_{origin\ vtx}}{\sqrt{\sigma^2(z^{particle}_{decay\ vtx}) + \sigma^2(z^{particle}_{origin\ vtx})}} \tag{5.2}$$

  where $z^{particle}_{origin\ vtx}$ is the z coordinate of the point of origin and $z^{particle}_{decay\ vtx}$ is the z coordinate of the decay vertex of the particle in question.
- $DIRA$ (cosine DIRection Angle) - is the cosine of the angle between momentum vector of the particle and its direction vector from the origin vertex to the decay vertex. It is the defined by $(x_D - x_O) \cdot p/(|p||x_D - x_O|)$, for a particle with origin vertex x_O, decay vertex x_D, and momentum p.
- Δ_{vtx_z} - the difference between the z position of the decay vertex and the origin vertex of a particle.
- $sign(\Delta_{vtx_z})FD$ - the flight distance of a particle with sign associated with the difference between the z position of the decay vertex and the origin vertex of a particle.
- I_{PT} - is the p_T asymmetry isolation variable defined as:

$$I_{PT} = \frac{B^{\pm}_{PT} - (\sum other_{\hat{p}_T})}{B^{\pm}_{PT} + (\sum other_{\hat{p}_T})} \tag{5.3}$$

  where B_{PT} is the transverse momentum of the B meson and $\sum other_{\hat{p}_T}$ is the sum of the transverse momentum vectors for all charged tracks that are not related to the signal decay within a cone shaped region. The cone is defined by a circle of radius 1.5 units constructed around the B mesons decay vertex in the pseudorapidity and azimuthal angle plane. As a result, the asymmetry isolation variable determines how isolated a particle is within the cone. A I_{PT} nearer to 1 indicates fewer other charged tracks near the B candidate and thus it's more likely to be reconstructed correctly [71].

- $ISmuon$ - If $ISmuon == 0$ the particle in question is likely not a muon, whereas if $ISmuon == 1$ the particle is likely a muon. A track is classed as $ISmuon == 1$ if it has a minimum number of hits in the muon stations [72].

5.1 Data and Simulation Samples

5.1.1 Data samples

The analysis is based on the 2017 LHCb dataset corresponding to ≈ 1.8 fb^{-1} integrated luminosity. The $B^{\pm} \to D(\to 2\pi{+}2\pi{-})h^{\pm}$ candidates were selected using lines in the Beauty2Charm stripping stream:

- $B^{\pm} \to D(\to 2\pi{+}2\pi{-})K^{\pm}$: B2D0KD2HHHHBeauty2CharmLine
- $B^{\pm} \to D(\to 2\pi{+}2\pi{-})\pi^{\pm}$: B2D0PiD2HHHHBeauty2CharmLine

5.1.2 Simulation samples

Filtered simulation (where simulated events are prefiltered by the selections in Table 5.1) $B^{\pm} \to D(\to 2\pi{+}2\pi{-})h^{\pm}$ decay modes samples are generated with a non-resonant amplitude model for the D decay. Thus, to ensure the simulation samples model the data accurately the B^{+} and B^{-} simulation samples are reweighted using D^0 and $\bar{D^0}$ amplitudes respectively from the $D^0 \to 2\pi^+2\pi^-$ amplitude model [73].

Separately, the relevant partially reconstructed background simulation samples outlined in Reference [29] are used. They contain partially reconstructed background samples with $D \to K_s^0\pi^+\pi^-$, where the long-long K_s^0 decays to $\pi^+\pi^-$, therefore they decay to the same final state as $D \to 2\pi^+2\pi^-$. The K_s^0 decays have a short flight distance which means that $D \to K_s^0\pi^+\pi^-$ is very similar to $D \to 2\pi^+2\pi^-$ and are an adequate proxy since the differences between the D decays is not critical to the modelling of the partially reconstructed backgrounds (the missing final state particles are more important).

The simulation samples are used for various purposes including selection efficiencies, multivariate analysis tool training and testing, and to aid the modelling of background and signal decays.

5.2 Trigger Event Selection

As explained in Section 3.3 there are three trigger steps applied to event candidates - one hardware and two software steps- in the LHCb data acquisition. In each step a selection is chosen.

Step 1 is the L0 hardware level trigger where the trigger decision is either:

- Trigger-On-Signal (TOS) when signal candidates activate the L0 Hadron line.
- Trigger-Independent-of-Signal (TIS) when particles not associated with the signal decay activate the L0 Global line.

Step 2 is the first software level trigger HLT1 where the signal candidates must trigger either:

- HLT1 TrackMVA line [74] where a rectangular selection is applied to the p_T, χ^2_{IP} and χ^2_{track} of the track, prior to a multivariate analysis tool which distinguishes between signal candidates and background events in the plane defined by χ^2_{IP} and p_T. Events are selected if they have a minimum of one track that pass the selection criterion set by the line.
- HLT1 TwoTrackMVA line which selects events where two tracks that form a vertex are displaced with respect to the primary vertex. A similar approach is taken to HLT1 TrackMVA, however after rectangular selection criteria are applied to each individual track a further selection criterion is placed on two track combinations such as χ^2 and p_T. Finally, a multivariate analysis tool is applied again.

Step 3 is the second software level trigger HLT2 where the Topological lines [74] are designed to trigger on 2-body, 3-body or 4-body B decays with a minimum of 2 charged children and take into account possible missing child particles. Therefore, signal candidates need to trigger either:

- HLT2 Topological 2-body TOS line which triggers on 2 body B decays as described above. Full event reconstruction is undertaken in HLT2, thus information such as all tracks and possible displaced vertices for the entire signal decay can be evaluated. First a rectangular selection is applied by the line on charged particle track variables for example χ^2_{IP} and p_T and displaced vertices variables such as χ^2_{SV}. Following this, a multivariate analysis tool known as MatrixNet [75] is used to distinguish between signal candidates and background events.
- HLT2 Topological 3-body TOS line which triggers on 3 body B decays as described above and follows similar selections to the 2 body case.
- HLT2 Topological 4-body TOS line which 4 body triggers on 4 body B decays as described above and follows similar selections to the 2 body case.

5.3 Stripping

The LHCb stripping is a central offline selection procedure.

In this analysis $B^{\pm} \to D(\to 2\pi^{+}2\pi^{-})h^{\pm}$ candidates are selected using stripping lines in the Beauty2Charm stripping streams:

- $B^{\pm} \to D(\to 2\pi^{+}2\pi^{-})K^{\pm}$: B2D0KD2HHHHBeauty2CharmLine which selects $B^{\pm} \to DK^{\pm}$ decays where the D meson decays to a four-body hadronic final state.
- $B^{\pm} \to D(\to 2\pi^{+}2\pi^{-})\pi^{\pm}$: B2D0PiD2HHHHBeauty2CharmLine which selects $B^{\pm} \to D\pi^{\pm}$ decays where the D meson decays to a four-body hadronic final state.

The stripping lines first attempt to reconstruct the D meson candidate from $2\pi^{+}$ and $2\pi^{-}$ candidates, then the D meson of this composition is combined with a $K^{\pm}$ candidate (in the B2D0KD2HHHHBeauty2CharmLine case) or $\pi^{\pm}$ candidate (in the B2D0PiD2HHHHBeauty2CharmLine case) to reconstruct the B meson candidate. The selection criteria for the LHCb stripping lines of $B^{\pm} \to D(\to 2\pi^{+}2\pi^{-})h^{\pm}$ are given in Table 5.1.

5.4 Kinematic Fitting

The DecayTreeFitter (DTF) algorithm [76], within the LHCb reconstruction software DaVinci, refits the entire decay chain trees in terms of vertex positions, decay times and momentum parameters simultaneously with further constraints added and applied. In the analysis the mass of the D meson is constrained to its PDG value [77], and the B meson candidate is constrained according to its momentum vector originating from the primary vertex . Consequently, this ensures improved resolution of the B mass and accurate reconstruction of the positions of $B^{\pm} \to D(\to 2\pi^{+}2\pi^{-})K^{\pm}$ and $B^{\pm} \to D(\to 2\pi^{+}2\pi^{-})\pi^{\pm}$ events in the $4\pi^{\pm}$ phase space and thus, associated bin number.

5.5 Preselections

After the trigger and stripping levels, a set of largely loose rectangular selections are applied in order to retain as many signal candidates as possible whilst eliminating candidates which are highly likely to be background. All the preselection cuts in this section are outlined in Table 5.2.

Table 5.1: Selection criteria for all $B^{\pm} \to D(\to 2\pi^{+}2\pi^{-})h^{\pm}$ candidates in the LHCb stripping.

Particle	Parameter	Selection Criteria
$\pi^{\pm}$	p	> 1000 MeV
	p_T	> 100 MeV
	$DLL_{K-\pi}$	< 20
	χ^2_{track}	< 4
	χ^2_{IP}	> 4
	p_{ghost}	< 0.4
D	p_T	> 1800 MeV
	m_D	[1764.84, 1964.84] MeV
	χ^2_{vtx}/N_{dof}	< 10
	$DIRA$	> 0
$h^{\pm}$	p	> 5000 MeV
	p_T	> 500 MeV
	χ^2_{track}	< 4
	χ^2_{IP}	> 4
	P_{ghost}	< 0.4
$B^{\pm}$	p_T	> 1000 MeV
	$m_{B^{\pm}}$	[4750, 7000] MeV
	$\tau_{B^{\pm}}$	> 0.2 ps
	χ^2_{IP}	< 25
	$DIRA$	> 0.999

B mesons have a lifetime of 1.6 ps, are created with high momentum and are highly likely to be produced in the forward region as explained in Section 3.2, thus they fly a number of millimetres downstream from their primary vertex before decaying and hence the $DIRA$ and χ^2_{FD} cuts are applied to the B meson. Consequently, not only is a secondary vertex detectable downstream but a large proportion of the $B^{\pm}$ mass is transferred into the kinetic energy of its daughters and is forward boosted. Therefore, the D meson also moves a brief distance downstream in its 410 fs lifetime before itself decaying, thus the χ^2_{FD} cut is applied to the D meson. Therefore, the D decay vertex ends up further downstream than the B decay vertex. As a result, the application of the FD_{sig_z} cut to the D meson can be used to reject charmless decays, where the final state particles originate from the B meson decay vertex (this is optimised further after the Gradient Boosted Decision tree stage).

However, even though the B meson and its daughters are predominantly forward boosted, the B meson daughters also have substantial p_T because the B mass is much larger than its daughters' mass. Hence, the p_T criteria on the D meson. Furthermore, the high p_T of the daughter particles and the B and D meson flight distances result in relatively large impact parameters with respect to the primary vertex for all the final state particles, whereas the B meson has a relatively small impact parameter since it originates from the primary vertex, thus the χ^2_{IP} cuts. A relatively tight D mass window is enforced to remove D mesons with mis-identified daughters such as $B^{\pm} \to D(\to K^{\pm}\pi^{\mp}\pi^{+}\pi^{-})h^{\pm}$ decays. The $ProbNN$ particle identification cuts on the D meson daughters reduce instances where they are misidentified. The $hasRICH$ cut on the bachelor particle makes sure there is information from the RICH to aid particle identification. Finally, the B mass window is wide enough to contain signal events, as well as enough of the partially reconstructed low mass backgrounds and combinatorial background in the upper mass region so that they can all be fitted in the global mass fit.

Table 5.2: Preselection criteria for all $B^{\pm} \to D(\to 2\pi^{+}2\pi^{-})h^{\pm}$ decays aimed at retaining as much signal as possible.

Particle	Parameter	Selection Criteria
$\pi^{\pm}$	$ProbNN_{\pi}$	> 0.02
	$ProbNN_{K}$	< 0.96
D	m_D	[1839.84, 1889.84] MeV
	χ^2_{IP}	> 1.5
	χ^2_{FD}	> 50
	FD_{sig_z}	> -4
$h^{\pm}$	χ^2_{IP}	> 5
	hasRich	True
$B^{\pm}$	χ^2_{IP}	< 20
	χ^2_{FD}	> 30
	$DIRA$	> 0.9995
	$m_{B^{\pm}}$	[5080, 5800] MeV

5.5.1 Truth Cuts

Truth cuts are used to truth match the simulated signal samples so that $B^{\pm}$ signal candidates are correctly reconstructed. The truth cuts in this analysis are shown in Table 5.3.

The particle IDs correspond to the respective particle PDG ID code [77] or ID number 0 (when the particle is not recognised by any PDG ID code) called a ghost track which needs to be

Table 5.3: Truth selection criteria for all simulated signal samples.

Particle	Parameter	Selection Criteria
Daughter $\pi^{\pm}$	particle TRUE ID	$\pm$211 or 0
	mother particle ID	$\pm$421 or 0
D	particle TRUE ID	$\pm$421 or 0
	mother particle ID	$\pm$521 or 0
Bachelor $K^{\pm}$	particle TRUE ID	$\pm$321 or 0
	mother particle ID	$\pm$521 or 0
Bachelor $\pi^{\pm}$	particle TRUE ID	$\pm$211 or 0
	mother particle ID	$\pm$521 or 0
$B^{\pm}$	particle TRUE ID	$\pm$521 or 0
	Background Category	0 or 50 or 60

included as explained below. Moreover, it is a requirement that the background category [78] of the B meson must either be:

- 0 which are true signal candidates.
- 50 which are events where all particles are correctly identified and originate from the same MC particle but at least one particle has been omitted . Figure 5.1 shows that a large proportion of these decays are very near to the B mass peak, hence they are real signal decays which have undergone final state radiation and a photon is missing.
- 60 which are events where a minimum of one particle is classed as a ghost track which could be a poorly reconstructed signal track or one which decayed in flight. As a result, an obvious signal peak can be observed in Figure 5.1.

Figures 5.1 and 5.2 demonstrates that it is important to include B mass background categories 50 and 60 (and particle ID 0) to ensure the particular signal shape parameters which are fixed in the global invariant fit in Section 6.1 are accurate because the categories in question affect the tails of the B mass distribution.

5.6 Gradient Boosted Decision Tree Classifier

A multivariate analysis technique known as a Gradient Boosted Decision Tree classifier, from the Toolkit for MultiVariate data Analysis (TMVA) with ROOT package [79], is used to classify signal from background derived from false combinations of tracks in the detector known as combinatorial background.

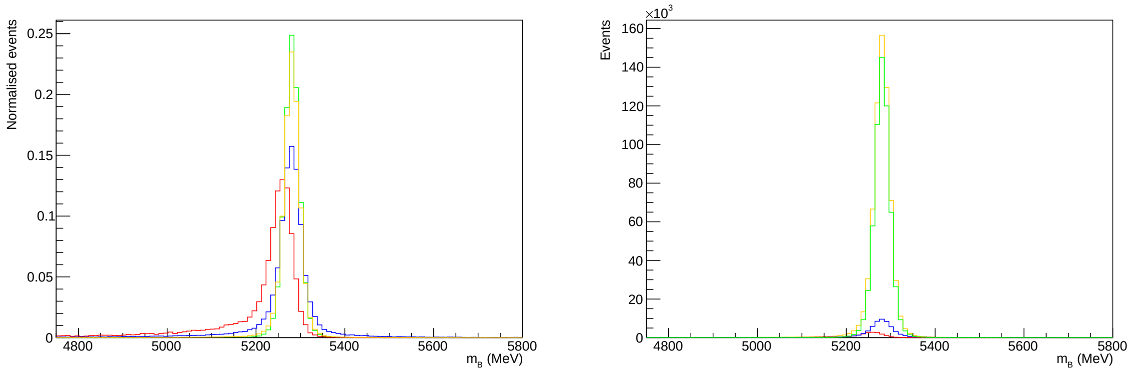

FIGURE 5.1. $B^{\pm} \to DK^{\pm}$ signal simulation sample after truth cuts and preselections (normalised left, unnormalised right), Background category 0 green, 50 red, 60 blue, combined 0, 50 and 60 orange .

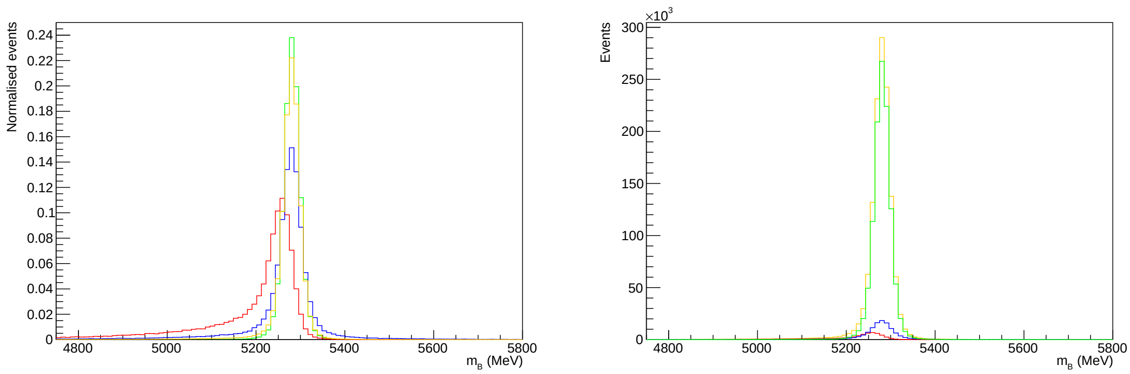

FIGURE 5.2. $B^{\pm} \to D\pi^{\pm}$ signal simulation sample after truth cuts and preselections (normalised left, unnormalised right), Background category 0 green, 50 red, 60 blue, combined 0, 50 and 60 orange .

5.6.1 Simple Decision Tree

In order to classify events in a sample as signal or background using a decision tree, it first has to be trained using a training sample where all the events are labelled as either signal or background. This is known as a supervised machine learning technique. A simple decision tree is made up of successive nodes beginning with the root node. Initially, a condition to split the events in the full training sample at the root node is determined, consisting of a cut value on a particular variable for example cut c1 on variable xi as shown in Figure 5.3 resulting in two subsequent sets of events at the daughter nodes. The cut variable and value is chosen such that it provides the best separation between signal and background using a separation index. In this case, the optimal separation is established using the Gini Index defined as $p(1-p)$, where $p = s/(s+b)$ is the signal purity derived from number of signal events s and number of background events b, thus, the Gini Index can be written as $sb/(s+b)^2$. The maximum value of the Gini Index = 0.25 is when purity is equal to 0.5 in an equally mixed sample of signal and background and, the minimum of the Gini Index = 0 when purity is either equal to 1 or 0 and, the sample is either entirely signal or background respectively. The optimal value of the Gini Index is the value which provides the greatest difference between the Gini Index of the parent node and the weighted sum of its daughters nodes (weighted by the number of events at each node). This process is repeated at all the subsequent nodes until either, the separation index of the node cannot be improved further, the maximum depth of the decision tree is at capacity or the specified minimum number events in a node cannot be reached (5% of the total training events). When the training is complete the leaf nodes at the end of each branch path within the tree are classified as either signal or background based on whichever class is in the majority. The decision tree has effectively split the phase space into n number of hyper cubes where n is the number of leaf nodes at the end of branches within the tree. Once a decision tree is trained, unlabelled data can be used an an input into the decision tree and each event will be classified as either signal or background.

5.6.2 Boosted Decision Tree

However, simple decision trees suffer some potential drawbacks such as overfitting to the training data sample, particularly when grown to large depth size, and being susceptible to statistical fluctuations causing the tree to take paths which would not have been optimal otherwise. As a result, this can lead to poor generalisation of performance of the tree. A solution to these issues is to instead create an ensemble of multiple weakly classifying trees with limited depth using boosting known as a Boosted Decision Tree (BDT). Boosting uses the outcome of a decision tree to inform the creation of successive decision trees during training through an iterative process. In each iteration the incorrectly classified training events in a decision tree are all given a higher common weight in the training sample used to train the next decision

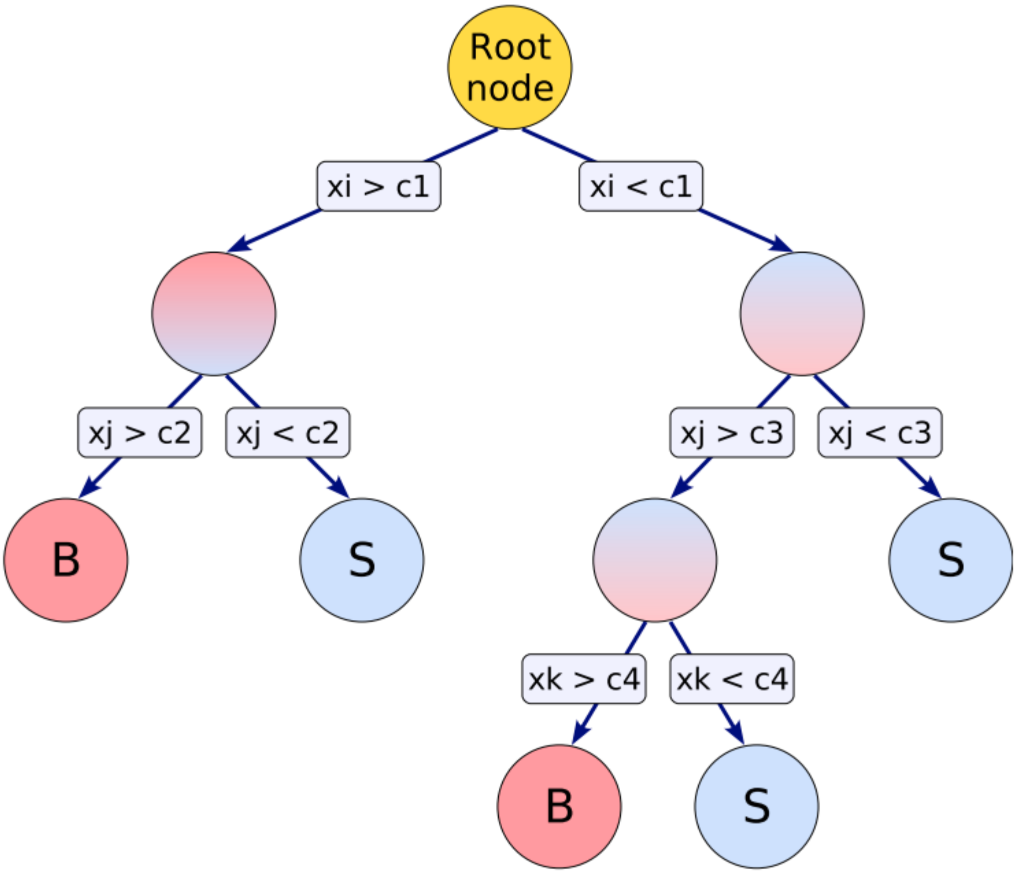

FIGURE 5.3. Example of simple decision tree. Figure is from Reference [79].

tree. Initially the training event weights are all equal to a constant. In each successive i-th tree the incorrectly classified training events weights are then updated by multiplying them by a common boost weight α defined as

$$\alpha_i = \frac{1 - err_{i-1}}{err_{i-1}}, \tag{5.4}$$

where err_{i-1} is the previous tree's weighted misclassification rate (and must satisfy $err_{i-1} \leq 0.5$). Each decision tree attempts to minimise the weighted misclassification rate err_i. Afterwards the whole sample's weights are renormalised to ensure the sum of the weights is constant. As a consequence, subsequent trees are optimised to correctly classify those events the previous trees misclassified.

After a Boosted Decision Tree is fully trained, its response $F(\hat{x})$ (the boosted event classification) for an event m with variables $\hat{x}$ is a weighted average of the output of N simple decision trees defined as:

$$F(\hat{x}) = \frac{1}{\sum_{i=0}^{N} \ln(\alpha_i)} \sum_{i=0}^{N} \ln(\alpha_i) f_i(\hat{x}) \tag{5.5}$$

Each simple decision tree classifies an event (with associated variables $\hat{x}$) as either signal where the output $f(\hat{x})$ = 1 or background with output $f(\hat{x})$ = -1. As a result, the boosted event classification $F(\hat{x})$ is a value between -1 and +1 where the event is more background-like the closer it is to the former limit and the more signal-like the nearer it is the latter limit.

5.6.3 Gradient Boost

In this analysis the GradientBoost method is used. The GradientBoost method differs from the traditional BDT as it utilises a loss-function $L(F,y)$ which measures the difference between the prediction of the BDT response $F(\hat{x})$ and the true label $y(\hat{x})$ of an event. Thus, each event is given an individual event weight corresponding to its loss function. A Gradient Boosted Decision Tree is advantageous as it performs well on noisy data with outliers and/or mislabelled data points and on samples where background events are difficult to distinguish from signal events [79]. This is achieved by using a smooth loss-function (Equation 5.6) that does not over-penalise misclassified events. Moreover, this has the added benefit of being robust to overtraining.

The loss-function for the Gradient Boost Decision Tree is the binomial log-likelihood:

$$L(F,y) = \ln(1 + \exp^{-2F(\hat{x})y}). \tag{5.6}$$

The average loss of the each decision tree over the entire training sample with k events is determined using:

$$\langle L(F,y)\rangle^i = \sum_{l=0}^{k} \omega_l^i L_l^i. \tag{5.7}$$

The average loss is analogous to the misclassification rate err. This allows each tree's boosting coefficient to be calculated:

$$\alpha_i = \frac{\langle L(F,y)\rangle^i}{1 - \langle L(F,y)\rangle^i} \tag{5.8}$$

The individual boosting weight of each each event k in each tree i can the obtained:

$$\omega_k^i = \omega_k^{i-1} \cdot \alpha_i^{1-L_k^{(i-1)}} \tag{5.9}$$

The loss-function $L^i(F(\hat{x}), y)$ is minimised for each decision tree in order to optimise the full BDT.

5.6.4 BDT Strategy

The BDT requires training samples for the background and signal. Ordinarily any samples used to train the BDT cannot be used later in the analysis as the selection would be biased. However, this issue can be addressed by instead training and testing two BDTs- BDT0 and BDT1- on sub samples of 2 different samples- sample A and sample B- and then applying the BDT trained and tested on one sample to the alternative sample and vice versa. The training samples used in this analysis are large enough to cope with statistical fluctuations. Other than being trained on different samples the two BDTs have identical properties.

The two samples, sample A and sample B are each split into two further samples A1 and A2 and B1 and B2, where A1 and B1 are used for training BDT0 and BDT1 respectively and A2 and B2 are used to test BDT0 and BDT1 respectively, as can be seen in Figure 5.4. Thus, the fully trained and tested BDT0 and BDT1 can be applied to sample B and sample A, respectively as illustated in Figure 5.5.

The full signal $B^{\pm} \rightarrow D(\rightarrow 2\pi^{+}2\pi^{-})K^{\pm}$ simulation samples after the preselection step are used as the signal samples for training the BDT. Data from the $B^{\pm} \rightarrow D(\rightarrow 2\pi^{+}2\pi^{-})K^{\pm}$ upper B mass sideband above 5800MeV after the preselection stage is used as the background samples for training the BDT, as these events are likely to be entirely combinatorial background. Both signal simulation samples and background data samples are used following the procedure as outlined above, for example there is "signal sample A" and "background sample A." Events not used in training and testing the BDT are randomly assigned to sample A and Sample B in equal numbers after the training and testing step but before the application of the BDT.

5.6.5 Input Variables

The input variables for the BDTs need to have varying distributions for signal and background events so they have power to distinguish between them. To keep the efficiencies similar between $B^{\pm} \rightarrow DK^{\pm}$ and the $B^{\pm} \rightarrow D\pi^{\pm}$ decay modes, no particle identification variables on the bachelor kaon or bachelor pion are included.

As a result, due to the signal decay's topology as previously discussed in Section 5.5, input variables for the BDTs include $\log(p_T)$, $\log(p)$ and $\log(\chi^2_{IP})$ for all particles, $\log(\chi^2_{FD})$, $\log(\chi^2_{vtx})$, Δ_{vtx}, $sign\Delta_{vtx}FD$ and and $\log(1-DIRA)$ for the B and D mesons as well as $\log(\chi^2)$ for the B and finally I_{PT}. All the input variables for the BDTs are ranked in order of importance in Tables

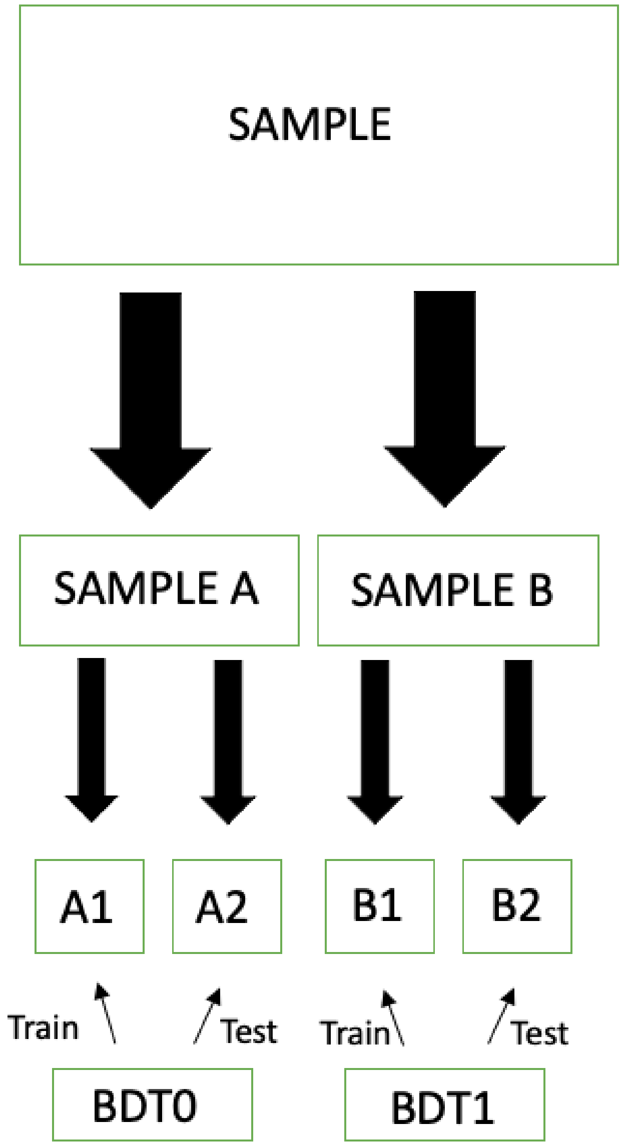

FIGURE 5.4. BDT Train and Test Strategy.

5.4 and 5.5, where the higher the frequency with which the variable is chosen by the decision tree the more important it is. Differences in the background and signal distributions of the input variables for BDT0 can be observed in Figures 5.6 and 5.7 and for BDT1 seen in Figures 5.8 and 5.9, the double-peak structure on the red curve in some of the sub-figures is due to prompt D decays (the left hand peak) and secondary D decays (the right hand peak).

Initially, the DecayTreeFitter χ^2 seemed to be a very effective BDT input variable for discriminating signal from background and suppressed the sidebands significantly. However,

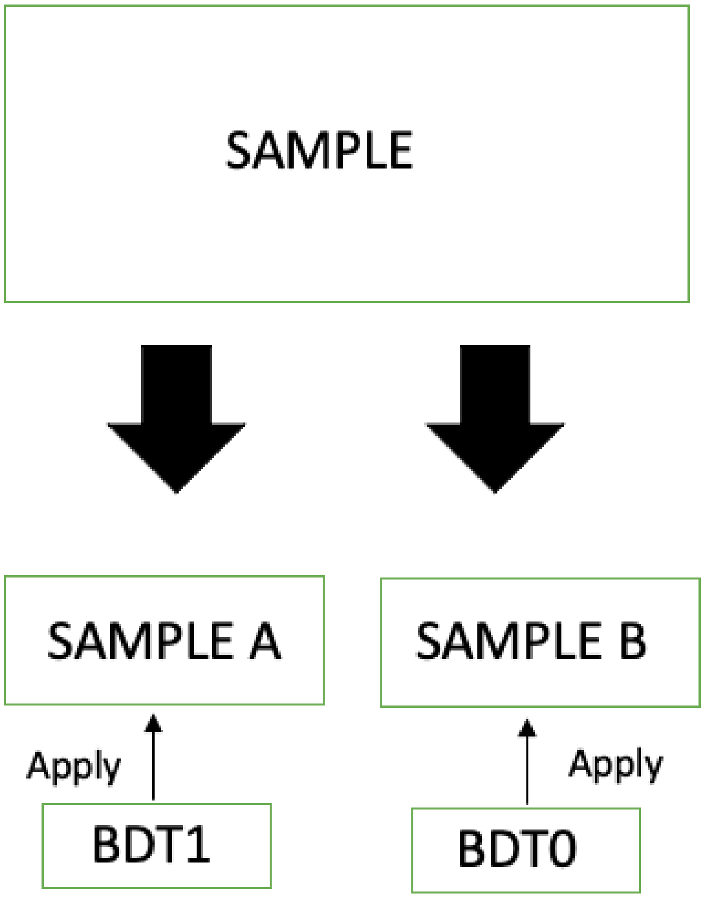

FIGURE 5.5. BDT Application Strategy

it was found that it was not uniformly effecting the charmless background but instead sculpted the sidebands. Almost all the charmless background from the upper sideband was removed, whilst Charmless background remained beneath the signal peak. The Charmless background under the signal peak is modelled from the D mass upper sideband as explained in 5.8.1, hence the decision was taken to exclude the DecayTreeFitter χ^2 as an input variable for the BDT.

5.6.6 BDT Training results

As previously explained each event has a BDT response value between -1 and +1, where -1 indicates an event is background and +1 indicates the event is signal. Figures 5.10 and 5.11 show the BDT responses for the signal and background training and testing samples, which have peaks at +1 and -1 respectively. Furthermore, Figures 5.10 and 5.11 show there is no evidence of overtraining since there is a consistency between the BDT results on both the training and testing samples for BDT0 and BDT1 respectively, and that both BDTs are highly effective at separating signal from background events. Moreover the difference in TMVA

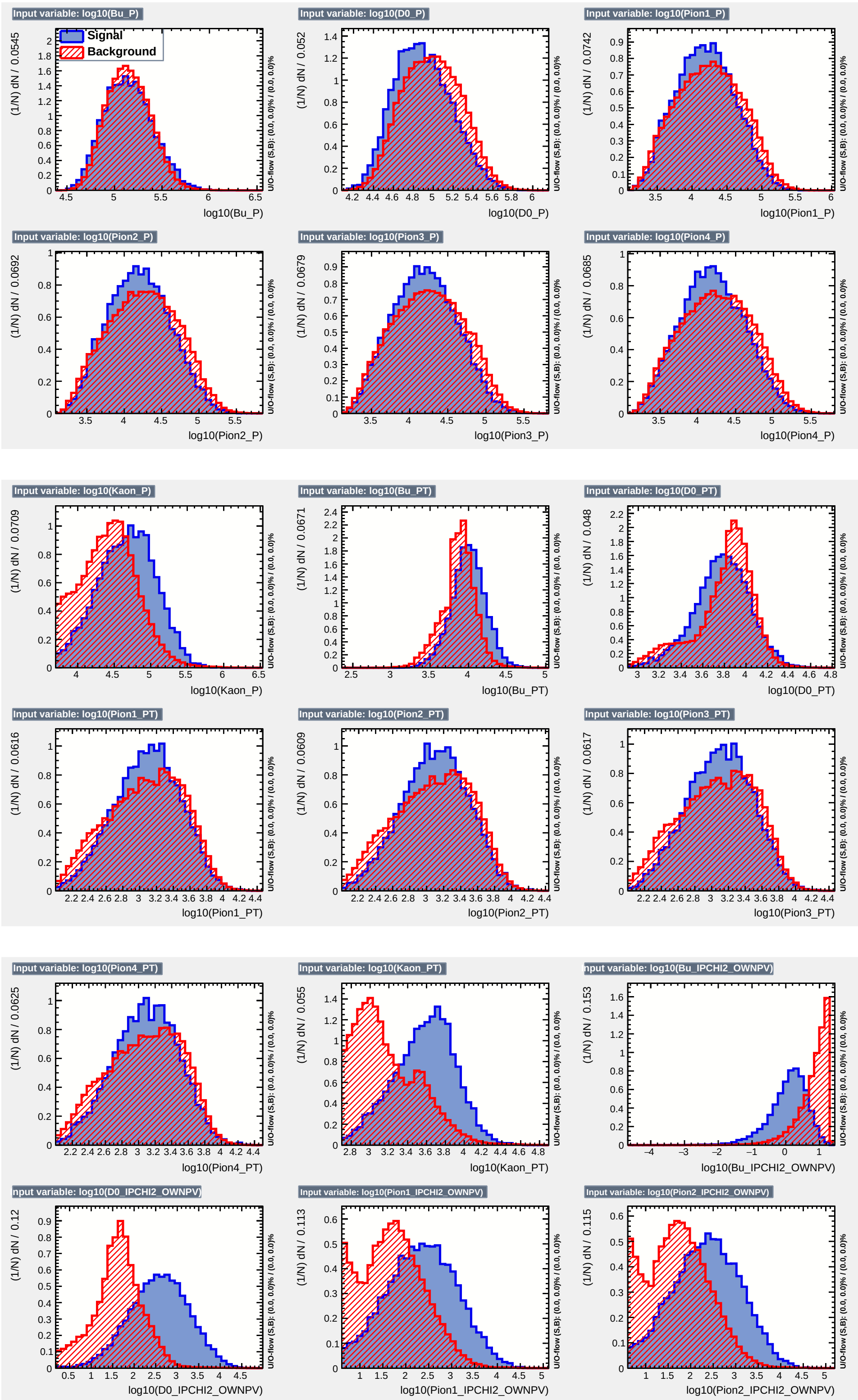

Figure 5.6: BDT0 training signal (blue) and background (red) input parameter distributions.

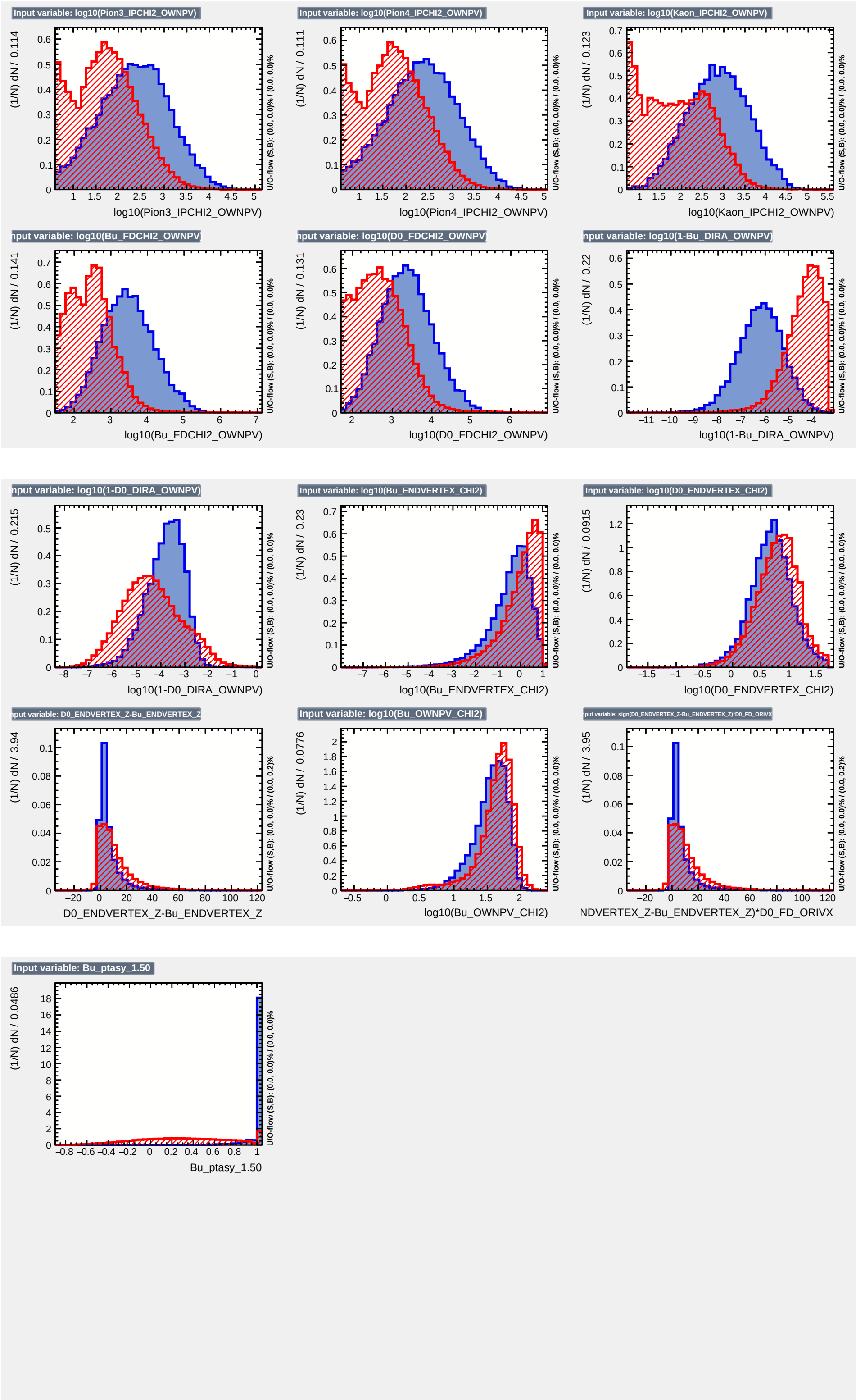

Figure 5.7: BDT0 training signal (blue) and background (red) input parameter distributions.

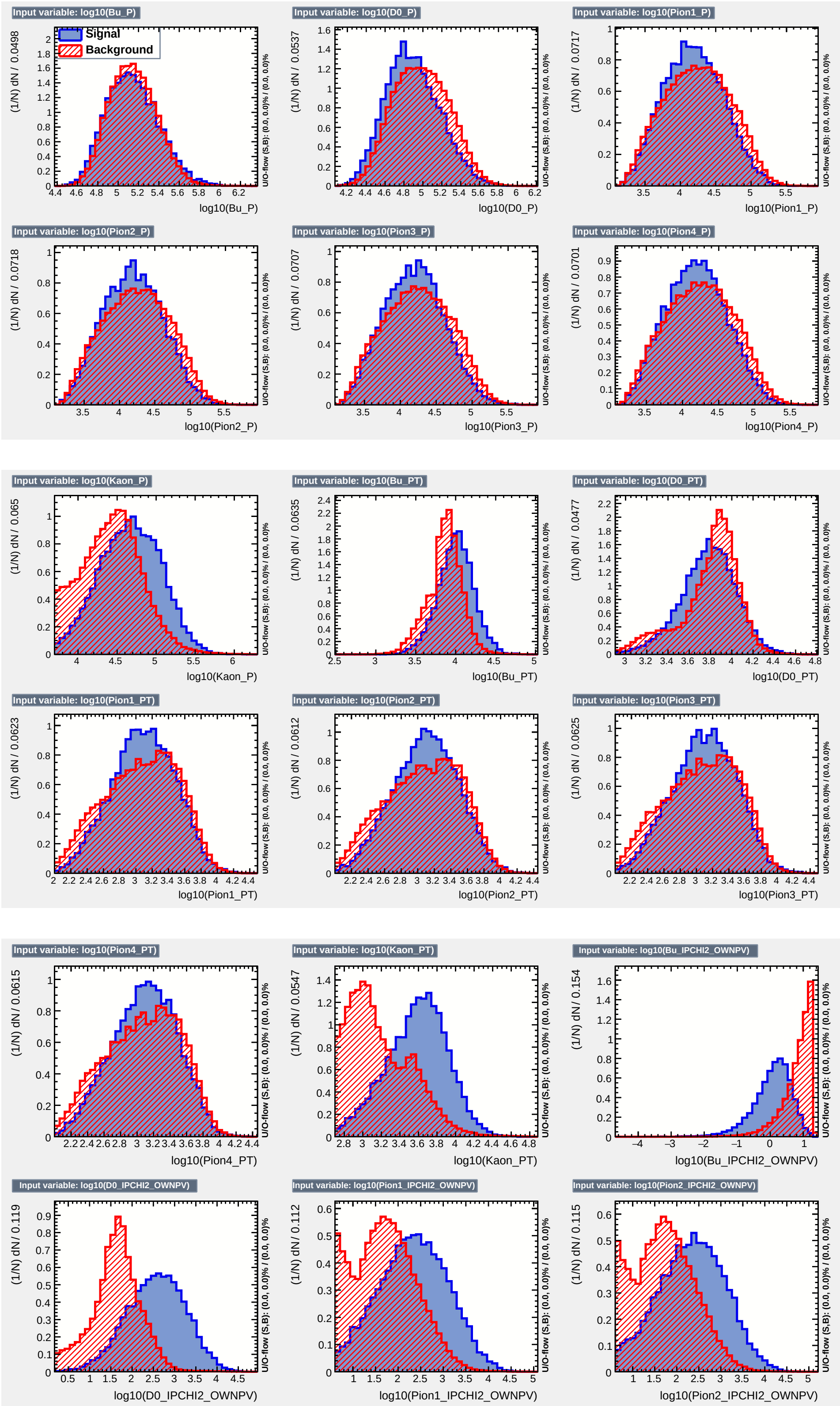

Figure 5.8: BDT1 training signal (blue) and background (red) input parameter distributions.

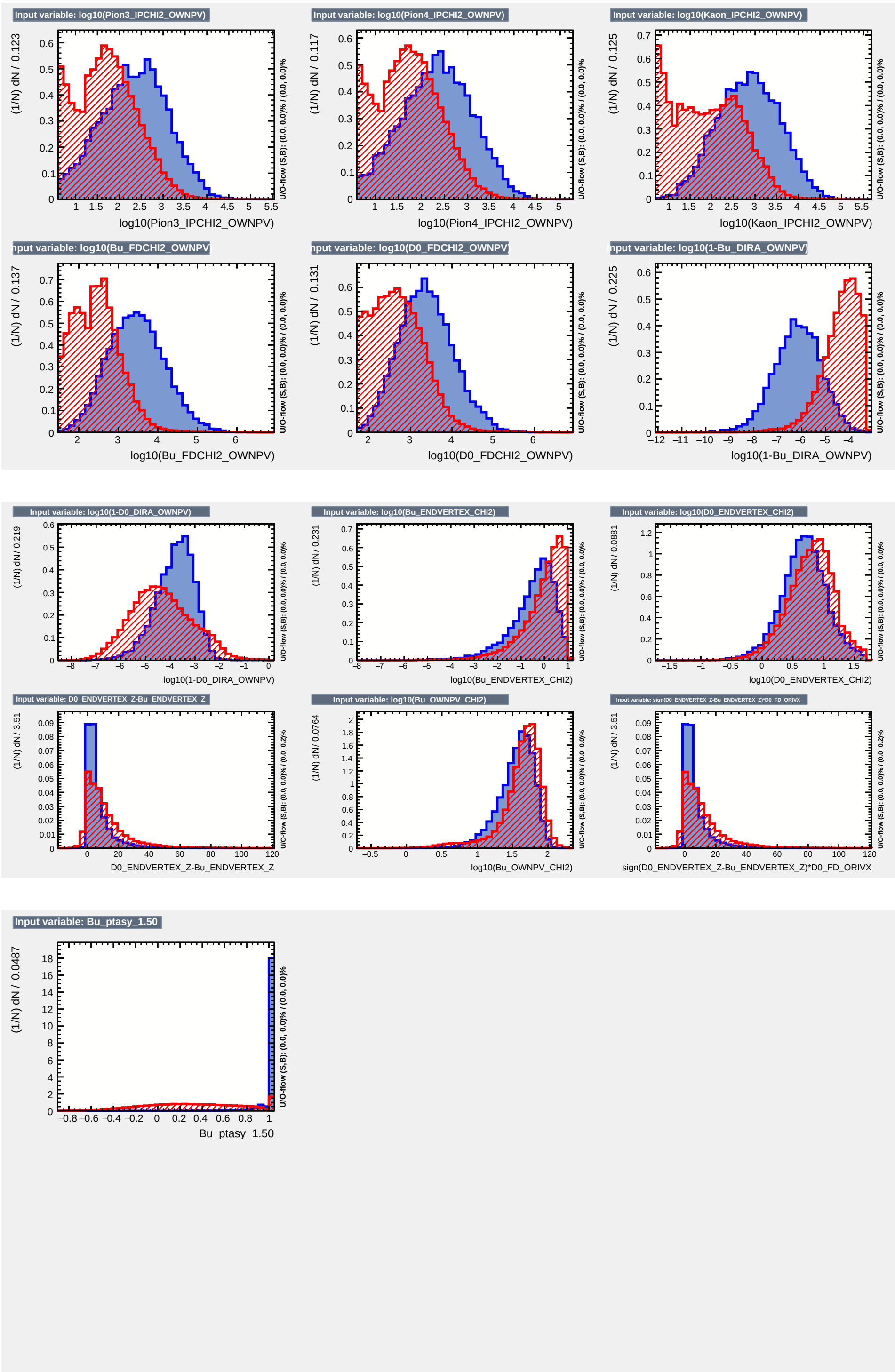

Figure 5.9: BDT1 training signal (blue) and background (red) input parameter distributions.

Table 5.4: Ranking of input variables for BDT0 after training .

Particle	Parameter	Ranking	Importance(%)
$B^{\pm}$	I_{PT}	1	5.14
$h^{\pm}$	$\log(p)$	2	4.50
D	$\log(\chi^2_{IP})$	3	4.27
π_2	$\log(p)$	4	4.24
$h^{\pm}$	$\log(p_T)$	5	4.04
$B^{\pm}$	$\log(p_T)$	6	3.81
$B^{\pm}$	$\log(p)$	7	3.73
$B^{\pm}$	$\log(1-DIRA)$	8	3.71
D	$\log(\chi^2)$	9	3.70
D	$\log(p_T)$	10	3.69
π_4	$\log(\chi^2_{IP})$	11	3.58
π_3	$\log(\chi^2_{IP})$	12	3.34
π_1	$\log(\chi^2_{IP})$	13	3.31
D	$\log(1-DIRA)$	14	3.23
π_1	$\log(p)$	15	3.18
π_1	$\log(p_T)$	16	3.14
$B^{\pm}$	$\log(\chi^2_{IP})$	17	3.00
$h^{\pm}$	$\log(\chi^2_{IP})$	18	2.99
π_3	$\log(p_T)$	19	2.98
π_2	$\log(p_T)$	20	2.84
$B^{\pm}$	$\log(\chi^2_{FD})$	21	2.84
π_4	$\log(p_T)$	22	2.80
D	$\log(p)$	23	2.74
π_3	$\log(p)$	24	2.70
π_2	$\log(\chi^2_{IP})$	25	2.65
π_4	$\log(p)$	26	2.61
$B^{\pm}$	$\log(\chi^2)$	27	2.58
$B^{\pm}$	$\log(\chi^2)$	28	2.53
D	$\log(\chi^2_{FD})$	29	2.28
D	Δ_{vtx}	30	1.90
D	$sign\Delta_{vtx}FD$	31	1.89

overtraining scores for the Receiving Operating Characteristic (ROC) curves between the test and train samples are 0.4% for BDT0 and 0.5% for BDT1 for a background rejection value of 99% and non-existent for background rejection scores of 90% and 70% further demonstrating the BDTs are not overtrained.

When the trained and tested BDTs are applied to the candidates in the full data sample they receive a BDT response value, hence a BDT response cut value is chosen for the BDTs and events which do not meet the cut criteria are removed from the sample. The optimal BDT cut

Table 5.5: Ranking of input variables for BDT1 after training .

Particle	Parameter	Ranking	Importance(%)
$B^{\pm}$	I_{PT}	1	5.17
D	$\log(\chi^2_{IP})$	2	4.38
$B^{\pm}$	$\log(1-DIRA)$	3	4.23
$h^{\pm}$	$\log(p)$	4	4.04
$B^{\pm}$	$\log(p_T)$	5	3.96
$h^{\pm}$	$\log(p_T)$	6	3.94
$B^{\pm}$	$\log(p)$	7	3.79
D	$\log(p_T)$	8	3.76
π_3	$\log(\chi^2_{IP})$	9	3.46
D	$\log(1-DIRA)$	10	3.43
D	$\log(\chi^2)$	11	3.40
$B^{\pm}$	$\log(\chi^2_{IP})$	12	3.39
π_4	$\log(p_T)$	13	3.24
π_2	$\log(p)$	14	3.20
π_3	$\log(p_T)$	15	3.13
π_4	$\log(p)$	16	3.08
π_2	$\log(\chi^2_{IP})$	17	3.06
π_4	$\log(\chi^2_{IP})$	18	3.06
π_1	$\log(\chi^2_{IP})$	19	3.05
π_1	$\log(p_T)$	20	2.97
π_2	$\log(p_T)$	21	2.95
D	$\log(p)$	22	2.95
$h^{\pm}$	$\log(\chi^2_{IP})$	23	2.84
π_3	$\log(p)$	24	2.78
π_1	$\log(p)$	25	2.78
$B^{\pm}$	$\log(\chi^2_{FD})$	26	2.72
$B^{\pm}$	$\log(\chi^2)$	27	2.62
D	$\log(\chi^2_{FD})$	28	2.63
$B^{\pm}$	$\log(\chi^2)$	29	2.43
D	$sign\Delta_{vtx}FD$	30	1.83
D	Δ_{vtx}	31	1.76

value is chosen using figures of merit in Section 5.9 in order to maximise the proportion of signal events in the DK mode signal region.

5.7 Particle Identification Cuts

The particle identification (PID) cuts on the bachelor particles are applied directly to the data samples but not the simulation samples as the PID distributions are not well modelled in simulation. Therefore, the PIDCalib2 package [80] [81] [82] is used to obtain and apply the PID

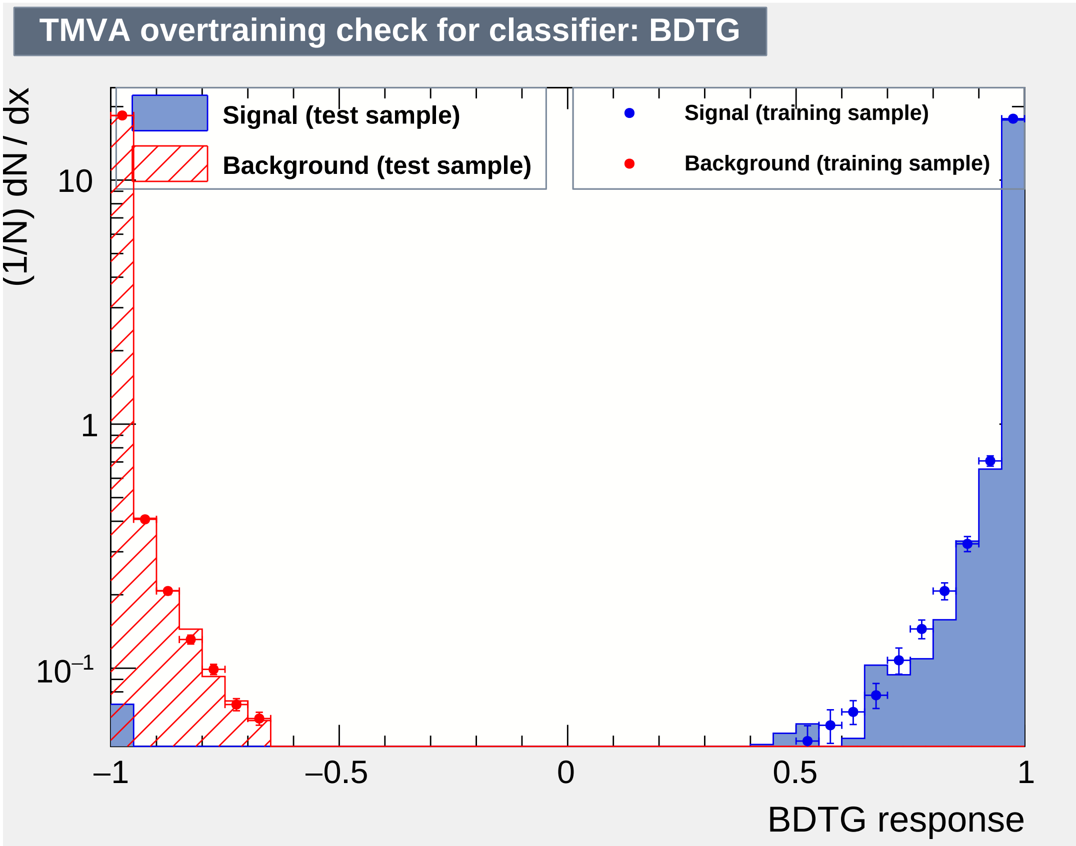

FIGURE 5.10. Response of the BDT for signal and background sample used to train and test the BDT0. The y axis scale is logarithmic. The TMVA overtraining check for the associated ROC curves result in signal efficiency values of 96.8%, 100%, 100% for the test sample and 97.6%, 100% and 100% for the train sample for the background rejection values of 99%, 90% and 70% respectively.

cuts to the bachelor particles in the simulation samples. PIDCalib2 provides data-driven PID performance data (mis-ID rate, efficiency, etc) as a function of particle kinematics and global event properties such as the number of charged particles in the event. It is based on calibration data using decays where the true particle ID is known - such as $D^{*+} \to D^0\pi^+$, where the D^0 (nearly) always decays to $K^-\pi^+$. PIDCalib2 has calibration data samples for each magnet polarity, for every data taking year, and uses the associated calibration sample along with the bachelor PID requirements (including the binning variables and the PID cuts) of the analysis to create PID efficiency histograms, which can be applied to the simulation sample to estimate the average PID efficiency of a sample and provide an efficiency weight for each event in the sample. The default binning schemes for the parameters used by PIDCalib2 are:

- The momentum p: 3 bins separated at 3, 9.3 and 15.6 GeV and then 15 uniformly spread bins in the 15.6 to 100 GeV range;

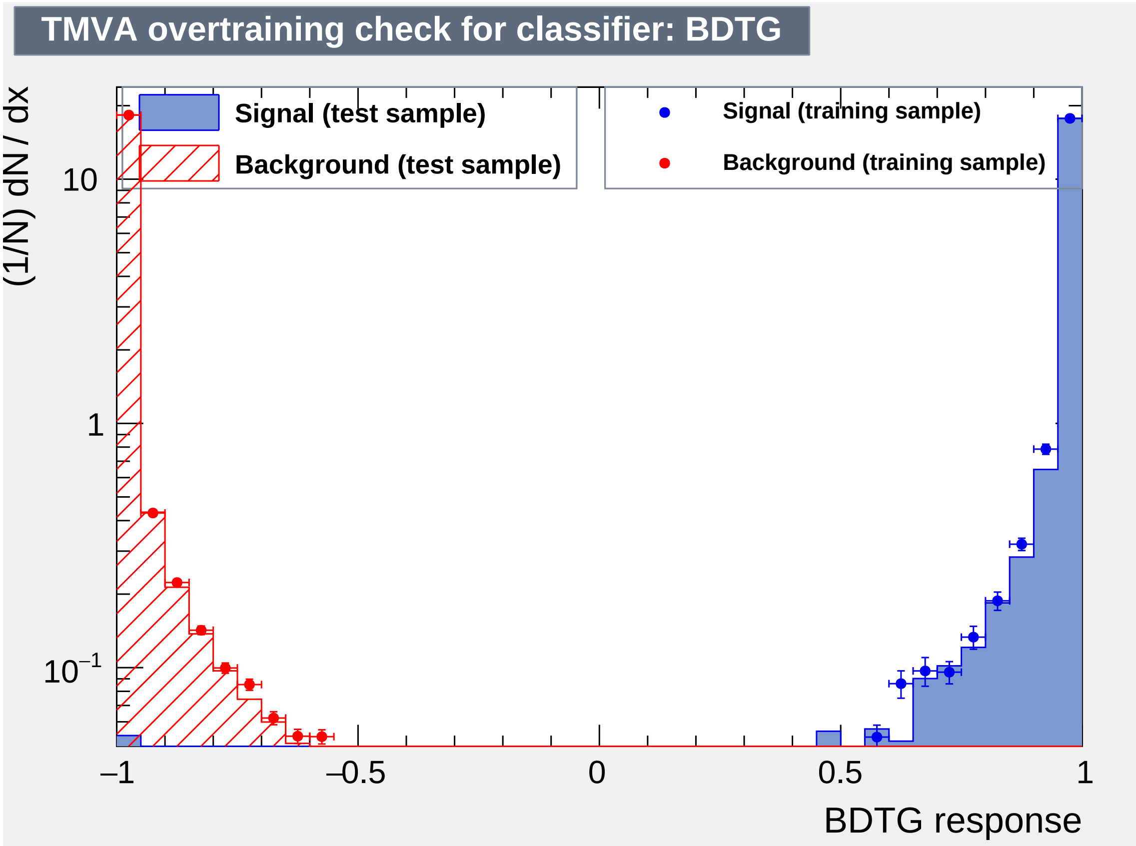

FIGURE 5.11. Response of the BDT for signal and background sample used to train and test the BDT1. The y axis scale is logarithmic. The TMVA overtraining check for the associated ROC curves result in signal efficiency values of 97.1%, 100%, 100% for the test sample and 97.6%, 100% and 100% for the train sample for the background rejection values of 99%, 90% and 70% respectively.

- The pseudorapidity η: 4 uniformly spread bins in range 1.5 to 5.
- The number of charged tracks $nTracks$: 4 bins separated at 0, 50, 200, 300 and 500.

Cuts to all the samples are applied to match the upper and lower bounds of the PID binning schemes to ensure optimal particle identification performance.

The PID efficiency weights for each event in a sample are required to reweight the simulation samples so that some or all of their shape parameters can be obtained for use in the global invariant mass fit in Chapter 6. Therefore, PIDCalib2 is used for all signal, cross-feed and partially reconstructed background simulation samples to obtain these weights.

The PID efficiency weights are also needed for the efficiency calculation (see Section 5.10). The average PID efficiency value for each signal $\epsilon^{PID}_{\pi\to\pi}$, $\epsilon^{PID}_{K\to K}$ and misidentified bachelor $\epsilon^{PID}_{\pi\to K}$,

$\epsilon^{PID}_{K\rightarrow\pi}$ simulation sample used in the efficiency calculations are defined as:

- $\epsilon^{PID}_{\pi\rightarrow\pi}$- The fraction of events where an actual pion is correctly identified when the PID cut is applied.
- $\epsilon^{PID}_{\pi\rightarrow K}$ - The fraction of events where an actual pion is misidentified as a kaon when the PID cut is applied.
- $\epsilon^{PID}_{K\rightarrow K}$ - The fraction of events where an actual kaon is correctly identified when the PID cut is applied.
- $\epsilon^{PID}_{K\rightarrow\pi}$ - The fraction of events where an actual kaon is misidentified as a pion when the PID cut is applied.

The kinematic distributions of the signal $B\rightarrow D\pi$ sample, signal $B\rightarrow DK$ sample and the cross-feed sample in the DK mode are similar as illustrated in Figure 5.7. Therefore, the $B\rightarrow D\pi$ sample is the simulation sample used to obtain the average PID efficiencies $\epsilon^{PID}_{\pi\rightarrow\pi}$, $\epsilon^{PID}_{K\rightarrow K}$ and $\epsilon^{PID}_{\pi\rightarrow K}$, since the $B\rightarrow D\pi$ sample has the highest statistics. The simulation sample where the bachelor kaon is reconstructed as a pion is used to establish $\epsilon^{PID}_{K\rightarrow\pi}$ as its kinematics vary compared to the other samples as shown is Figure 5.7.

The optimal PID cut values are chosen using figures of merit in Section 5.9.

5.8 Backgrounds

There are a number of backgrounds that have the potential to impact on the signal region. This section discusses these backgrounds and how they are addressed. However, this does not include partially reconstructed or combinatorial backgrounds which cannot be eliminated or reduced effectively with additional selections and need to be modelled in the fit to determine their impact on the signal region as outlined in Chapter 6.

5.8.1 Charmless Background

Charmless backgrounds occur when a B meson decays to the same final state particles as the signal decay but decays to them directly rather than via the D meson. As a result, $B\rightarrow 4\pi K$ decays in the DK mode and $B\rightarrow 5\pi$ decays in the $D\pi$ channel need to be investigated as they are located under the B mass signal peaks in the data sample and affect the proportion of DK and $D\pi$ signal events in the signal region. The charmless backgrounds have different CP violation to the signal decays and therefore need to be removed or reduced and modelled.

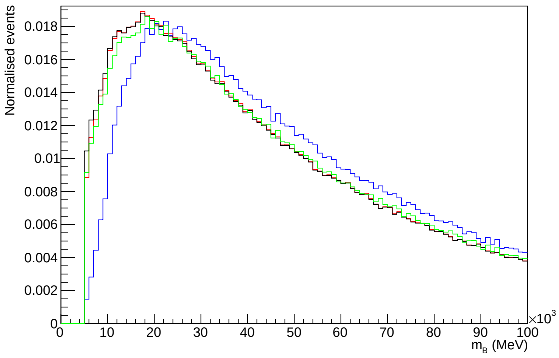

(a) p distribution.

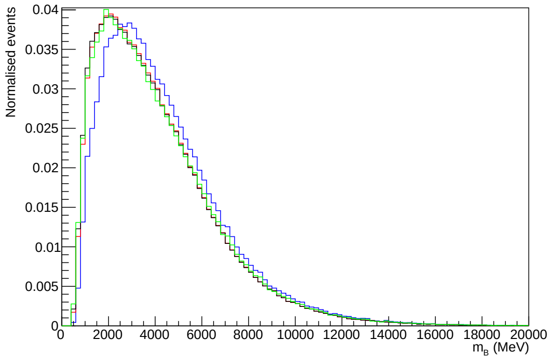

(b) p_T distribution

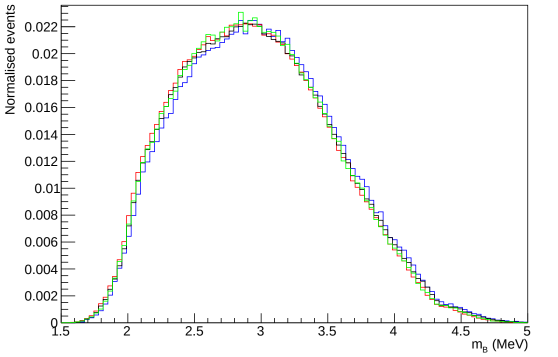

(c) η distribution.

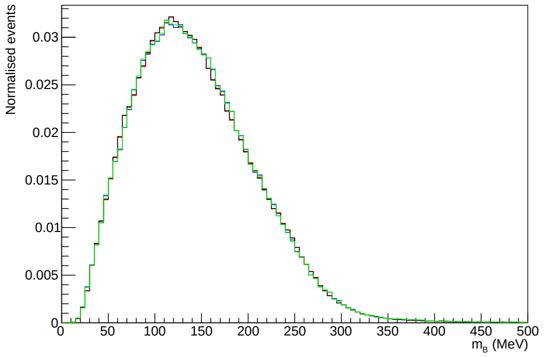

(d) $nTracks$ distribution.

Figure 5.12: The p, p_T, η and $nTrack$ variable distributions for the simulation sample distributions $B^{\pm} \to DK^{\pm}$ (green), $B^{\pm} \to D\pi^{\pm}$ (black), $B^{\pm} \to DK^{\pm}$ reconstructed as $B^{\pm} \to D\pi^{\pm}$ (blue), $B^{\pm} \to D\pi^{\pm}$ reconstructed as $B^{\pm} \to DK^{\pm}$ (red).

As mentioned in Section 5.5, the FD_{sig_z} cut is very effective at distinguishing signal from charmless background, as signal decays should have a distance between the B decay vertex and D decay vertex whereas, for charmless decays the B decay vertex and "D" decay vertex are the same since the B decays directly to the four daughter pions. The charmless shape and yield in each signal mode can be estimated with a fit to the upper D mass sideband between 1920 and 1970MeV/c^2 of the data in each channel as explained in Section 6.4. The upper D mass sideband is used rather than the low D mass sideband due to contamination in the lower D mass sideband.

It is found that the FD_{sig_z} cut on the D meson is highly effective at suppressing charmless background in both the DK and $D\pi$ modes. However, the optimal FD_{sig_z} is determined from figures of merit in Section 5.9 since the aim is to optimise the proportion of $B \to DK$ signal events in the DK signal region, which does not necessarily correspond with eliminating all the charmless background. Thus, the FD_{sig_z} cuts > 0, > 2 and > 4 are applied during the simultaneous optimisation of multiple cuts. Although the charmless background in the $D\pi$ mode remains negligible for all FD_{sig_z} cuts, the charmless in the DK mode does not remain negligible and needs to be modelled in these cases as Table 5.6 shows.

Table 5.6: An example of charmless yields in the $B^{\pm} \to DK^{\pm}$ mode for varying FD_{sig_z} cuts when all other cuts (apart from the D mass window) in Tables 5.1, 5.2, 5.3 and 5.7 are applied.

FD_{sig_z} Cut	$B^{\pm} \to DK^{\pm}$ mode
> 0 Cut	890.89
> 2 Cut	204.76
> 4 Cut	48.472

5.8.2 The $B^{\pm} \to D^0(\to K^0_s\pi^+\pi^-)h^{\pm}$ Background

$B^{\pm} \to D^0(\to K^0_s\pi^+\pi^-)h^{\pm}$ is an important background in the data sample because the branching ratio of $D^0 \to K^0_s\pi^+\pi^-$ is four times larger than $D^0 \to 2\pi^+2\pi^-$, and it ultimately decays into the same $2\pi^+2\pi^-$ final state. The K^0_s decays have a short flight distance which means that $D^0 \to K^0_s\pi^+\pi^-$ is very similar to $D^0 \to 2\pi^+2\pi^-$ but the phase space distribution is different, and thus $D^0 \to K^0_s\pi^+\pi^-$ decays need to be removed.

To ensure the $D^0 \to K^0_s\pi^+\pi^-$ background is negligible, a rectangular veto selection $480 MeV/c < m(\pi^+\pi^-) < 505\ MeV/c$ is applied to the invariant mass of each pair of opposite sign pions $m(\pi^+\pi^-)$, such that the region surrounding the K^0_S mass is excluded. The selection applied is in line with the selection used in the measurement of the $D^0 \to 2\pi^+2\pi-$ hadronic parameters from Reference [36], thus ensuring that the results obtained in Reference [36] can be used as input for this analysis.

5.8.3 Semi Leptonic Background

Similarly to Reference [83] and Reference [29] the background from $B^{\pm} \to D\mu^{\pm}\nu_{\mu}$, where $\mu^{\pm}$ is misidentified as the bachelor, is vetoed using the cut $ISmuon == 0$ on the bachelor candidate. This is applied as it is clear in the $B^{\pm} \to D\pi^{\pm}$ data that semi-leptonic background is present, as shown in Figure 5.13. Punch-through and in-flight decay pions account for the reduced green signal peak but the green shape also varies from the red shape in the lower mass regions too. The greater green background in the low mass region is different in shape from the partially reconstructed background and indicates the presence of semi-leptonic background.

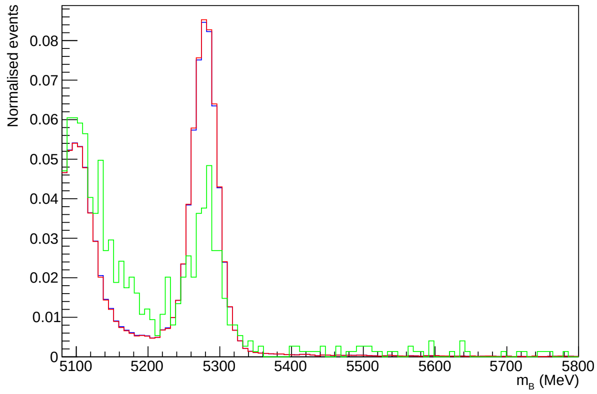

FIGURE 5.13. The $B^{\pm} \to D\pi^{\pm}$ mass distribution where no muon cut is applied (blue), $ISmuon == 0$ veto applied (red) and $ISmuon == 1$ cut applied (green).

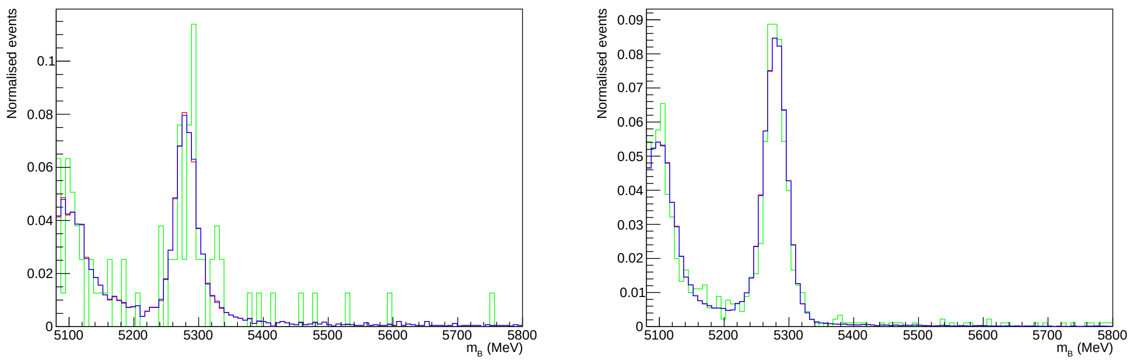

Figure 5.14: The $B^{\pm} \to DK^{\pm}$ mass distribution (left) and $B^{\pm} \to D\pi^{\pm}$ mass distribution (right) where no electron cut is applied (blue), electron veto cut $Bach_{PIDe} < 3$ applied (red), and the opposite to the electron veto $Bach_{PIDe} > 3$ cut applied (green).

Similarly to Reference [83], Figure 5.14 shows the background from $B^{\pm} \to De^{\pm}\nu_e$ is not observed in the $B^{\pm} \to D\pi^{\pm}$ or $B^{\pm} \to DK^{\pm}$ data, thus the application of a veto is not required.

Reference [83] found background from D-semileptonic decays to be neglible.

5.8.4 Cross-feed Bachelor Background

Misidentified bachelor candidates where the bachelor pion is reconstructed as a kaon in the $B^{\pm} \to D\pi^{\pm}$ mode, and the bachelor kaon is reconstructed as a pion in the $B^{\pm} \to DK^{\pm}$ channel result in cross-feed backgrounds. The $B^{\pm} \to D\pi^{\pm}$ decays have very similar topology to $B^{\pm} \to DK^{\pm}$ decays but have a significantly different CP asymmetry, thus it's important to be able to distinguish between them.

The previous selections and BDT are unable to discriminate between $B^{\pm} \to DK^{\pm}$ and $B^{\pm} \to D\pi^{\pm}$ events as no bachelor particle identification cuts or bachelor particle identification BDT input variables were used. Therefore, a cut on the combination of kaon hypothesis $ProbNN_K$ and pion hypothesis $ProbNN_{\pi}$ particle identification variables from the Neural network $ProbNN$ (see Section 3.2.2.4) of the charged kaon candidate in the DK mode, as well as charged pion candidate in the $D\pi$ channel are implemented:

$$varProbNN = ProbNN_K(1 - ProbNN_{\pi}) \tag{5.10}$$

Where $varProbNN$ is used to distinguish between the $B^{\pm} \to D\pi^{\pm}$ and $B^{\pm} \to DK^{\pm}$ events in the data sample. For the $B^{\pm} \to DK^{\pm}$ data sample we apply $varProbNN > Cut_{PID}$, whereas for the $B^{\pm} \to D\pi^{\pm}$ candidates we apply $varProbNN < Cut_{PID}$ where Cut_{PID} is the cut value (between 0 and 1) for both samples. The $varProbNN$ cut is used to suppress background from the misidentified events and has the added benefit of ensuring no decay is included in both samples.

The misidentified bachelor candidates in the $B^{\pm} \to DK^{\pm}$ mode are the most significant due to the relative branching fractions. The $B^{\pm} \to D\pi^{\pm}$ decay has a branching fraction over 10 fold greater than $B^{\pm} \to DK^{\pm}$ thus the cross-feed background in the DK mode needs particular attention. As a result, the optimal PID cuts value Cut_{PID} is chosen using figures of merit in section 5.9, in order to maximise the proportion of signal events in the DK mode signal region.

As previously explained in section 5.7, the effect of the bachelor PID cuts on simulation samples are obtained using PIDCalib2.

5.9 Selection Optimisation

To optimise the combination of BDT, PID and charmless background cuts on the data sample the variable $x = S/\sqrt{(S+B)}$ is maximised, where S is the number of signal events and B the number of background events in the DK signal region. It is desirable to optimise x in the DK mode since the signal events in this mode provide the vast majority of the sensitivity to the CKM angle γ.

This optimisation involves two-dimensional scans of x for the BDT cut and PID cut variables ($varProbNN$) across a range of Charmless background cut (FD_{sig_z}) variable values. For

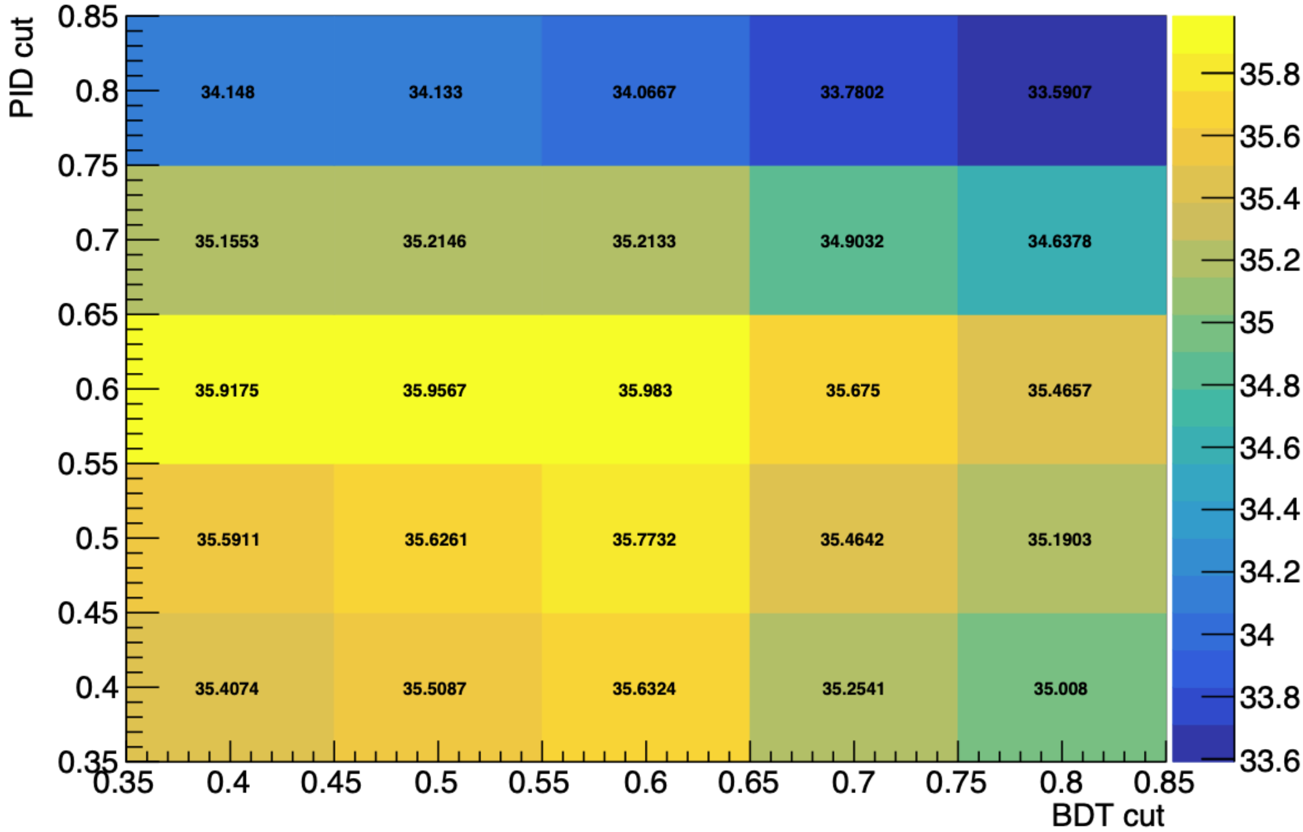

FIGURE 5.15. Figures of merit for the BDT cuts vs PID cuts for $FD_{sig_z} > 2$.

each configuration of cuts the invariant mass fit is performed, as outlined in Chapter 6, to obtain S and B in the DK signal region. S is the number of $B^{\pm} \rightarrow DK^{\pm}$ signal events determined in the global mass fit and B is the total background yield in the DK mode. Optimising the cuts using the data is not biasing because γ is mainly sensitive to the variation of events over the bins, and not the total number of events in the sample. Moreover, it would not be bias anyway as any requirements decided upon are taken into account by the efficiencies.

Figure 5.15 shows the optimal configuration of cuts where $FD_{sig_z} > 2$, BDT cut > 0.6 and PID cuts $varProbNN > 0.6$ in the DK mode and $varProbNN < 0.6$ in the $D\pi$ mode. As a result, these are chosen as the optimal selection and events not meeting these selections are removed. A complete list of all the selections applied after the preselections are outlined in Table 5.7.

Table 5.7: Further selection criteria for all $B^{\pm} \to D(\to 2\pi^{+}2\pi^{-})h^{\pm}$ decays.

Particle	Parameter	Selection Criteria
	BDT cut	> 0.6
D^0	FD_{sig_z}	> 2
Daughter $\pi^{\pm}$	$ProbNN_{\pi}(1-ProbNN_{K})$	> 0.2
	$m(\pi^{+}\pi^{-})$	< 505 MeV/c
	$m(\pi^{+}\pi^{-})$	> 480 MeV/c
$h^{\pm}$	p	> 3000 MeV
	p	< 100 GeV
	η	> 1.5
	η	< 5
	$nTracks$	> 0
	$nTracks$	< 500
Bachelor $K^{\pm}$	$ProbNN_{K}(1-ProbNN_{\pi})$	> 0.6
	$ISmuon$	== 0
Bachelor $\pi^{\pm}$	$ProbNN_{K}(1-ProbNN_{\pi})$	< 0.6
	$ISmuon$	== 0

5.10 Selection Efficiencies

Selection efficiency ratios are required for the global invariant mass fit and CP observable fit as explained in Chapters 6 and 7. The selection efficiency steps are defined consecutively as follows:

- ϵ_{geom}- The fraction of generated events that have all their decay products created within the LHCb detector acceptance is known as the geometrical or generator level efficiency.
- ϵ_{strip}- The fraction of reconstructed events produced in the LHCb acceptance that are selected by the stripping selections, outlined in Section 5.3, is known as the stripping efficiency.
- $\epsilon_{trigger}$- The fraction of events which have passed the stripping selection that are selected by the trigger selection criterion outlined in Section 5.2 is known as the trigger efficiency.
- ϵ_{pre}- The fraction of events which have passed the trigger requirements that are selected by the preselection criterion outlined in Section 5.5 is known as the preselection efficiency.
- ϵ_{BDT}- The fraction of events which have passed the preselections selected by the BDT selection criterion outlined in Section 5.6.6 is known as the BDT efficiency.

- ϵ_{other}- The fraction of events which have passed the BDT selection that are selected by the remaining selection criteria (apart from the bachelor PID) after the BDT outlined in Table 5.7 is the efficiency of the remaining selections.

- ϵ_{PID}- The fraction of events of events selected by the bachelor PID requirements outlined in Section 5.9 is the PID efficiency.

The efficiency ϵ_{geom} is extracted from the LHCb simulation logs and the efficiency ϵ_{strip} can obtained using bookkeeping. The other efficiencies of each selection stage, apart from the bachelor PID requirements, can be determined using the simulation samples, by taking the number of events in the sample in the current stage and dividing it by the number of events in the sample in the previous stage. The particle identification efficiencies for the bachelor cuts outlined in Table 5.7 are determined using PIDCalib2 (as explained in Section 5.7):

- $\epsilon^{PID}_{\pi\to\pi}$ = 99.265%

- $\epsilon^{PID}_{\pi\to K}$ = 0.7345%

- $\epsilon^{PID}_{K\to K}$ = 76.475%

- $\epsilon^{PID}_{K\to\pi}$ = 25.38%

The total efficiency of all the steps combined can be calculated using:

$$\epsilon_{total} = \epsilon_{geom} \times \epsilon_{strip} \times \epsilon_{trigger} \times \epsilon_{pre} \times \epsilon_{BDT} \times \epsilon_{other} \times \epsilon_{PID} \tag{5.11}$$

The total product of the consecutive efficiencies of each stage can be observed in Tables 5.8, 5.9 and 5.10 and 5.11. It was found that the total products of the consecutive signal and cross-feed efficiencies remained consistent across the D meson decay phase space bins as shown in Tables 5.12 and 5.13.

Ratios of the total efficiencies, rather than the absolute total efficiencies, are used in the simultaneous global invariant mass fit and the fit for the CP observables described in Chapter 6 and Chapter 7 respectively.

Table 5.8: Selection efficiencies from the signal and cross-feed simulation samples in the $B^{\pm} \to DK^{\pm}$ channel. The total efficiencies $\epsilon^{m_B}_{total}$ and ϵ^{CP}_{total} include the B mass window for the global mass fit and the B mass window for the CP fit respectively and both include the PID efficiencies determined using PIDCalib2.

Decay	Bachelor	ϵ_{geom} (%)	ϵ_{strip} (%)	ϵ_{trig} (%)	ϵ_{pre} (%)	ϵ_{BDT} (%)	ϵ_{other} (%)	$\epsilon^{m_B}_{total}$ (%)	ϵ^{CP}_{total} (%)
$B^{\pm} \to DK^{\pm}$	$K \to K$	16.53	3.88	95.81	88.29	96.26	47.88	0.19	0.19
$B^{\pm} \to D\pi^{\pm}$	$\pi \to K$	16.01	4.08	95.48	80.89	95.22	48.46	0.0017	0.0017

Table 5.9: Selection efficiencies from the signal and cross-feed simulation samples in the $B^{\pm} \to D\pi^{\pm}$ channel. The total efficiencies $\epsilon^{m_B}_{total}$ and ϵ^{CP}_{total} include the B mass window for the global mass fit and the B mass window for the CP fit respectively and both include the PID efficiencies determined using PIDCalib2.

Decay	Bachelor	ϵ_{geom} (%)	ϵ_{strip} (%)	ϵ_{trig} (%)	ϵ_{pre} (%)	ϵ_{BDT} (%)	ϵ_{other} (%)	$\epsilon^{m_B}_{total}$ (%)	ϵ^{CP}_{total} (%)
$B^{\pm} \to DK^{\pm}$	$K \to \pi$	0.1653	0.0382	95.51	76.23	96.30	47.06	0.053	0.047
$B^{\pm} \to D\pi^{\pm}$	$\pi \to \pi$	01601	0.0406	95.80	87.93	95.91	48.64	0.25	0.25

Table 5.10: Selection efficiencies from the partially reconstructed background simulation samples in the $B^{\pm} \to D\pi^{\pm}$ channel. The total efficiencies $\epsilon^{m_B}_{total}$ includes the signal PID efficiencies determined using PIDCalib2 and the B mass window for the global mass fit.

Decay	Bachelor	$\epsilon^{m_B}_{total}$ (%)
$B^{\pm} \to D^{*0}(\to D[\gamma])\pi^{\pm}$	$\pi \to \pi$	17.15
$B^{\pm} \to D^{*0}(\to D[\pi^0])\pi^{\pm}$	$\pi \to \pi$	16.52
$\overset{(-)}{B}{}^0 \to D^{*\mp}(\to D[\pi^{\mp}])\pi^{\pm}$	$\pi \to \pi$	14.31
$\overset{(-)}{B}{}^0 \to D\rho^0(\to \pi^{\pm}[\pi^{\mp}])$	$\pi \to \pi$	6.77
$B^{\pm} \to D\rho^{\pm}(\to \pi^{\pm}[\pi^0])$	$\pi \to \pi$	7.59

Table 5.11: Selection efficiencies from the partially reconstructed background simulation samples in the $B^{\pm} \to DK^{\pm}$ channel. The total efficiencies $\epsilon^{m_B}_{total}$ includes the signal PID efficiencies determined using PIDCalib2 and the B mass window for the global mass fit.

Decay	Bachelor	$\epsilon^{m_B}_{total}$ (%)
$B^{\pm} \to D^{*0}(\to D[\gamma])K^{\pm}$	$K \to K$	14.20
$B^{\pm} \to D^{*0}(\to D[\pi^0])K^{\pm}$	$K \to K$	13.37
$\overset{(-)}{B^0} \to D^{*\mp}(\to D[\pi^{\mp}])K^{\pm}$	$K \to K$	10.80
$\overset{(-)}{B^0} \to DK^{*0}(\to K^{\pm}[\pi^{\mp}])$	$K \to K$	6.17
$B^{\pm} \to DK^{*+}(\to K^{\pm}[\pi^0])$	$K \to K$	7.74
$B^{\pm} \to D^{*0}(\to D[\gamma])\pi^{\pm}$	$\pi \to K$	0.2004
$B^{\pm} \to D^{*0}(\to D[\pi^0])\pi^{\pm}$	$\pi \to K$	0.2150
$\overset{(-)}{B^0} \to D^{*\mp}(\to D[\pi^{\mp}])\pi^{\pm}$	$\pi \to K$	0.2018
$\overset{(-)}{B^0} \to D\rho^0(\to \pi^{\pm}[\pi^{\mp}])$	$\pi \to K$	0.0955
$B^{\pm} \to D\rho^{\pm}(\to \pi^{\pm}[\pi^0])$	$\pi \to K$	0.1081

Table 5.12: Selection efficiencies from the signal and cross-feed simulation samples in the $B^{\pm} \to DK^{\pm}$ channel for each bin used in the CP fit. The total efficiencies ϵ^{CP}_{total} includes the B mass window for the CP fit and the PID efficiencies determined using PIDCalib2.

Decay	Bachelor	ϵ^{CP}_{total} (%) bin -3	ϵ^{CP}_{total} (%) bin -2	ϵ^{CP}_{total} (%) bin -1	ϵ^{CP}_{total} (%) bin 1	ϵ^{CP}_{total} (%) bin 2	ϵ^{CP}_{total} (%) bin 3
$B^{\pm} \to DK^{\pm}$	$K \to K$	0.19	0.19	0.19	0.19	0.19	0.19
$B^{\pm} \to D\pi^{\pm}$	$\pi \to K$	0.0017	0.0017	0.0017	0.0017	0.0017	0.0017

Table 5.13: Selection efficiencies from the signal and cross-feed simulation samples in the $B^{\pm} \to D\pi^{\pm}$ channel for each bin used in the CP fit. The total efficiencies ϵ^{CP}_{total} includes the B mass window for the CP fit and the PID efficiencies determined using PIDCalib2.

Decay	Bachelor	ϵ^{CP}_{total} (%) bin -3	ϵ^{CP}_{total} (%) bin -2	ϵ^{CP}_{total} (%) bin -1	ϵ^{CP}_{total} (%) bin 1	ϵ^{CP}_{total} (%) bin 2	ϵ^{CP}_{total} (%) bin 3
$B^{\pm} \to DK^{\pm}$	$K \to \pi$	0.047	0.047	0.047	0.047	0.047	0.047
$B^{\pm} \to D\pi^{\pm}$	$\pi \to \pi$	0.25	0.25	0.25	0.25	0.25	0.25

CHAPTER 6

Invariant Global Mass Fit

The global mass fit is used to establish the invariant-mass-shape parametrisation for the subsequent measurement of the CP-violation observables. This chapter describes the signal and background components used in the extended maximum-likelihood fit [84] performed simultaneously to $B^{\pm} \to D\pi^{\pm}$ and $B^{\pm} \to DK^{\pm}$ data categories using the $RooFit$ package [85], and how they are determined. The general strategy described in Reference [29] is implemented.

6.1 Signal Shape

6.1.1 Signal Shape Parametrisation

The signal shape is modelled by the sum of a modified Cruijff probability density function (PDF) [86] [29], such that it does not tend towards a non-physical uniform mass distribution of $|m - m_B| \equiv |\Delta m| \gg \sigma$, and a Gaussian PDF $p_G(m|,_B, \sigma)$. The modified Cruijff PDF is:

$$p_c(m|m_b, \sigma, \alpha_L, \alpha_R, \beta) \propto \begin{cases} \exp\left[\frac{-\Delta m^2(1+\beta\Delta m^2)}{2\sigma^2+\alpha_L\Delta m^2}\right], & \Delta m = m - m_B < 0 \\ \exp\left[\frac{-\Delta m^2(1+\beta\Delta m^2)}{2\sigma^2+\alpha_R\Delta m^2}\right], & \Delta m = m - m_B > 0 \end{cases} \tag{6.1}$$

Common means and widths are shared between the Gaussian and modified Cruijff resulting in the signal PDF:

$$p_{signal}(m|m_b, \sigma, \alpha_L, \alpha_R, \beta) = f_c p_c(m|m_b, \sigma, \alpha_L, \alpha_R, \beta) + (1 - f_c) p_G(m|m_B, \sigma) \tag{6.2}$$

6.1.2 Determination of signal shape parameters

The signal PDF parameters α_L, α_R, f_c, β, are fixed from simulation samples as illustrated in Figure 6.1 and recorded in Table 6.1 . The simulation samples are processed through the full selection as outlined in Section 5, with the exception of the bachelor PID cuts. As previously explained in Section 5.7 the bachelor PID distribution is not well modelled in simulation, and thus the PIDCalib2 package is used to reweight the simulation samples and account for their efficiencies based on the η, p and $nTracks$ variables.

Table 6.1: Signal Shape parameters determined from fits to simulation samples and fixed in the mass fit to data.

Variable	$B^{\pm} \to DK^{\pm}$	$B^{\pm} \to D\pi^{\pm}$
α_L	0.1610 ± 0.0017	0.1780 ± 0.0011
α_R	0.1208 ± 0.0013	0.1244 ± 0.0008
f_c	0.697 ± 0.023	0.741 ± 0.013
β	$(8.9 \pm 1.1) \times 10^{-7}$	$(7.6 \pm 0.6) \times 10^{-7}$

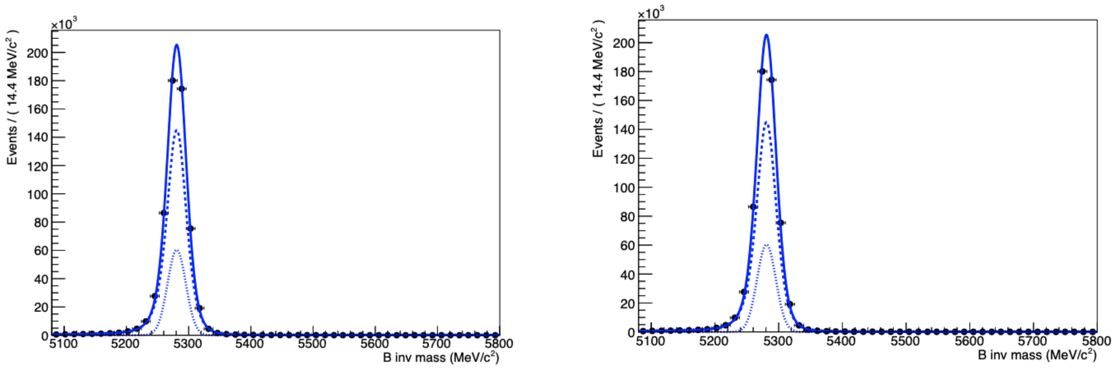

Figure 6.1: Fit to $B^{\pm} \to DK^{\pm}$ (left) and $B^{\pm} \to D\pi^{\pm}$ (right) signal simulation samples.

6.1.3 Signal Yields Definition

The DK signal yield N_{DK} is defined by:

$$N_{DK} = R_{DK/D\pi} \times N_{D\pi} \times \frac{\epsilon_{DK \to DK}}{\epsilon_{D\pi \to D\pi}} \tag{6.3}$$

The $D\pi$ signal yield $N_{D\pi}$ and the ratio of the $B^{\pm} \to DK^{\pm}$ and $B^{\pm} \to D\pi^{\pm}$ branching fractions $R_{DK/D\pi}$ are permitted to float in the fit to data. Both $B^{\pm} \to DK^{\pm}$ and $B^{\pm} \to D\pi^{\pm}$ efficiencies, $\epsilon_{DK \to DK}$ and $\epsilon_{D\pi \to D\pi}$, are fixed from the product of the combined selections efficiencies outlined in Tables 5.8 and 5.9.

6.2 Misidentified bachelor decays

6.2.1 Cross-feed Shape Parametrisation

The misidentified bachelor candidates result in a cross-feed between the $B^\pm \to DK^\pm$ and $B^\pm \to D\pi^\pm$ channels, where $B^\pm \to DK^\pm$ decays are reconstructed as $B^\pm \to D\pi^\pm$ decays and vice versa. The cross-feed from the misidentifed bachelor candidates in the $B^\pm \to DK^\pm$ channel is the most significant due to the relative branching fractions.

The misidentified bachelor shapes are obtained following the same procedure as Section 6.1.2. All the parameters for the Cruijff + Gausian cross-feed PDFs were fixed from $B^\pm \to D\pi^\pm$ misidentified as $B^\pm \to DK^\pm$ and $B^\pm \to DK^\pm$ misidentified as $B^\pm \to D\pi^\pm$ simulation samples as illustrated in Figure 6.2 and outlined in Table 6.2. As previously explained in Section 5.7 the bachelor PID cuts are not well modelled in simulation, and thus the PIDCalib2 package is used to reweight the simulation samples and account for their efficiencies based on the η, p and $nTracks$ variables.

Table 6.2: Cross-feed shape parameters determined from fits to simulation samples and fixed in the mass fit to data.

Fit Result		
Variable	$B^\pm \to DK^\pm$ recon as $B^\pm \to D\pi^\pm$	$B^\pm \to D\pi^\pm$ recon as $B^\pm \to DK^\pm$
μ	5233.7 ± 0.1	5327.6 ± 0.5
σ	19.68 ± 0.098	19.252 ± 0.7
α_L	0.2537 ± 0.0018	0.1767 ± 0.0092
α_R	0.1084 ± 0.0011	0.2626 ± 0.0159
f_c	1 ± 0.005	1 ± 0.094
β	$9 \times 10^{-14} \pm 1.9 \times 10^{-8}$	$(4.6 \pm 0.7) \times 10^{-6}$

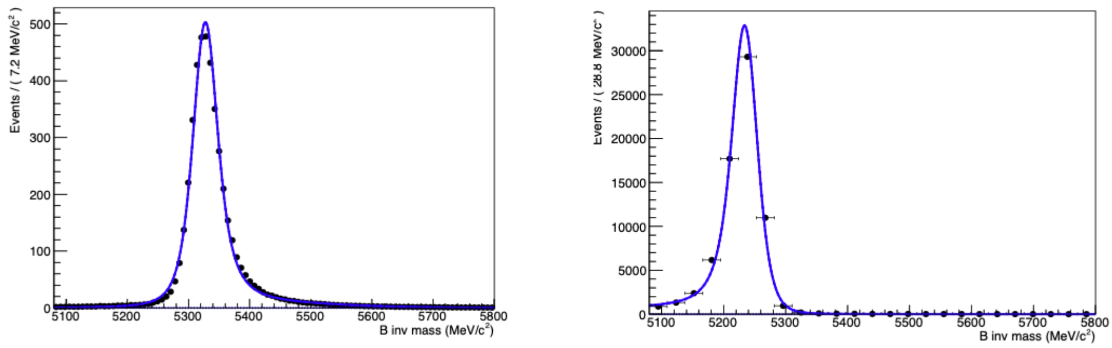

Figure 6.2: Fit to $B^{\pm} \to DK^{\pm}$ misidentified as $B^{\pm} \to D\pi^{\pm}$ (left) and $B^{\pm} \to D\pi^{\pm}$ misidentified as $B^{\pm} \to DK^{\pm}$ (right) cross-feed simulation samples. The small discrepancies in the tails of the left hand plot make a negligible difference since the cross feed contribution in the $B^{\pm} \to DK^{\pm}$ mode in the global invariant mass fit in Figure 6.16 is very small.

6.2.2 Definition of cross-feed yield

The $B^{\pm} \to DK^{\pm}$ misidentified as $B^{\pm} \to D\pi^{\pm}$ yield in the $D\pi$ mode $N^{D\pi\ mode}_{DK\to D\pi}$ is defined by:

$$N^{D\pi\ mode}_{DK\to D\pi} = N_{DK} \times \frac{\epsilon_{DK\to D\pi}}{\epsilon_{DK\to DK}}. \tag{6.4}$$

The $B^{\pm} \to D\pi^{\pm}$ misidentified as $B^{\pm} \to DK^{\pm}$ yield in the DK mode $N^{DK\ mode}_{D\pi\to DK}$ is defined by:

$$N^{DK\ mode}_{D\pi\to DK} = N_{D\pi} \times \frac{\epsilon_{D\pi\to DK}}{\epsilon_{D\pi\to D\pi}}. \tag{6.5}$$

All efficiencies are fixed from the product of the combined selections efficiencies outlined in Tables 5.8 and 5.9.

6.3 Partially reconstructed background decays

When a particle within a decay is not reconstructed the decay is described as partially reconstructed. Multiple partially reconstructed background candidates derive from $B \to Dh[X]$ decays where X is not reconstructed and is either $\pi^{\pm}$, γ (photon), or π^0. These decays are too similar to the signal decays to be rejected in the selection. The reduced momentum leads to the B masses being reconstructed at lower values than the true B mass and are thus low mass backgrounds.

The invariant mass distribution of each of these partially reconstructed backgrounds is dependent on the mass and spin of the missing particle and are modelled with analytical PDFs (see Section 6.3.1). The kinematic endpoints (a and b) of the PDFs are defined by the particle masses in the decay using four-momentum conservation. Moreover, the helicity angle of the missing particle has a one to one relation to its missing momentum, consequently the invariant B mass depends directly on the helicity angle (and thus the angular distribution of the missing particle). The spin-parity of the missing particle dictates one of two possible mass distributions.

If the missing particle is a $\pi^{\pm}$ or π^0 with spin-party 0^-, then the mass distribution is parametrised by a parabola with positive curvature (Equation 6.6) convolved with a Gaussian resolution function known as a HORNSdini PDF [87]. The HORNSdini shape describes the double-peak structure produced when a scalar (spin 0) particle is missing in the decay of a vector resonance such as $B \to D^*(\to D[\pi])h$ resulting in $m(Dh)$. In this example the angle between the $[\pi]$ momentum vector in the D^* rest frame and the D^* boost vector in the B rest frame is the D^* helicity angle. The most likely direction the missing $[\pi]$ will travel in will be where the helicity angle is either 0 or π. In the case of the helicity angle being equal to π the proportion of momentum carried by the missing $[\pi]$ is higher, resulting in a lower reconstructed $m(Dh)$. The opposite is true when the helicity angle is equal to 0. This results in the B mass distribution according to the parabola $p^0_{HORNS}(x)$ which peaks near both kinematic endpoints a and b :

$$p^0_{HORNS}(x) = \begin{cases} (x - \frac{a+b}{2})^2, & if\ a < x < b \\ 0, & otherwise \end{cases} . \tag{6.6}$$

Whereas, the parabola in the parametrisation has negative curvature (Equation 6.7) if the missing particle is a γ (photon) with spin-parity 1^- and thus the distribution is known as a HILLdini PDF [87]. When the missing particle in the decay of the vector resonance is a vector (spin 1) particle such as in the case of $B^{\pm} \to D^{*0}(\to D[\gamma])h^{\pm}$, the spin-parity means that the missing photon will predominantly travel in the direction of helicity angles $\frac{\pi}{2}$ or $\frac{3\pi}{2}$.Thus, there will not be a double-peak structure and the B mass distribution results in a parabola $p^0_{HILL}(x)$:

$$p^0_{HILL}(x) = \begin{cases} -(x-a)(x-b), & if\ a < x < b \\ 0, & otherwise \end{cases} . \tag{6.7}$$

Resolution effects in the determination of the momentum require the parabolic shapes to each be convolved with a double Gaussian resolution function:

$$p_{DG}(x) = p_{DG}(x|\mu,\sigma) + f_G p_G(x|\mu, R_\sigma \sigma) \tag{6.8}$$

where the width of the first Gaussian is σ, the relative fraction between the two Gaussians is f_G and their relative width is R_σ.

Moreover, in the HORNSdini case selection efficiency differences can result in peaks with varying heights to each other. A linear polynomial with slope parameter ξ is included in the formalism such that ξ is defined as the height of the left peak, relative to the right peak- the left peak decreases in height relative to the right peak as ξ tends to 0. This leads to the following HILLdini and HORNSdini distributions:

$$p_{HORNS/HILL}(m) = \int_a^b dx p^0_{HORNS/HILL}(x) p_{DG}(m|x,\sigma,f_G,R_\sigma)\Big(\frac{1-\xi}{b-a}x + \frac{b\xi - a}{b-a}\Big) \tag{6.9}$$

A term to describe the translation of the full HILLdini and HORNSdini shapes δm is also added. The term δm is shared between all HILLdini and HORNSdini PDFs in the remainder of the analysis.

6.3.1 Partially Reconstructed Background Shapes

The parameters for the shapes used for the partially reconstructed backgrounds within the global mass fit are described below. The monte carlo simulation samples mentioned in Section 5.1.2 are weighted with their respective PIDCalib2 efficiency weights.

6.3.2 Partially reconstructed $B \to D^* h^\pm$ decays background

A significant element of the partially reconstructed background in both $B^\pm \to DK^\pm$ and $B^\pm \to D\pi^\pm$ modes are from $B^\pm \to D^* h^\pm$ decays, where $h^\pm$ can be $K^\pm$ or $\pi^\pm$:

- $B^\pm \to D^{*0}(\to D[\gamma])h^\pm$ modelled with a HILLdini PDF.
- $B^\pm \to D^{*0}(\to D[\pi^0])h^\pm$ modelled with a HORNSdini PDF.
- $\overset{(-)}{B^0} \to D^{*\mp}(\to D[\pi^\mp])h^\pm$ modelled with a HORNsdini PDF.

The mass resolution $\sigma^{part.}$ of the $B^\pm \to D^{*0}(\to D[\pi^0])h^\pm$ and $\overset{(-)}{B^0} \to D^{*\mp}(\to D[\pi^\mp])h^\pm$ HORNSdini PDFs are not well modelled in simulation, hence the widths are left free to float in the fit and shared between their PDFs. The mass shift parameter δm is also left free to float in the fit and shared between all the HORNS/HILLdini PDFs set out in Section 6.3. The remaining parameters of the HORNSdini PDFs, apart from the kinematic endpoints, are shared and fixed from simulation samples. The kinematic end points differ for each background individually for the decays described by HORNSdini PDFs above and are fixed from simulation samples. All the parameters for these shapes used in the global fit are summarised in Table 6.3 and obtained from fits to simulation illustrated in Figures 6.3 to 6.6.

The parameters for the $B^\pm \to D^{*0}(\to D[\gamma])h^\pm$ HILLdini PDFs, apart from the kinematic endpoints and δm, are shared and fixed from simulation samples. The kinematic end points

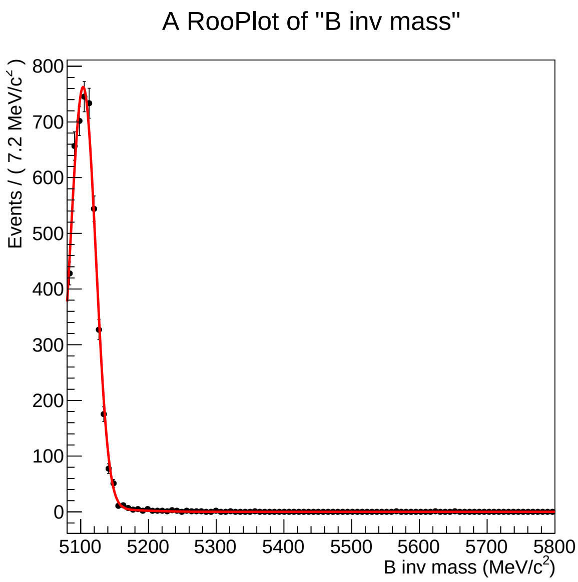

FIGURE 6.3. HORNSdini fit to $B^{\pm} \to D^{*0}(\to D[\pi^0])\pi^{\pm}$ simulation sample.

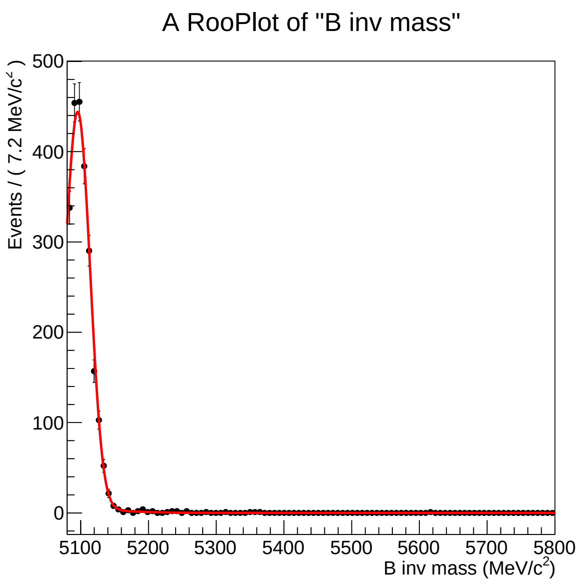

FIGURE 6.4. HORNSdini fit to $\overset{(-)}{B}{}^0 \to D^{*\mp}(\to D[\pi^{\mp}])\pi^{\pm}$ simulation sample.

differ for each individual background decay described by HILLdini PDFs and are fixed from simulation samples. All the parameters for these shapes used in the global fit are summarised in Table 6.4 and obtained from fits to simulation illustrated in Figures 6.7 and 6.8.

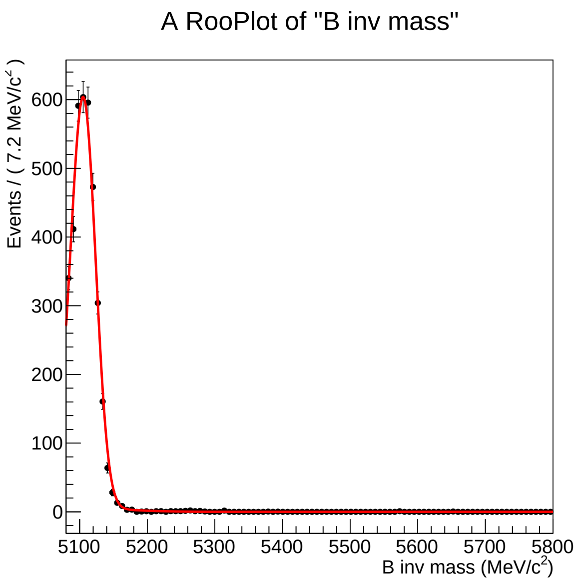

FIGURE 6.5. HORNSdini fit to $B^{\pm} \to D^{*0}(\to D[\pi^0])K^{\pm}$ simulation sample.

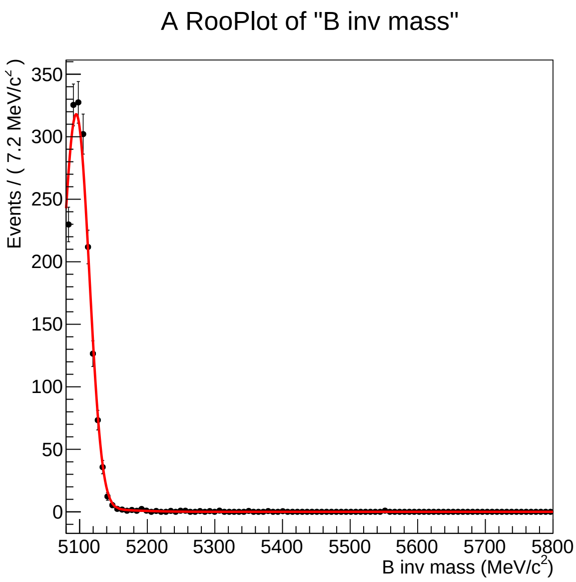

FIGURE 6.6. HORNSdini fit to $\overset{(-)}{B^0} \to D^{*\mp}(\to D[\pi^{\mp}])K^{\pm}$ simulation sample.

6.3.3 Partially reconstructed $B^{\pm(0)} \to D^0 h^{\pm}[\pi^{0(\mp)}]$ decays background

Within the $B^{\pm} \to D\pi^{\pm}$ mode, there are partially reconstructed $B \to D^0\pi^{\pm}[\pi]$ backgrounds from $\overset{(-)}{B^0} \to D\pi^{\pm}[\pi^{\mp}]$ and $B^{\pm} \to D\pi^{\pm}[\pi^0]$ decays. These decays are described by a HORNsdini PDF and all shape parameters, apart from δm, are fixed from $\overset{(-)}{B^0} \to D\rho^0$ and $B^{\pm} \to D\rho^{\pm}$ simulation

Table 6.3: Partially reconstructed $B^{\pm} \rightarrow D^{*0}h^{\pm}$ decay HORNSdini PDF parameters determined from fits to simulation samples and used in the global mass fit to data.

Fit Result				
	$B^{\pm} \rightarrow D^{*0}(\rightarrow D[\pi^0])h^{\pm}$		$\overset{(-)}{B^0} \rightarrow D^{*\mp}(\rightarrow D[\pi^{\mp}])h^{\pm}$	
Variable	Recon. as $B^{\pm} \rightarrow DK^{\pm}$	Recon. as $B^{\pm} \rightarrow D\pi^{\pm}$	Recon. as $B^{\pm} \rightarrow DK^{\pm}$	Recon. as $B^{\pm} \rightarrow D\pi^{\pm}$
$a[MeV/c$	5021.4	5015.6	4990.9	5020.0
$b[MeV/c]$	5114.9	5113.7	5106.4	5104.5
ξ	0.0004	0.0004	0.0004	0.0004
f_{σ}	0.9734	0.9734	0.9734	0.9734
R_{σ}	3.8195	3.8195	3.8195	3.8195
σ	shared, floated	shared, floated	shared, floated	shared, floated
δm	shared, floated	shared, floated	shared, floated	shared, floated

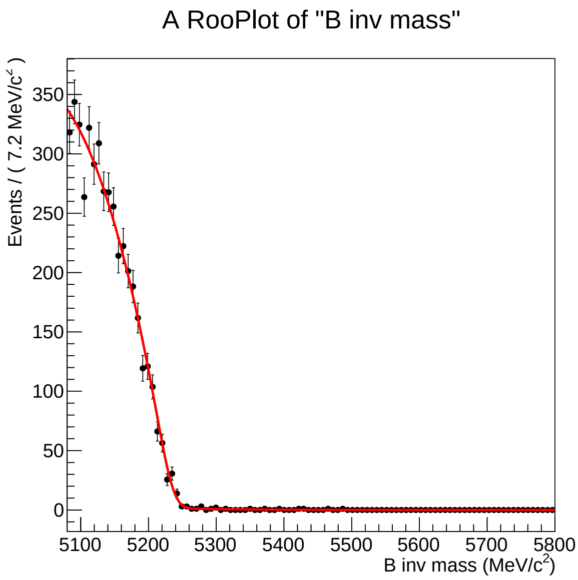

FIGURE 6.7. HILLdini fit to $B^{\pm} \rightarrow D^{*0}(\rightarrow D[\gamma])\pi^{\pm}$ simulation sample.

samples as shown in Fig. 6.9 and outlined in Table 6.5.

The $B^{\pm} \rightarrow D^0K^{\pm}$ mode has a partially reconstructed $B \rightarrow D^0K^{\pm}[\pi]$ background from $\overset{(-)}{B^0} \rightarrow DK^{\pm}[\pi^{\mp}]$ and $B^{\pm} \rightarrow DK^{\pm}[\pi^0]$ decays. This channel also has an additional $B_s^0 \rightarrow D^0K^{\pm}[\pi^{\mp}]$ background. Both these background decays are described using HORNSdini PDFs where all the shapes parameters, apart from δm, are fixed from simulation samples as can be seen in Figures 6.10 and 6.11 and stated in Tables 6.6 and 6.7.

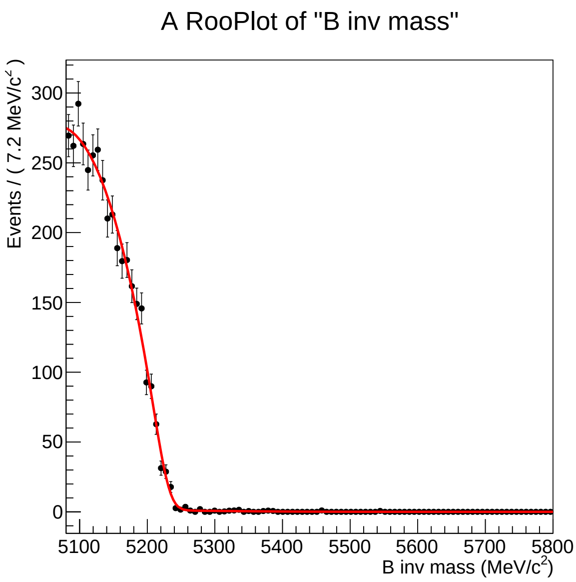

FIGURE 6.8. HILLdini fit to $B^{\pm} \to D^{*0}(\to D[\gamma])K^{\pm}$ simulation sample.

Table 6.4: Partially reconstructed $B^{\pm} \to D^{*0}h^{\pm}$ decay HILLdini PDF parameters determined from fits to simulation samples and used in the global mass fit to data.

$B^{\pm} \to D^{*0}(\to D[\gamma])h^{\pm}$		
Variable	Recon. as $B^{\pm} \to DK^{\pm}$	Recon. as $B^{\pm} \to D\pi^{\pm}$
$a[MeV/c]$	4738.3	4583.6
$b[MeV/c]$	5230.7	5235.4
ξ	0.0230	0.0230
f_{σ}	0.9920	0.9920
R_{σ}	11.202	11.202
σ	12.505	12.505
δm	shared, floated	shared, floated

6.3.4 Misidentified partially reconstructed decays background

Finally, all the partially reconstructed background contributions in the $B^{\pm} \to D\pi^{\pm}$ mode are also reconstructed in the $B^{\pm} \to DK^{\pm}$ mode, where the bachelor pion is misidentified as a kaon. These decays are described by HORNSdinimisID and HILLdinimisID PDFs [87] (effectively the sum of multiple HORNS/HILLdini PDFs) and the parameters are fixed from simulation samples where the bachelor is reconstructed as a kaon and are summarised in Table 6.8 and shown in Figures 6.12 to 6.14.

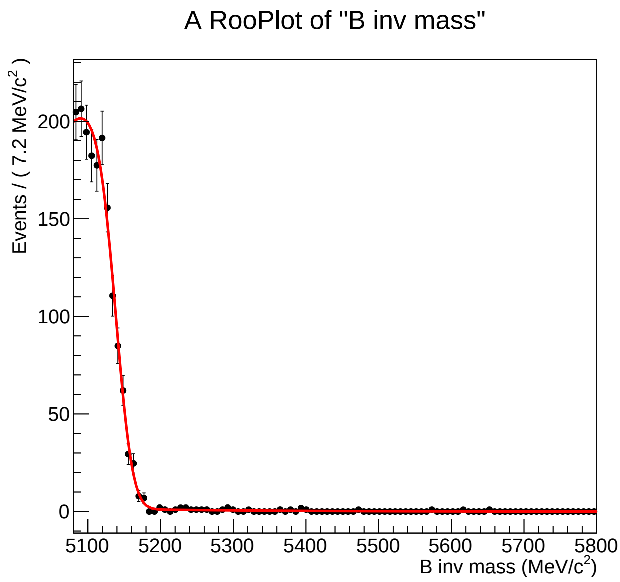

FIGURE 6.9. HORNSdini fit to $B \to D^0\rho$, $B \to D^0\pi^{\pm}[\pi]$ simulation samples.

Table 6.5: Partially reconstructed $B \to D^0\pi^{\pm}[\pi]$ decay HORNSdini PDF parameters determined from fit to simulation samples and used in the global masss fit to data.

$B \to D^0\pi^{\pm}[\pi]$	
Variable	Recon. as $B^{\pm} \to D\pi^{\pm}$
$a[MeV/c]$	4652.3
$b[MeV/c]$	5139.9
ξ	10.187
f_{σ}	0.98634
R_{σ}	14.262
σ	17.802
δm	shared, floated

6.3.5 Partially Reconstructed Background Yields

A summary of the partially reconstructed backgrounds and their associated background number is provided in Table 6.9. In the $D\pi$ channel the yield of partially reconstructed background number 1 ($N_{part._1}$) is permitted to float in the mass fit to data. The yield of partially reconstructed background number 2 is fixed relative to background number 1 using simulation signal PID efficiencies, simulation background selection efficiencies and relative branching ratios. The fraction of the sum of background numbers 1 and 2 which result in the yield of background number 3 is denoted by $f^{D\pi}_{D^*\gamma}$ and floated in the fit . Furthermore, the fraction of the sum of background numbers 1, 2 and 3 which determines the yield of background number

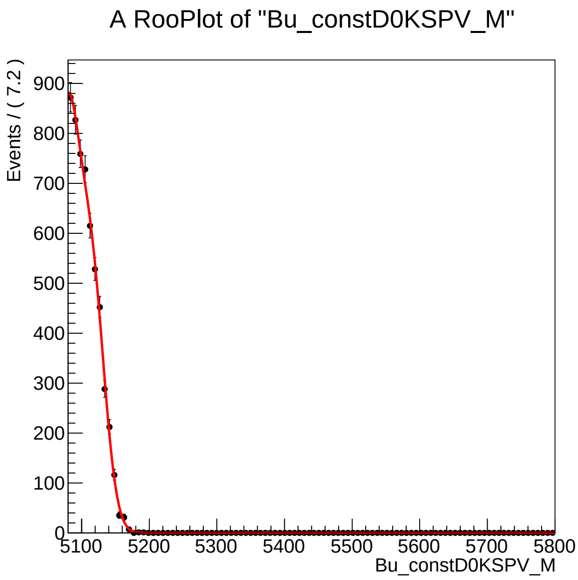

FIGURE 6.10. HORNSdini fit to $B \to D^0K^{\pm}[\pi]$ simulation samples based.

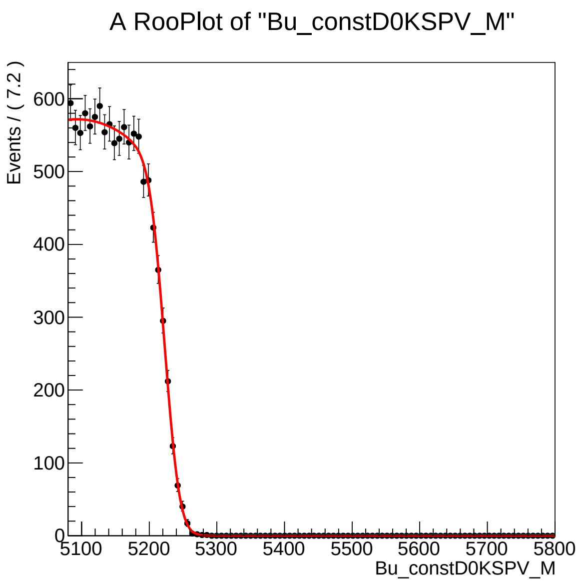

FIGURE 6.11. HORNSdini fit to $B_s^0 \to D^0K^{\pm}[\pi^{\mp}]$ simulation samples based.

4 is also floated in the fit and denoted as $f_{D\pi\pi}^{D\pi}$.

The total yield of partially reconstructed backgrounds in the $B^{\pm} \to D\pi^{\pm}$ mode is related to the total yield of the partially reconstructed backgrounds in the $B^{\pm} \to DK^{\pm}$ mode, apart from the B_s^0 background using:

Table 6.6: Partially reconstructed $B \to D^0K^{\pm}[\pi]$ decay HORNSdini PDF parameters used in the global fit to data.

$B \to D^0K^{\pm}[\pi]$	
Variable	Recon. as $B^{\pm} \to DK^{\pm}$
$a[MeV/c]$	5070.4
$b[MeV/c]$	5121.3
ξ	1.9036
f_{σ}	0.9271
R_{σ}	0.9919
σ	18.724
δm	shared, floated

Table 6.7: Partially reconstructed $B_s^0 \to D^0K^{\pm}[\pi^{\mp}]$ decay HORNSdini PDF parameters used in the global fit to data.

$B_s^0 \to D^0K^{\pm}[\pi^{\mp}]$	
Variable	Recon. as $B^{\pm} \to DK^{\pm}$
$a[MeV/c]$	3668.0
$b[MeV/c]$	5223.2
ξ	9.0152
f_{σ}	0.9706
R_{σ}	1.6137
σ	17.275
δm	shared, floated

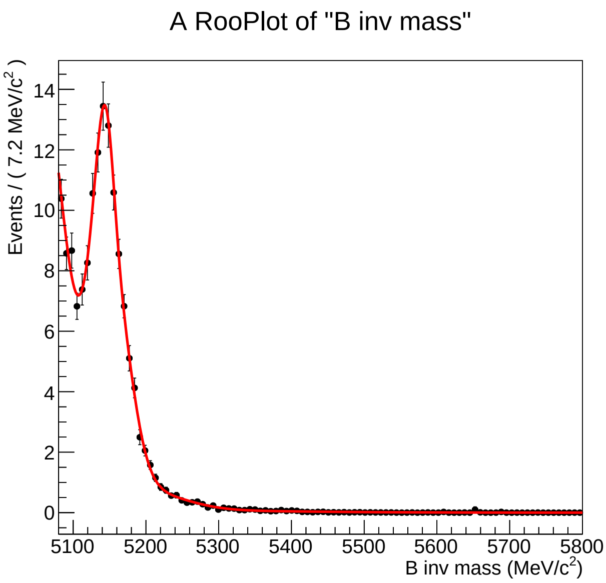

FIGURE 6.12. HORNSdinimisID fit to $B \to D^*(\to D[\pi])\pi$ reconstructed as $B \to D^*(\to D[\pi])K$ simulation samples.

$$N_{DK,part.} = R^{part.}_{DK/D\pi} \times N_{D\pi,part.} \times \frac{\epsilon_{DK\to DK,part.}}{\epsilon_{D\pi\to D\pi,part.}}. \tag{6.10}$$

The PID efficiencies are assumed to be identical between signal and partially reconstructed background and therefore taken from signal studies, all other efficiencies are fixed from the partially reconstructed background simulation samples - a combination of all partially reconstructed background simulation samples weighted according to relative simulation selection efficiencies and branching ratios. The ratio of the $B^{\pm} \to DK^{\pm}$ channel partially reconstructed

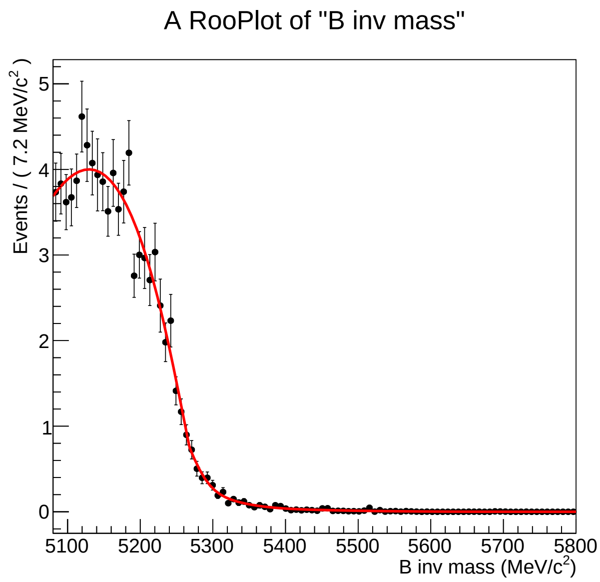

FIGURE 6.13. HILLdinimisID fit to $B \to D^*(\to D[\gamma])\pi$ reconstructed as $B \to D^*(\to D[\gamma])K$ simulation sample.

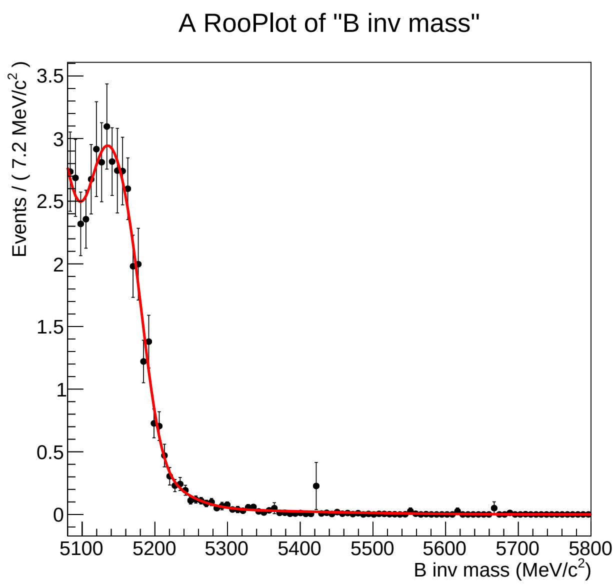

FIGURE 6.14. HORNSdinimisID fit to $B \to D\pi[\pi]$ reconstructed as $B \to DK[\pi]$ simulation samples.

and $B^{\pm} \to D\pi^{\pm}$ channel partially reconstructed background branching fractions $R^{part.}_{DK/D\pi}$is floated and shared between all categories.

In the DK channel, the relative yields of partially reconstructed backgrounds numbered 5-8

Table 6.8: Partially reconstructed background parameters where a bachelor pion has been reconstructed as a kaon used in the global fit to data.

	$B \to D^*(\to D[\pi])\pi$	$B \to D^*(\to D[\gamma])\pi$	$B \to D\pi[\pi]$
Variable	Recon. as $B^\pm \to DK^\pm$	Recon. as $B^\pm \to DK^\pm$	Recon. as $B^\pm \to DK^\pm$
$a[MeV/c]$	5009.3	4797.9	4994.8
$b[MeV/c]$	5105.3	5231.9	5117.7
ξ	1.0394	0.0082	1.2997
f_1	0.2300	0.47669	0.4660
f_2	0.6585	0.1981	0.1269
f_3	0.0366	0.3387	0.0463
$\mu_1[MeV/c^2]$	46.070	47.062	56.317
$\mu_2[MeV/c^2]$	55.745	46.188	77.367
$\mu_3[MeV/c^2]$	64.661	35.764	102.09
$\mu_4[MeV/c^2]$	116.32	180.55	18.696
$\sigma_1[MeV/c^2]$	9.8309	22.085	23.422
$\sigma_2[MeV/c^2]$	24.881	63.413	49.999
$\sigma_3[MeV/c^2]$	200.01	0.0054	199.89
$\sigma_4[MeV/c^2]$	50.002	119.80	20.410

and 10 are all fixed from simulation signal PID efficiencies, simulation background efficiencies and relative branching fractions. The yield of background number 10 was corrected using a correction factor $\epsilon_{m_{Dh}} = \frac{N_{m_{Dh}\ in\ fit\ range}}{N_{survive\ selection}}$ derived from simulation samples, due to the fact that more events fall inside the mass range when the pion is reconstructed as a kaon as m_{Dh} is shifted to a higher mass region.

The $B_s^0 \to DK^\pm[\pi^\mp]$ needs to be determined separately due to the K^- bachelor being predominantly produced with $\bar{D}^0$ mesons such that $B_s^0 \to \bar{D}^0[\pi^+]K^-$, and the K^+ bachelor being predominantly produced with D^0 meson such that $\bar{B}_s^0 \to D^0[\pi^-]K^+$. This is the opposite to the other background and signal decays where the bachelor K^- bachelor is predominantly produced with a D^0 meson, and the K^+ bachelor is predominantly produced with a $\bar{D}^0$ meson. This is achieved using the data-driven approach [83]. In this measurement the yield of B_s^0 background in the DK mode can be fixed relative to the number of signal events in the $D\pi$ mode similarly to the analysis in Reference [88] . Moreover, the associated ratio from Reference [88] is used and corrected for this analysis's mass range and PID cuts to provide the expected ratio in this BPGGSZ analysis:

$$\frac{N_{B_s^0}^{BPGGSZ}}{N_{D\pi}^{BPGGSZ}} = \frac{N_{B_s^0}^{BPGGSZ\ old}}{N_{D\pi}^{BPGGSZ\ old}} \times \frac{N_{B_s^0}^{MC}(m_B > 5080MeV)}{N_{B_s^0}^{MC}(m_B > 4900MeV)} \times \frac{\epsilon_{DK\to DK}(ProbNN > 0.6)}{\epsilon_{DK\to DK}(PIDK > 12)} \times \frac{\epsilon_{D\pi\to D\pi}(PIDK < 12)}{\epsilon_{D\pi\to D\pi}(ProbNN < 0.6)}, \tag{6.11}$$

where $ProbNN = Kaon_{ProbNN_k} \times (1 - Kaon_{ProbNN_\pi})$. This calculation results in 5.2×10^{-3} thus, the number of signal events in the $D\pi$ channel can be related to the B_s^0 background yield by this scale factor.

Table 6.9: Summary of partially reconstructed backgrounds.

Number	Decay	PDF
1	$B^\pm \to D^{*0}(\to D[\pi^0])\pi^\pm$	HORNSdini
2	$\overset{(-)}{B^0} \to D^{*\mp}(\to D[\pi^\mp])\pi^\pm$	HORNSdini
3	$B^\pm \to D^{*0}(\to D[\gamma])\pi^\pm$	HILLdini
4	$B \to D^0\pi^\pm[\pi]$	HORNSdini
5	$B^\pm \to D^{*0}(\to D[\pi^0])K^\pm$	HORNSdini
6	$\overset{(-)}{B^0} \to D^{*\mp}(\to D[\pi^\mp])K^\pm$	HORNSdini
7	$B^\pm \to D^{*0}(\to D[\gamma])K^\pm$	HILLdini
8	$B \to D^0K^\pm[\pi]$	HORNSdini
9	$B_s^0 \to D^0K^\pm[\pi^\mp]$	HORNSdini
10	$B \to Dh^\pm[X]$ cross-feed	{HORNS/HILL}dinimisID

6.4 Charmless Backgrounds

Charmless backgrounds in the data, coming from from $B \to 4\pi^\pm h^\pm$ decays, need to be accounted for. These background are located under the B mass signal peak so the charmless shape parameters and yield are estimated and fixed from the D meson upper mass sideband $1920-1970MeV/c^2$ of the $B^\pm \to Dh^\pm$ data, where an exponential distribution is used to describe the combinatorial background and a Gaussian distribution is used to model the charmless component as illustrated in Figure 6.15 . The flight distance significant cut in the z direction FD_{sig_z} significantly reduces the charmless background in the DK mode and eradicates the charmless background in the $D\pi$ mode. The FD_{sig_z} cut does not completely remove the background in the DK mode, therefore it has to be modelled in the fit. The charmless background shape parameters and yield are contained in Table 6.10.

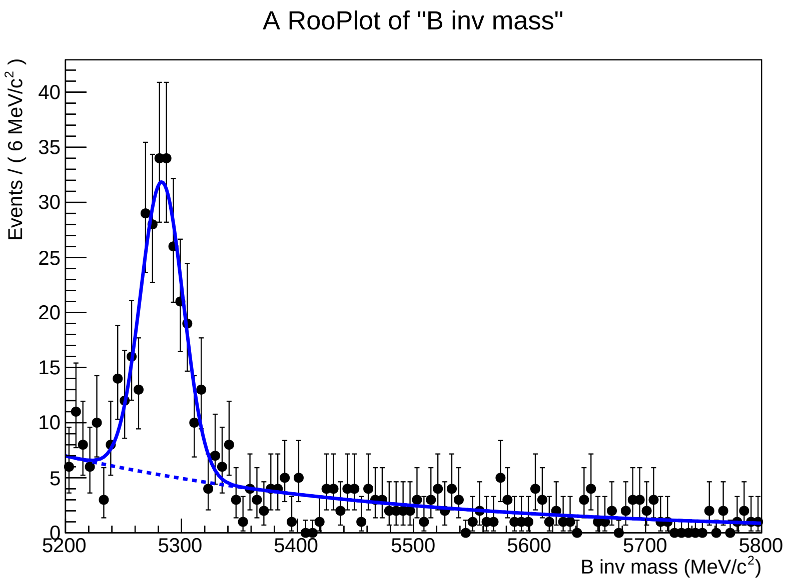

FIGURE 6.15. Fit to Charmless background in D upper sideband of $B^{\pm} \to DK^{\pm}$ data.

Table 6.10: Charmless shapes parameters and yields used in the global fit to data.

$B^{\pm} \to 4\pi^{\pm}K^{\pm}$ Charmless Background	
Variable	$B^{\pm} \to DK^{\pm}$
μ	5283.1
σ	18.4
N	204.8

6.5 Combinatorial Backgrounds

An exponential distribution is used to describe the combinatorial background in each data category. The yields $N_{DK,comb}$, $N_{D\pi,comb}$ and slopes α_{DK}, $\alpha_{D\pi}$ of the backgrounds are floated in the respective DK and $D\pi$ modes independently.

6.6 Global mass fit results

An extended maximum likelihood fit is performed simultaneously to both $B^{\pm} \to DK^{\pm}$ and $B^{\pm} \to D\pi^{\pm}$ categories on 2017 Run 2 data over the mass range $5080-5800 MeV/c^2$. The range is sufficient to include the higher mass peak of the double-peaked partially reconstructed backgrounds, in order to help the fit constrain the relative contributions of low mass backgrounds. The upper mass range provides sufficient combinatorial background to establish accurate exponential shapes parameters.

The fit is undertaken in two steps. The first step does not include a global shift parameter, and the fit is used to establish the global shift parameter set to the difference between the measured signal mean in the data and signal mean in the simulated samples. This global shift is then added and fixed in the fit to the data in the separate second step and applied to the non-signal decay means. The fit in the second step is illustrated in Figure 6.16 and the fitted parameters and yields are given in Tables 6.11 and 6.12.

Table 6.11: Global invariant mass fit parameters.

Variable	Value
Signal shape parameters	
$\mu\,[MeV]$	5279.00 ± 0.116
$\sigma_{D\pi}\;[MeV]$	16.14 ± 0.1025
$\sigma_{DK}\;[MeV]$	15.23 ± 0.4657
Partially reconstructed background parameters	
$\sigma^{part.}\;[MeV]$	15.95 ± 0.9343
$f^{D\pi}_{D^*\gamma}$	0.5319 ± 0.0448
$f^{D\pi}_{D\pi\pi}$	0.4010 ± 0.09079
δm	0.6901 ± 0.39030
Combinatorial gradients (10^{-3})	
$\alpha_{D\pi}$	-3.4180 ± 0.3036
α_{DK}	-2.3956 ± 0.4858

Table 6.12: Global invariant mass fit yields.

Variable	Value
Signal yields	
N_{DK}	1725.04
$N_{D\pi}$	29804.70 ± 187.54
$R_{DK/D\pi}$ (10^{-2})	7.57 ± 0.22
Partially reconstructed background yields	
$N_{part._1}$	6514.6 ± 575.33
$N_{DK,part.}$	1099.28
$N_{D\pi,part.}$	21196.7
$R^{part.}_{DK/D\pi}$ (10^{-2})	5.44 ± 0.24
Combinatorial yields	
$N_{D\pi,comb}$	2495.23 ± 187.54
$N_{DK,comb}$	474.03 ± 55.35

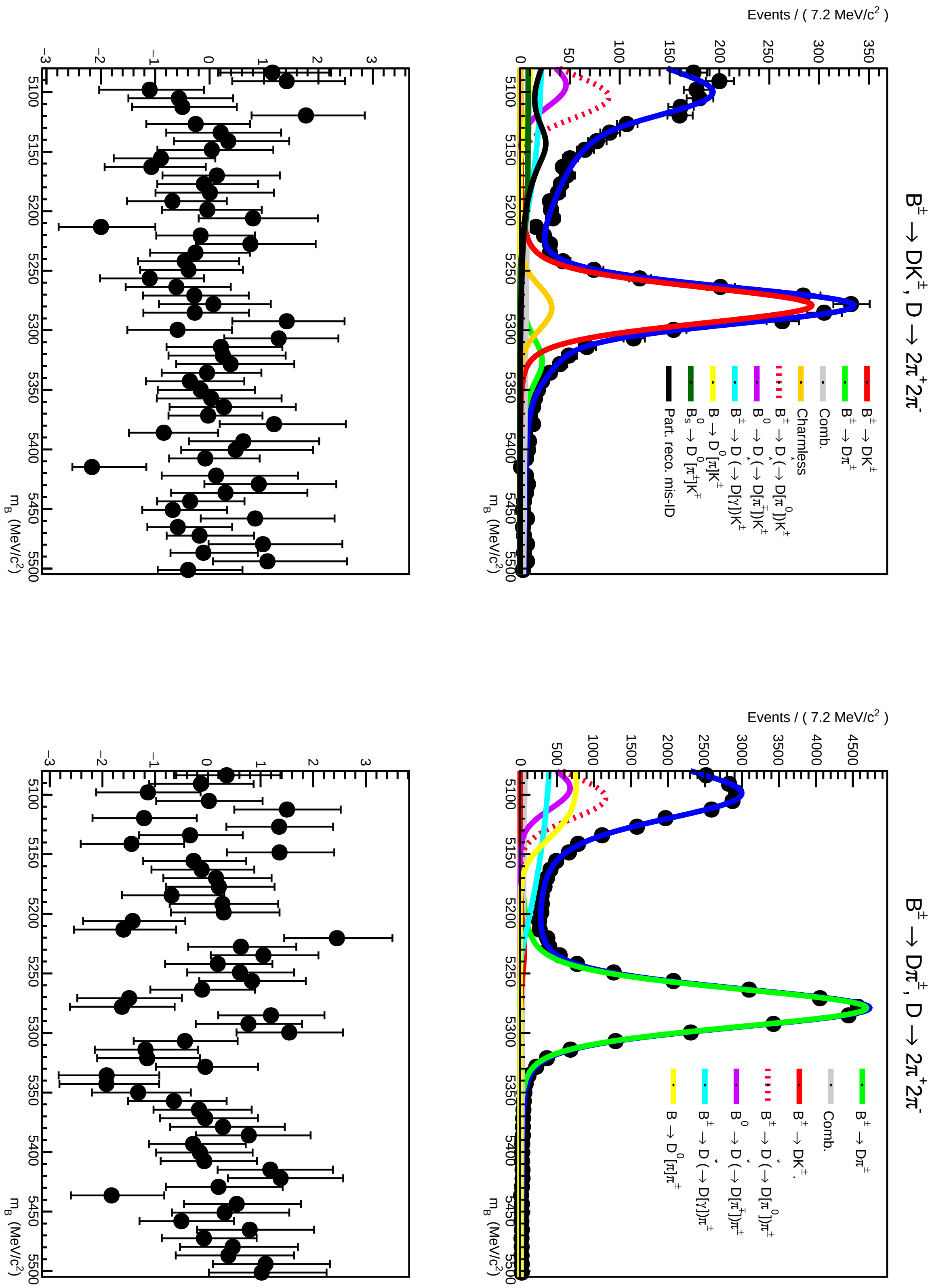

FIGURE 6.16. Simultaneous global invariant mass fit distributions for the $B^{\pm} \to DK^{\pm}$ and $B^{\pm} \to D\pi^{\pm}$ modes.

CHAPTER 7

CP Observables Fit

The CP fit is used to determine the CP-violation observables $x_{\pm}^{DK}$ and $y_{\pm}^{DK}$ and the nuisance parameters $x_{\xi}^{D\pi}$ and $y_{\xi}^{D\pi}$. This chapter describes the extended maximum-likelihood fit set up and results. The general strategy described in Reference [29] is implemented.

7.1 CP Fit Setup

The data is split by $B^{\pm} \rightarrow DK^{\pm}$ and $B^{\pm} \rightarrow D\pi^{\pm}$ decay modes as in the invariant global mass fit. Additionally, the data is further split by B charge and D decay bin number. There are 2 decay modes, 2 B charges and 6 D decay bins for each B charge, resulting in a total of 24 categories. A simultaneous, unbinned, extended maximum likelihood fit [84] is performed using the $RooFit$ package [85] over the slightly reduced B mass range of $5150\ MeV < M_B < 5800\ MeV$ compared to the global mass fit, as motivated in Section 7.1.4. The fit is performed in 2 steps, where all the shape parameters are fixed from the global invariant mass fit. In each $DK^{\pm}$ and $D\pi^{\pm}$ category there are 4 yield components which the remaining categories have in common:

1. A signal yield component for the $B^{\pm} \rightarrow DK^{\pm}$ or $B^{\pm} \rightarrow D\pi^{\pm}$ signal decay yield in each category. The total yield of each signal B decay and B charge across all bins are floated as independent variables, resulting in 4 variables. The individual bin yields are then derived from the respective total B decay and B charge yields using Equation 7.1.
2. A cross-feed yield component for $B^{\pm} \rightarrow DK^{\pm}$ decays reconstructed as $B^{\pm} \rightarrow D\pi^{\pm}$ decays or visa versa in each category. The respective cross feed yields in each B charge and bin are fixed relative to the respective signal yield components in each B charge and bin analogously to the equations in the global fit Section 6.2.2.

3. A combinatorial background yield component is floated independently for each category resulting in 24 variables.

4. A total partially reconstructed background yield component for $B^{\pm}$ and $\overset{(-)}{B^0}$ decays with correctly identified bachelor, is floated in each category, resulting in 24 variables. The relative partially reconstructed background yields are fixed to those obtained in the global invariant mass fit and corrected for the reduced mass range.

For the $DK^{\pm}$ category there are 3 further yield components:

1. A total misidentified partially reconstructed background yield component, where the bachelor pion is reconstructed as a kaon, in each category. The yield in each category is fixed relative to the respective floating total $B^{\pm} \to D\pi^{\pm}$ partially reconstructed background yield (with correctly identified bachelor) in each category, analogously to the equations in the global fit Section 6.3.5. The relative misidentified partially reconstructed background yields are fixed to those obtained in the global invariant mas fit and corrected for the reduced mass range.

2. A partially reconstructed $B_s^0 \to D^0 K^{\pm}[\pi^{\mp}]$ background component is fixed relative to its total yield in the global invariant mass fit, split in half for B charge and distributed across the bins using the F_i parameters and $\bar{F_i}$ parameters for the positive and negative B charges respectively. This component is treated separately due to the K^- bachelor being predominantly produced with $\bar{D^0}$ mesons such that $B_s^0 \to \bar{D}^0[\pi^+]K^-$, and the K^+ bachelor being predominantly produced with D^0 meson such that $\bar{B}_s^0 \to D^0[\pi^-]K^+$ .This is the opposite to the other background and signal decays where the bachelor K^- bachelor is predominantly produced with a D^0 meson, and the K^+ bachelor is predominantly produced with a $\bar{D^0}$ meson

3. A charmless background yield component is fixed in each category from separate fits to the D mass upper side band in the $DK^{\pm}$ data for each B charge and bin.

7.1.1 Signal yield parametrisation

The signal yields in each bin and their relation to $x_{\pm}^{DK,D\pi}$,$y_{\pm}^{DK,D\pi}$,$x_{\xi}^{D\pi}$, y_{ξ}^{DK}, F_i, c_i and s_i were motivated and defined in Section 2.4 with Equations 2.45, 2.46, 2.49, 2.50, 2.54, 2.55. We use these equations to relate the number of signal events in each category and the CP observables to the floating signal yields within the CP fit using

$$N^{\pm}_{mode,i} = \frac{n^{\pm}_{mode,i}}{\sum_j n^{\pm}_{mode,i}} \times N^{\pm}_{mode,total}, \tag{7.1}$$

where the superscript $\pm$ refers to the charge of the reconstructed B meson candidate, the subscript $mode$ refers to the decay mode (either DK or $D\pi$), the subscript i refers to the bin number in the $D \to 2\pi^+2\pi^-$ decay phase space, and subscript $total$ indicates the sum over all D decay phase space bins i. The number of signal events in each category is denoted $N^{\pm}_{mode,i}$, and the total floating yield for each decay mode and B charge across all the D decay bins is denoted $N^{\pm}_{mode,total}$. Equations 2.45, 2.46, 2.49, 2.50 in Section 2.4 are reparametrised as $n^{\pm}_{mode,i}$ defined by

$$n^{\pm}_{mode,i} = F_{\mp i} + [(x^{mode}_{\pm})^2 + (y^{mode}_{\pm})^2]F_{\pm i} + 2\sqrt{F_i F_{-i}}(c_i x^{mode}_{\pm} \mp s_i y^{mode}_{\pm}). \tag{7.2}$$

The $x^{DK}_{\pm}$ and $y^{DK}_{\pm}$ observables are floated and shared between all categories (since $x^{D\pi}_{\pm}$ and $y^{D\pi}_{\pm}$ also rely on $x^{DK}_{\pm}$ and $y^{DK}_{\pm}$ in Equations 2.54 and 2.55) . The $x^{D\pi}_{\pm}$ and $y^{D\pi}_{\pm}$ parameters are fixed in relation to $x^{DK}_{\pm}$, $y^{DK}_{\pm}$ as well as nuisance parameters $x^{D\pi}_{\xi}$ and $y^{D\pi}_{\xi}$ using Equations 2.54 and 2.55 , which are floated and shared across the B charges and D decay bins in the $D\pi$ mode. The c_i and s_i parameters are used as inputs from a measurement using CLEO-c data [36] and shared between all categories. Finally, the $F_{\pm i}$ parameters are floated and shared between all categories however, they are parameterised in terms of recursive fractions as laid out in Section 7.1.2 in order to improve fit stability.

7.1.2 F_i reparametrisation

The F_i parameters must satisfy $0 \le F_i \le 1$ and $\sum_i F_i = 1$. However, if the F_i parameters are constrained between 0 and 1 and are all floating, apart from $F_j = 1 - \sum_{i \neq j} F_i$, it can result in unstable fits with large correlation coefficients. Reparametrising the F_i in terms of floating recursive fractions R_i, satisfying $0 \le R_i \le 1$, addresses this:

$$R_i = \begin{cases} F_i, & i = -N \\ F_i / \sum_{j \ge i} F_j, & -N < i < N \end{cases} \tag{7.3}$$

for bin numbers $-N$ to N, except 0, there are $2N-1$ recursive fractions defined as only that number of F_i parameters are independent. Thus F_i is reparametrised as:

$$F_i = \begin{cases} R_i, & i = -N \\ R_i \prod_{j<i}(1-R_j), & -N < i < N \\ \prod_{j<i}(1-R_j), & i = N \end{cases} . \tag{7.4}$$

7.1.3 2 Step Fit

The CP fit is undertaken in 2 steps to deal with instances where specific background yields in the bins are very low, as values floating towards the limit can cause a problem in the fit when establishing an accurate error matrix. The first step is a fit in which all the yield parameters are floating. This is used to identify if any combinatorial or partially reconstructed reconstructed backgrounds have yields within a bin less than 1. In the second step, any background yields within the bins identified in the first step as meeting the low yield criterion are fixed to 0 and a second fit performed. This two step process is used to ensure stable fits with an accurate error matrix.

7.1.4 CP fit mass range

The mass fit range in the CP fit $5150\ MeV < M_B < 5800\ MeV$ is reduced compared to the global fit. The shapes for the PDFs in the CP fit are fixed from the invariant global mass fit and, the assumption the low mass background shapes is the same in each bin is more reliable when the lower mass range bound is increased from 5080 MeV to 5150 MeV.

7.2 CP Fit Results

The CP observables determined in the fit are given in Table 7.1 and their statistical correlation matrix is shown in Table 7.2. The F_i parameters established in the fit are shown in Table 7.3. The results show $(x_+^{DK}, y_+^{DK}) \neq (x_-^{DK}, y_-^{DK})$ which is an indication of CP violation.

Table 7.1: CP Observable fit results (statistical uncertainties only).

Parameter	Fit result ($\times 10^{-2}$)
x_-^{DK}	6.8 ± 6.2
y_-^{DK}	5.7 ± 7.4
x_+^{DK}	-9.8 ± 4.6
y_+^{DK}	15.0 ± 7.4
$x_\xi^{D\pi}$	-1.1 ± 1.0
$y_\xi^{D\pi}$	5.0 ± 1.1

The CP asymmetry of the phase-space integrated yields is large enough to be observed in some individual bin pairs. This is demonstrated in Figure 7.1, where it is evident CP violation is present when comparing the fit projections for the $B^+ \to D(\to 2\pi^+2\pi^-)K^+$ decay in bin -2, and the $B^- \to D(\to 2\pi^+2\pi^-)K^-$ decays in bin +2. The invariant B mass fit projection plots are laid out in their entirety in individual bin pairs in Figures 7.2, 7.3 and 7.4.

Table 7.2: Statistical correlations of the CP observables.

	x_-^{DK}	y_-^{DK}	$x_+^{D\pi}$	$y_+^{D\pi}$	$x_\xi^{D\pi}$	$y_\xi^{D\pi}$
x_-^{DK}	1.000	-0.288	0.060	0.074	-0.033	-0.308
y_-^{DK}	-0.288	1.000	-0.049	0.020	0.327	0.065
$x_+^{D\pi}$	0.060	-0.049	1.000	-0.223	-0.004	-0.015
$y_+^{D\pi}$	0.074	0.020	-0.223	1.000	0.038	-0.320
$x_\xi^{D\pi}$	-0.033	0.327	-0.004	0.038	1.000	-0.266
$y_\xi^{D\pi}$	-0.308	0.065	-0.015	-0.320	-0.266	1.000

Table 7.3: The F_i parameter fit results.

Bin Number	F_i	F_{-i}
1	0.1991 $\pm$0.0026	0.0993 $\pm$0.0022
2	0.2901 $\pm$0.0036	0.2056 $\pm$0.0031
3	0.1249 $\pm$0.0028	0.0809 $\pm$0.0026

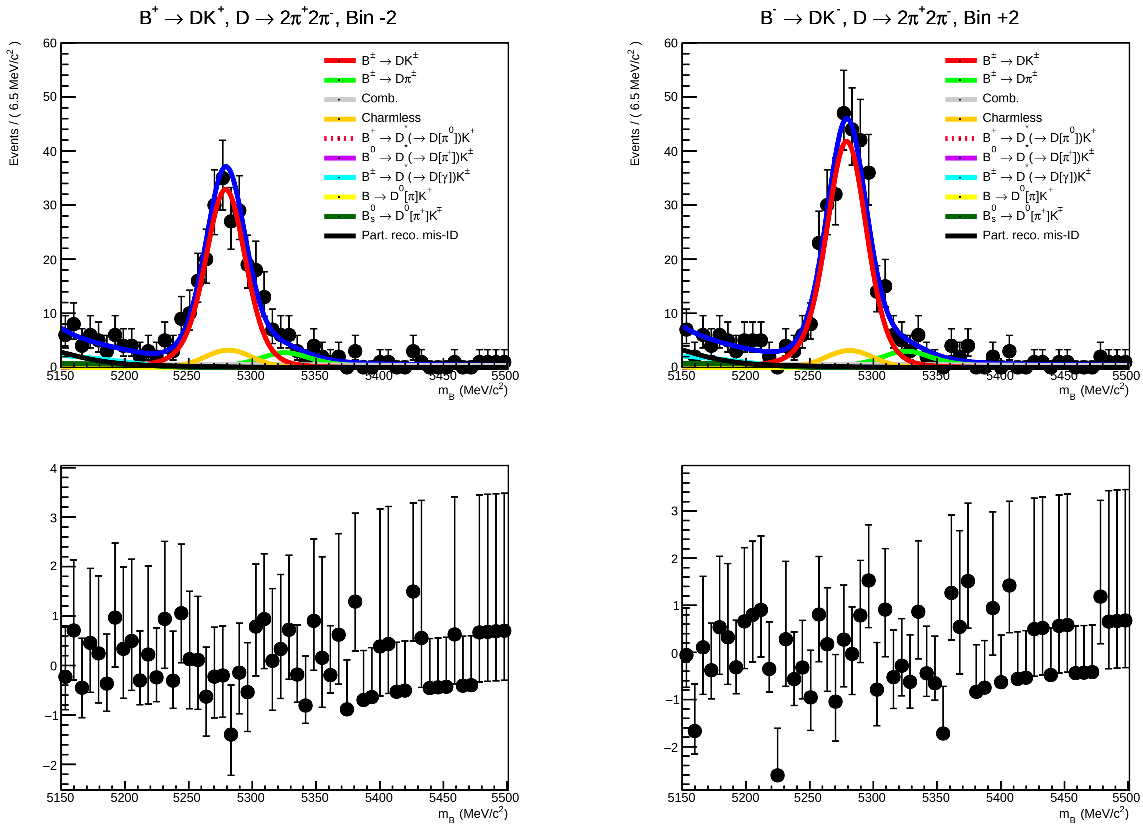

FIGURE 7.1. Top: the invariant B mass distributions of $B^+ \to D(\to 2\pi^+2\pi^-)K^+$ in bin -2 (left) and $B^- \to D(\to 2\pi^+2\pi^-)K^-$ in bin +2 (right). Bottom: The respective distribution of pulls for each of the invariant mass distributions above.

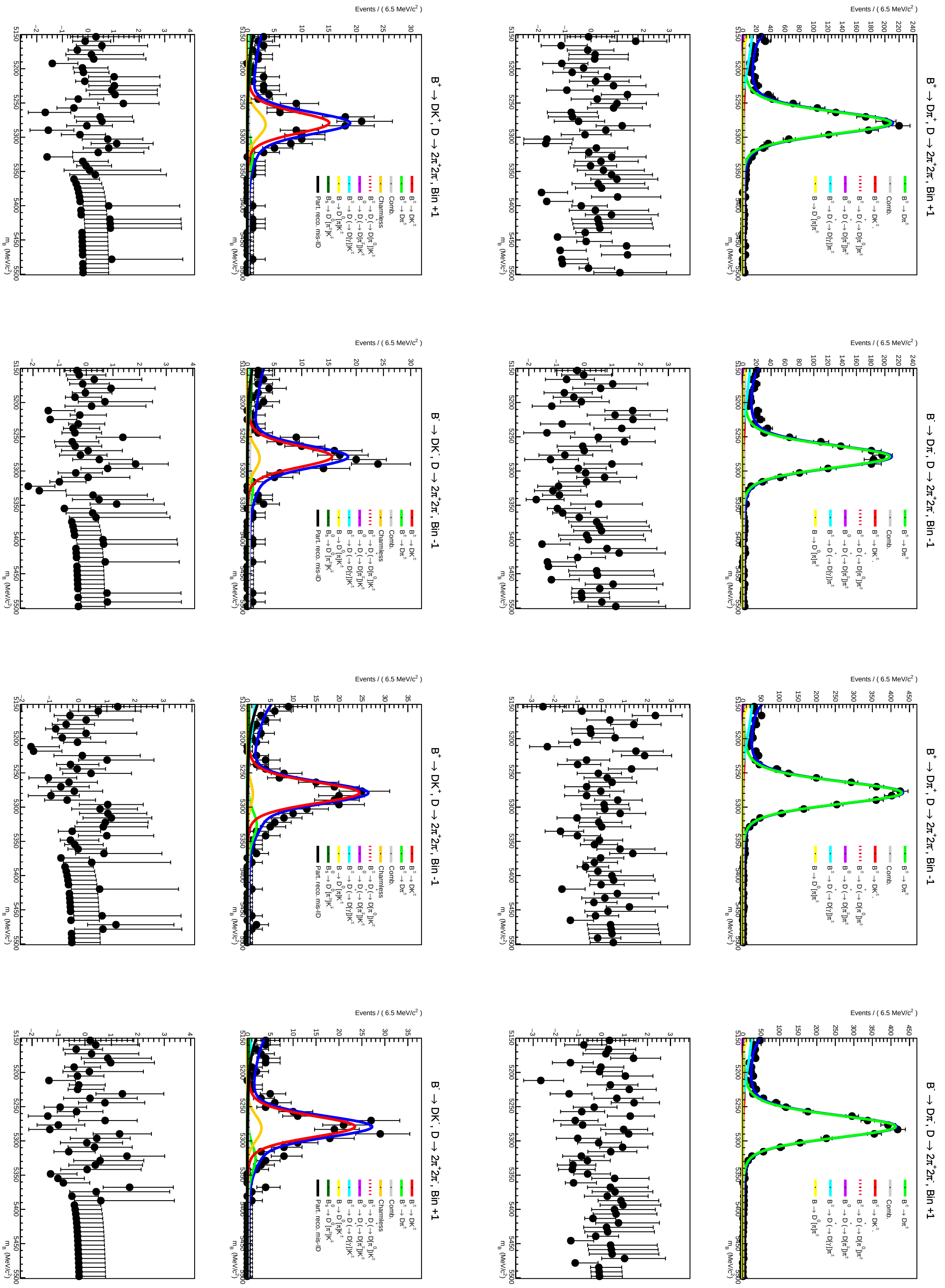

Figure 7.2: The invariant B mass projections from the fit for the CP observables and their respective pull distributions. The 2 columns on the left are the $B^{\pm} \to D(\to 2\pi^{+}2\pi^{-})K^{\pm}$ decays. The 2 columns on the right are the $B^{\pm} \to D(\to 2\pi^{+}2\pi^{-})\pi^{\pm}$ decays.

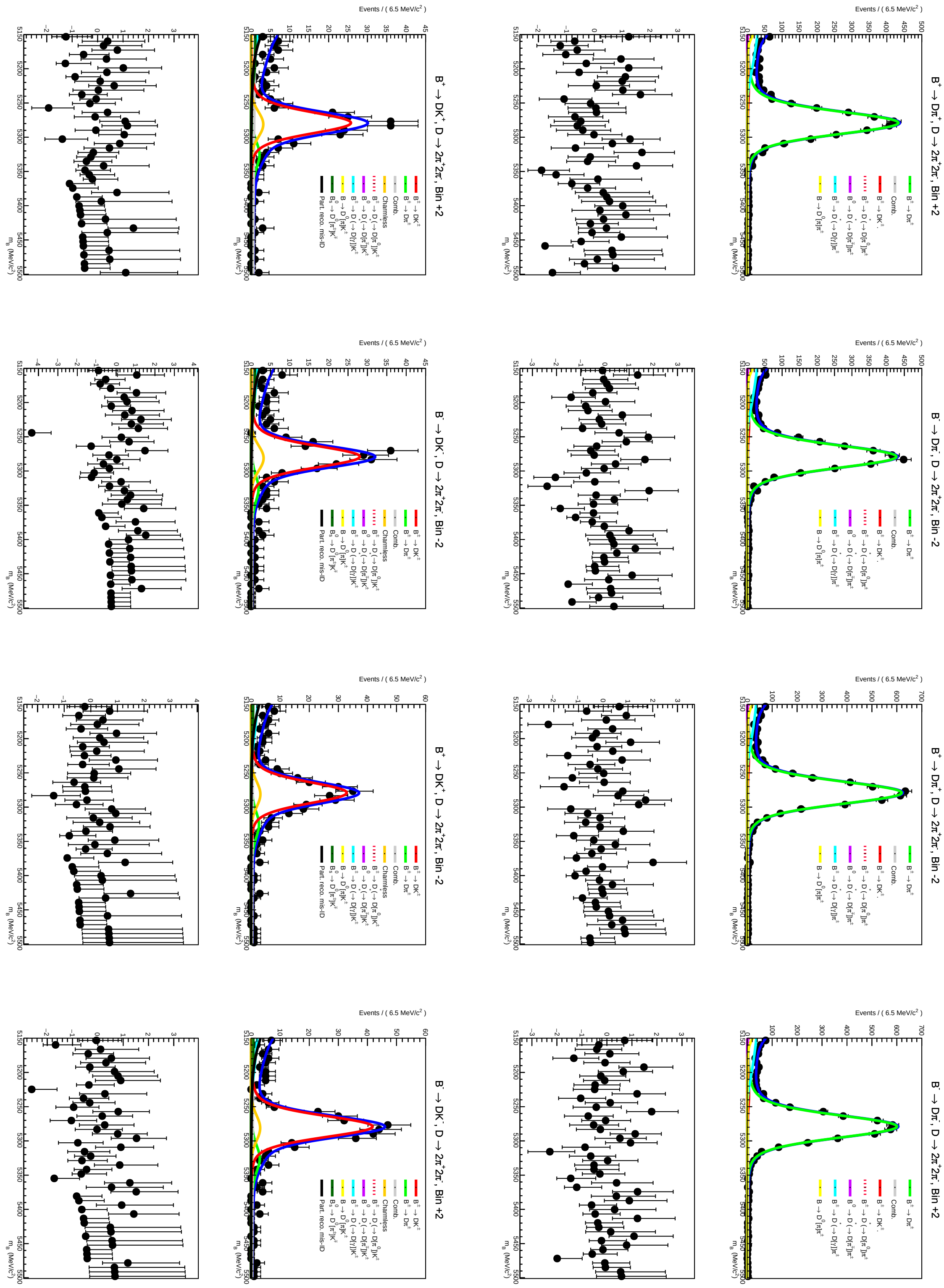

Figure 7.3: The invariant B mass projections from the fit for the CP observables and their respective pull distributions. The 2 columns on the left are the $B^{\pm} \rightarrow D(\rightarrow 2\pi^{+}2\pi^{-})K^{\pm}$ decays. The 2 columns on the right are the $B^{\pm} \rightarrow D(\rightarrow 2\pi^{+}2\pi^{-})\pi^{\pm}$ decays.

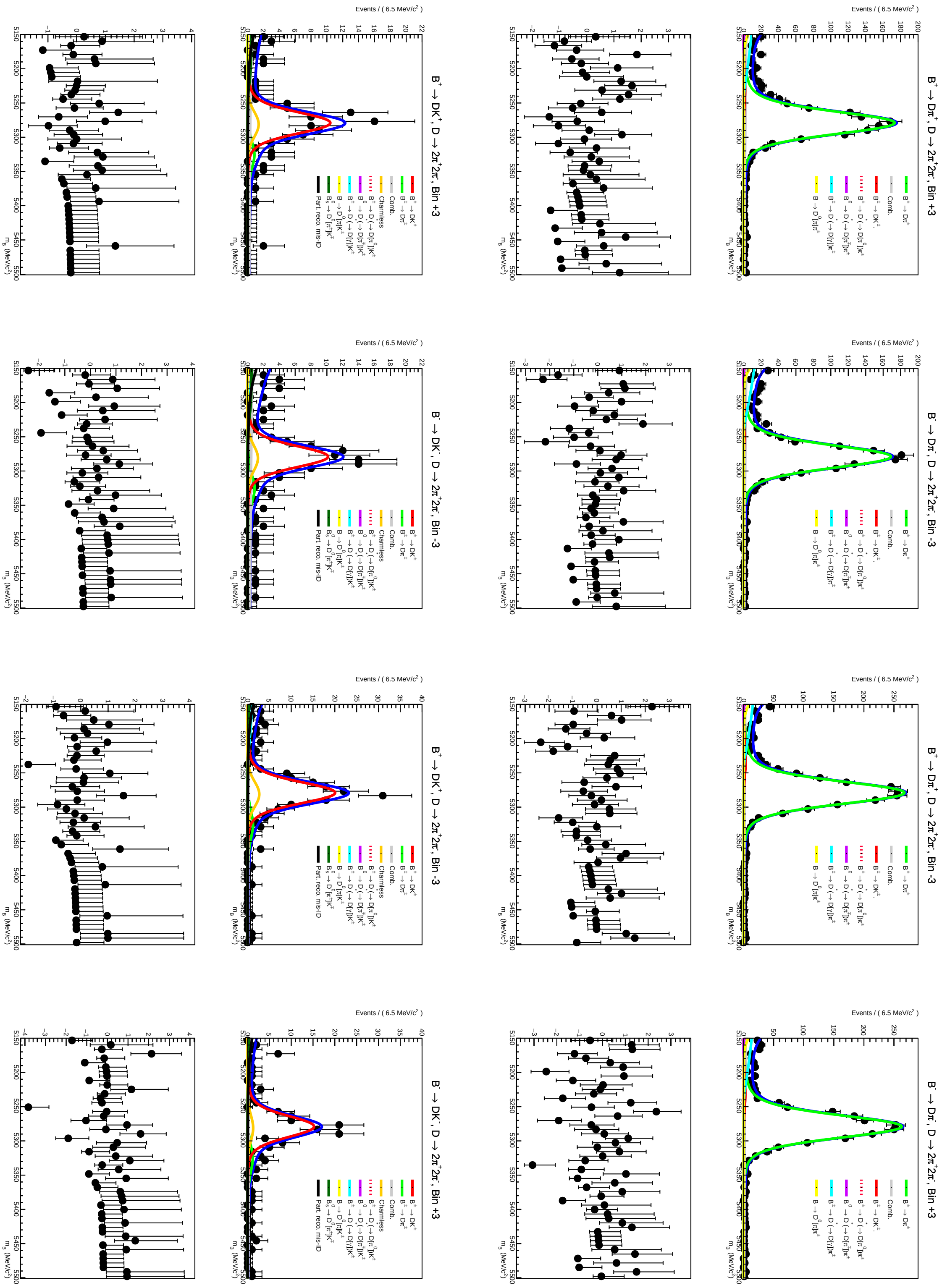

Figure 7.4: The invariant B mass projections from the fit for the CP observables and their respective pull distributions. The 2 columns on the left are the $B^{\pm} \to D(\to 2\pi^{+}2\pi^{-})K^{\pm}$ decays. The 2 columns on the right are the $B^{\pm} \to D(\to 2\pi^{+}2\pi^{-})\pi^{\pm}$ decays.

CHAPTER 8

CKM ANGLE γ RESULT

8.1 BPGGSZ measurement

The CP observables obtained in the CP fit $x_{\pm}^{DK}$, $y_{\pm}^{DK}$, $x_{\xi}^{D\pi}$ and $y_{\xi}^{D\pi}$ are used to determine CKM angle γ and the hadronic nuisance parameters δ_B^{DK}, r_B^{DK},$\delta_B^{D\pi}$, $r_B^{D\pi}$, as well as their confidence intervals using the profile likelihood method ($PROB$) of the $GammaCombo$ package [89]. The results for the physics parameters are

$$\begin{aligned}
\gamma &= (38.8^{+30}_{-22})^{\circ}, \\
\delta_B^{DK} &= (86.9^{+23}_{-31})^{\circ}, \\
r_B^{DK} &= 0.1296^{+0.046}_{-0.045}, \\
\delta_B^{D\pi} &= (168.8^{+89}_{-112})^{\circ}, \\
r_B^{D\pi} &= 0.0078^{+0.015}_{-0.031},
\end{aligned} \tag{8.1}$$

and the corresponding correlation matrix is outlined in Table 8.1.

The one-dimensional confidence level projections of the measurement parameters are shown in Figure 8.1, and two-dimensional confidence regions are plotted in Figure 8.2. The physical range for the $r_B^{D\pi}$ observable in Figure 8.1 (d) is from zero upwards, however the scan is allowed to show negative values in order to observe the shape of the contour and ensure calculations of the uncertainties for the observables are correct. The unphysical negative $r_B^{D\pi}$ solution is due to the degeneracy in the equations. The measured value of γ is within 1σ of the current LHCb combination [27].

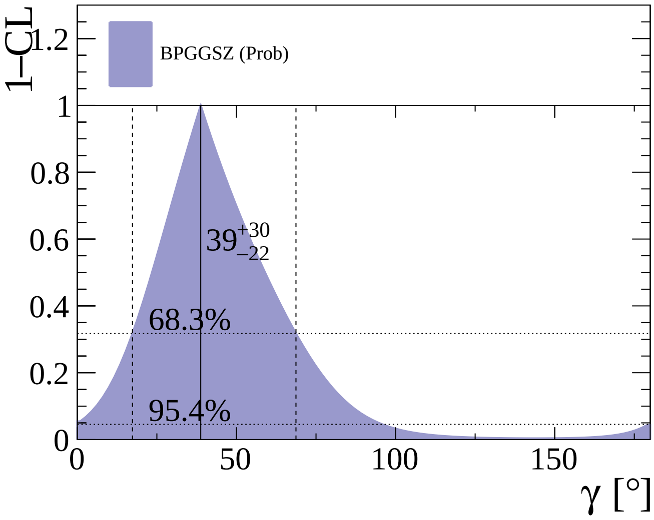

(a) Confidence levels for γ.

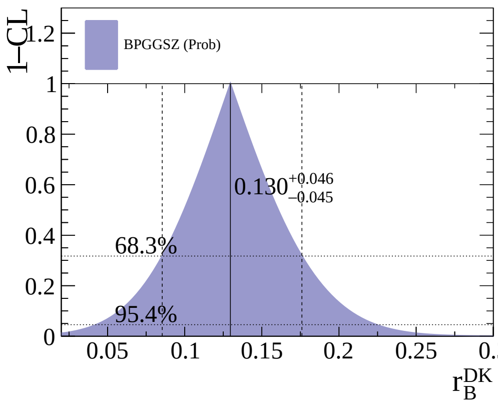

(b) Confidence levels for r_B^{DK}.

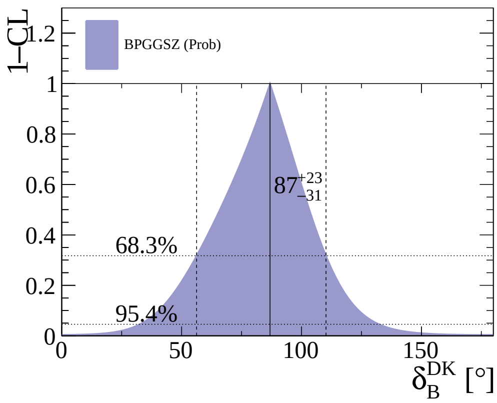

(c) Confidence levels for δ_B^{DK}.

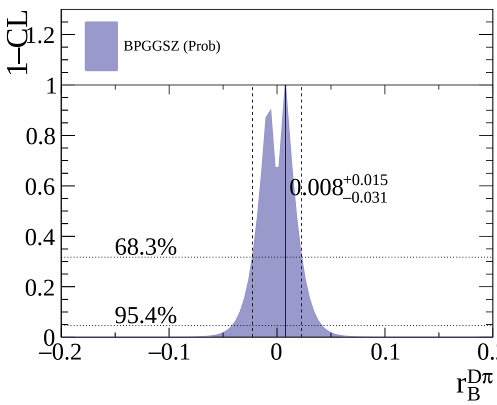

(d) Confidence levels for $r_B^{D\pi}$.

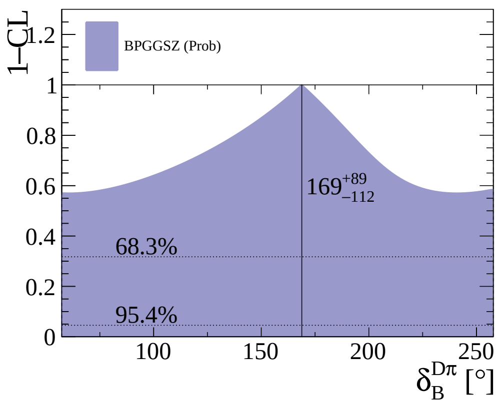

(e) Confidence levels for $\delta_B^{D\pi}$.

Figure 8.1: The one-dimensional confidence levels for each of the measured physics parameters. The solutions are written on the plots with the $PROB$ uncertainties.

Table 8.1: Statistical correlations of the measured physics parameters.

	γ	δ_B^{DK}	r_B^{DK}	$\delta_B^{D\pi}$	$r_B^{D\pi}$
γ	1.000	-0.768	-0.299	0.075	0.331
δ_B^{DK}	-0.768	1.000	0.167	0.048	-0.457
r_B^{DK}	-0.299	0.167	1.000	-0.242	-0.011
$\delta_B^{D\pi}$	0.074	0.048	-0.242	1.000	-0.288
$r_B^{D\pi}$	0.331	-0.457	-0.011	-0.288	1.000

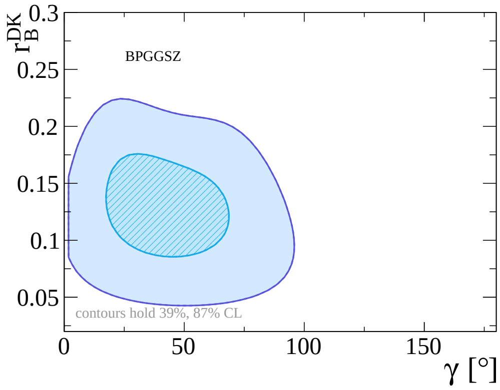

(a) Confidence regions for γ vs r_B^{DK}.

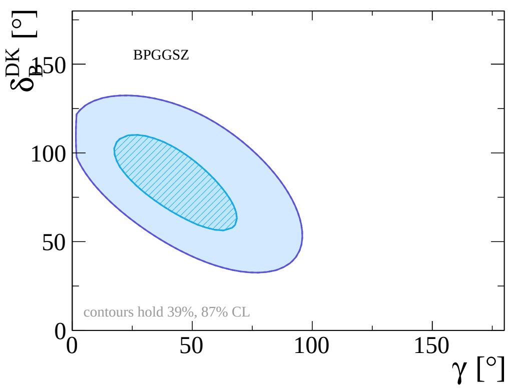

(b) Confidence regions for γ vs δ_B^{DK}.

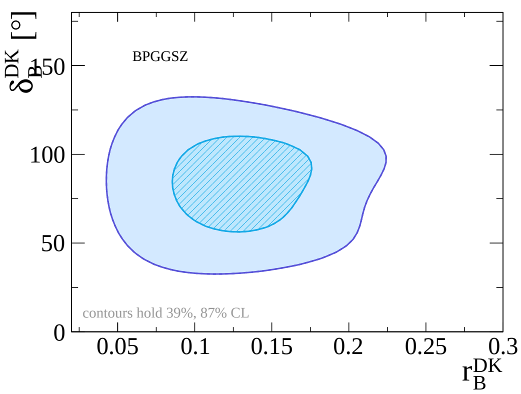

(c) Confidence regions for r_B^{DK} vs δ_B^{DK}.

Figure 8.2: The two-dimensional confidence regions for combinations of the measured physics parameters, determined using the $PROB$ method.

CHAPTER 9

FUTURE PROSPECTS

Systematic effects such as those listed below will be considered and then evaluated and a systematic uncertainty assigned accordingly if required:

- The uncertainties on the c_i and s_i values.
- The invariant mass shapes used in the global and CP mass fits.
- The assumption that there is no CP violation in the partially reconstructed backgrounds.
- The floating fraction of relative yields in the global mass fit.
- The PID efficiencies.
- The fixed Charmless background yields.
- The use of the $K_s^0\pi^+\pi^-$ for the modelling of the partially reconstructed backgrounds including not being reweighted by the D amplitude model.
- The impact of D mixing.
- The $B^\pm \to D\mu^\pm\nu_\mu$ Background.
- Bin migration.
- Phase space efficiencies. The $B^\pm \to DK^\pm$ and $B^\pm \to D\pi^\pm$ modes share the identical F_i parameters which is only true if the phase space efficiencies are the same. Also, the phase space acceptance for D^0 and $\bar{D}^0$ decays need to be identical for the $F_i = -F_i$ assumption to hold.

- Ignoring low mass physics effects.
- The fit bias systematic.

The measurement will be performed for the full Run 1 and Run 2 data samples and systematics evaluated. It is expected the measurement will remain statistically limited. Once completed the full analysis will be published following approval by the LHCb collaboration.

Chapter 10

Conclusion

The LHCb 2017 samples of $B^\pm \to DK^\pm$ and $B^\pm \to D\pi^\pm$ decays, where D is a superposition of D^0 and $\bar{D}^0$ and $D \to 2\pi^+2\pi^-$, are used to perform a model-independent BPGGSZ measurement of the CKM angle γ and its related hadronic parameters. The CP observables determined are

$$\begin{aligned}
x_-^{DK} &= (6.8 \pm 6.2) \times 10^{-2} \\
y_-^{DK} &= (5.7 \pm 7.4) \times 10^{-2} \\
x_+^{DK} &= (-9.8 \pm 4.6) \times 10^{-2} \\
y_+^{DK} &= (15.0 \pm 7.4) \times 10^{-2} \\
x_\xi^{D\pi} &= (-1.1 \pm 1.0) \times 10^{-2} \\
y_\xi^{D\pi} &= (5.0 \pm 1.1) \times 10^{-2}
\end{aligned} \tag{10.1}$$

where the uncertainty is statistical only. These CP observables are used to calculate the CKM angles γ and the related hadronic decay parameters resulting in

$$\begin{aligned}
\gamma &= (38.8^{+30}_{-22})^\circ, \\
\delta_B^{DK} &= (86.9^{+23}_{-31})^\circ, \\
r_B^{DK} &= 0.1296^{+0.046}_{-0.045}, \\
\delta_B^{D\pi} &= (168.8^{+89}_{-112})^\circ, \\
r_B^{D\pi} &= 0.0078^{+0.015}_{-0.031},
\end{aligned} \tag{10.2}$$

This is the first model independent BPGGSZ measurement of γ in the $D \to 2\pi^+2\pi^-$ mode. The measurement of the CKM angle γ is within 1σ of the current LHCb combination [27] and thus consistent with the LHCb combination. The statistical sensitivity is expected to increase once the measurement is performed with additional LHCb Run 1 and remaining Run 2 data samples.

Bibliography

[1] Serguei Chatrchyan et al.
Observation of a New Boson at a Mass of 125 GeV with the CMS Experiment at the LHC.
Phys. Lett. B, 716:30–61, 2012.

[2] Georges Aad et al.
Observation of a new particle in the search for the Standard Model Higgs boson with the ATLAS detector at the LHC.
Phys. Lett. B, 716:1–29, 2012.

[3] B. Adeva et al.
Roadmap for selected key measurements of LHCb.
12 2009.

[4] Nicola Cabibbo.
Unitary Symmetry and Leptonic Decays.
Phys. Rev. Lett., 10:531–533, 1963.

[5] Makoto Kobayashi and Toshihide Maskawa.
CP Violation in the Renormalizable Theory of Weak Interaction.
Prog. Theor. Phys., 49:652–657, 1973.

[6] Joachim Brod and Jure Zupan.
The ultimate theoretical error on γ from $B \to DK$ decays.
JHEP, 01:051, 2014.

[7] Joachim Brod, Alexander Lenz, Gilberto Tetlalmatzi-Xolocotzi, and Martin Wiebusch.
New physics effects in tree-level decays and the precision in the determination of the quark mixing angle γ.
Phys. Rev. D, 92(3):033002, 2015.

[8] Alexander Lenz and Gilberto Tetlalmatzi-Xolocotzi.
Model-independent bounds on new physics effects in non-leptonic tree-level decays of B-mesons.
JHEP, 07:177, 2020.

[9] Robert B. Mann.
An introduction to particle physics and the standard model.
CRC Press, Boca Raton, FL, 2010.

[10] F. Halzen and Alan D. Martin.
QUARKS AND LEPTONS: AN INTRODUCTORY COURSE IN MODERN PARTICLE PHYSICS.
1984.

[11] Mark Thomson.
Modern particle physics.
Cambridge University Press, New York, 2013.

[12] Michael E. Peskin and Daniel V. Schroeder.
An Introduction to quantum field theory.
Addison-Wesley, Reading, USA, 1995.

[13] Paul Langacker.
Introduction to the Standard Model and Electroweak Physics.
In *Theoretical Advanced Study Institute in Elementary Particle Physics: The Dawn of the LHC Era*, pages 3–48, 2010.

[14] Gerhart Luders.
On the Equivalence of Invariance under Time Reversal and under Particle-Antiparticle Conjugation for Relativistic Field Theories.
Kong. Dan. Vid. Sel. Mat. Fys. Med., 28N5(5):1–17, 1954.

[15] C. S. Wu, E. Ambler, R. W. Hayward, D. D. Hoppes, and R. P. Hudson.
Experimental Test of Parity Conservation in β Decay.
Phys. Rev., 105:1413–1414, 1957.

[16] R. Aaij et al.
Observation of CP violation in $B^{\pm} \to DK^{\pm}$ decays.
Phys. Lett. B, 712:203–212, 2012.
[Erratum: Phys.Lett.B 713, 351 (2012)].

[17] T. D. Lee and Chen-Ning Yang.
Question of Parity Conservation in Weak Interactions.
Phys. Rev., 104:254–258, 1956.

[18] J. H. Christenson, J. W. Cronin, V. L. Fitch, and R. Turlay.
Evidence for the 2π Decay of the K_2^0 Meson.
Phys. Rev. Lett., 13:138–140, 1964.

[19] Bernard Aubert et al.
Observation of CP violation in the B^0 meson system.
Phys. Rev. Lett., 87:091801, 2001.

[20] Kazuo Abe et al.
Observation of large CP violation in the neutral B meson system.
Phys. Rev. Lett., 87:091802, 2001.

[21] R Aaij et al.
First observation of CP violation in the decays of B_s^0 mesons.
Phys. Rev. Lett., 110(22):221601, 2013.

[22] A. D. Sakharov.
Violation of CP Invariance, C asymmetry, and baryon asymmetry of the universe.
Pisma Zh. Eksp. Teor. Fiz., 5:32–35, 1967.

[23] Antonio Riotto.
Theories of baryogenesis.
In *ICTP Summer School in High-Energy Physics and Cosmology*, pages 326–436, 7 1998.

[24] Ling-Lie Chau and Wai-Yee Keung.
Comments on the Parametrization of the Kobayashi-Maskawa Matrix.
Phys. Rev. Lett., 53:1802, 1984.

[25] R. L. Workman et al.
Review of Particle Physics.
PTEP, 2022:083C01, 2022.

[26] Lincoln Wolfenstein.
Parametrization of the Kobayashi-Maskawa Matrix.
Phys. Rev. Lett., 51:1945, 1983.

[27] Roel Aaij et al.
Simultaneous determination of CKM angle γ and charm mixing parameters.
JHEP, 12:141, 2021.

[28] J. Charles et al.
Current status of the Standard Model CKM fit and constraints on $\Delta F = 2$ New Physics.
Phys. Rev. D, 91(7):073007, 2015, updated results and plots available at: http://ckmfitter.in2p3.fr/.

[29] R. Aaij et al.
Measurement of the CKM angle γ in $B^\pm \to DK^\pm$ and $B^\pm \to D\pi^\pm$ decays with $D \to K_S^0 h^+ h^-$.
JHEP, 02:169, 2021.

[30] Anjan Giri, Yuval Grossman, Abner Soffer, and Jure Zupan.
Determining γ using $B^{\pm} \rightarrow DK^{\pm}$ with multibody D decays.
Phys. Rev. D, 68:054018, 2003.

[31] A. Poluektov et al.
Measurement of ϕ_3 with Dalitz plot analysis of $B^{\pm} \rightarrow D^{**(*)}K^{\pm}$ decay.
Phys. Rev. D, 70:072003, 2004.

[32] A. Bondar.
Proceedings of BINP special analysis meeting on Dalitz analysis, 24–26 Sep. 2002, unpublished.

[33] A. Bondar and A. Poluektov.
Feasibility study of model-independent approach to phi(3) measurement using Dalitz plot analysis.
Eur. Phys. J. C, 47:347–353, 2006.

[34] David Atwood, Isard Dunietz, and Amarjit Soni.
Enhanced CP violation with B —> K D0 (anti-D0) modes and extraction of the CKM angle gamma.
Phys. Rev. Lett., 78:3257–3260, 1997.

[35] Michael Gronau and David London.
How to determine all the angles of the unitarity triangle from B(d)0 —> D K(s) and B(s)0 —> D0.
Phys. Lett. B, 253:483–488, 1991.

[36] Samuel Harnew, Paras Naik, Claire Prouve, Jonas Rademacker, and David Asner.
Model-independent determination of the strong phase difference between D^0 and $\bar{D}^0 \rightarrow \pi^+\pi^-\pi^+\pi^-$ amplitudes.
JHEP, 01:144, 2018.

[37] Matthew Kenzie, Maurizio Martinelli, and Niels Tuning.
Estimating $r_B^{D\pi}$ as an input to the determination of the CKM angle γ.
Phys. Rev. D, 94(5):054021, 2016.

[38] The LHCb Collaboration, A Augusto Alves Jr, L M Andrade Filho, A F Barbosa, I Bediaga, G Cernicchiaro, G Guerrer, H P Lima Jr, A A Machado, and J Magnin.
The LHCb detector at the LHC.
Journal of Instrumentation, 3(08):S08005, 2008.

[39] Esma Mobs.
The CERN accelerator complex. Complexe des accélérateurs du CERN.

https://cds.cern.ch/record/2197559, 2016.

[40] The LHCb Collaboration.
Lhcb letter of intent.
Technical Report LHCC-95-5, CERN, August 1995.

[41] Christian Elsässer.
$\bar{b}b$ production angle plots.

[42] The LHCb Collaboration.
LHCb Vertex Locator Technical Design Report.
Technical Design Report LHCC-2001-011, CERN, May 2001.

[43] The LHCb Collaboration.
LHCb Magnet Technical Design Report.
Technical Report CERN-LHCC-2000-007, CERN, January 2000.

[44] The LHCb Collaboration.
LHCb Inner Tracker Technical Design Report.
Technical Report CERN-LHCC-2002-029, CERN, November 2002.

[45] The LHCb Collaboration.
LHCb Outer Tracker Technical Design Report.
Technical Report CERN-LHCC-2001-024, CERN, September 2001.

[46] LHCb Collaboration.
LHCb detector performance.
International Journal of Modern Physics A, 30(22):1530022, 2015.

[47] R. Fruhwirth.
Application of Kalman filtering to track and vertex fitting.
Nucl. Instrum. Meth. A, 262:444–450, 1987.

[48] The LHCb Collaboration.
LHCb RICH Technical Design Report.
Technical Report CERN-LHCC-2000-037, CERN, September 2000.

[49] William R. Leo.
Techniques for Nuclear and Particle Physics Experiments.
Springer-Verlag, Berlin, Heidelberg, New York, 1987.

[50] The LHCb Collaboration.
LHCb Calorimeters Technical Design Report.
Technical Report CERN-LHCC-2000-036, CERN, September 2000.

[51] The LHCb Collaboration.
LHCb Muon System Technical Design Report.
Technical Report CERN-LHCC-2001-010, CERN, 5 2001.

[52] Alessandro Cardini, Giovanni Bencivenni, and Patrizia De Simone.
The Operational Experience of the Triple-GEM Detectors of the LHCb Muon System: Summary of 2 Years of Data Taking.
Technical Report LHCb-PROC-2012-060, CERN, 11 2012.

[53] L. Anderlini et al.
Computing strategy for PID calibration samples for LHCb Run 2.
Technical Report LHCb-PUB-2016-020, CERN, 2016.

[54] LHCb collaboration.
Trigger schemes.
`http://lhcb.web.cern.ch/lhcb/speakersbureau/html/TriggerScheme.html`.

[55] R. Aaij et al.
The LHCb trigger and its performance in 2011.
JINST, 8:P04022, 2013.

[56] J. Albrecht, V. V. Gligorov, G. Raven, and S. Tolk.
Performance of the LHCb high level trigger in 2012.
J. Phys.: Conf. Ser., 513:012001, 2014.

[57] R. Aaij et al.
Performance of the LHCb trigger and full real-time reconstruction in run 2 of the LHC.
JINST, 14:P04013, 2019.

[58] Tatiana Likhomanenko, Philip Ilten, Egor Khairullin, Alex Rogozhnikov, Andrey Ustyuzhanin, and Michael Williams.
LHCb Topological Trigger Reoptimization.
J. Phys. Conf. Ser., 664(8):082025, 2015.

[59] V. V. Gligorov and Mike Williams.
Efficient, reliable and fast high-level triggering using a bonsai boosted decision tree.
JINST, 8:P02013, 2013.

[60] R. Aaij et al.
Tesla : an application for real-time data analysis in High Energy Physics.
Comput. Phys. Commun., 208:35–42, 2016.

[61] G Barrand, I Belyaev, Y Benhammou, D Breton, M Cattaneo, P Charpentier, M Chmeissani, M Clemencic, G Corti, S Cunliffe, et al.
Gaudi–a software architecture and framework for building HEP data processing applications.
Computer Physics Communications, 140(1-2):45–55, Oct 2001.

[62] G. Corti et al.
Software for the LHCb experiment.
IEEE Transactions on Nuclear Science, 53(3):1323–1329, 2006.

[63] Marco Clemencic et al.
The LHCb simulation application, Gauss: Design, evolution and experience.
Journal of Physics: Conference Series, 331(3):032023, 2011.

[64] Torbjorn Sjostrand, Stephen Mrenna, and Peter Skands.
PYTHIA 6.4 physics and manual.
Journal of High Energy Physics, 2006(05):026, 2006.

[65] Anders Ryd, David J. Lange, et al.
EvtGen, A Monte Carlo Generator for B-Physics.
Technical Report 10781, SLAC-PUB, Feb 2004.

[66] V.N. Ivanchenko.
Geant4 toolkit for simulation of HEP experiments.
Nuclear Instruments and Methods in Physics Research Section A: Accelerators, Spectrometers, Detectors and Associated Equipment, 502(2-3):250–303, Apr 2003.

[67] J. Allison et al.
Geant4 developments and applications.
IEEE Transactions on Nuclear Science, 53(1):270–278, 2006.

[68] The LHCb Collaboration.
The DaVinci Project.
`http://lhcbdoc.web.cern.ch/lhcbdoc/davinci/`.

[69] Claire Prouve.
Measurement of the CP-even Fraction of the $D^0 \to 2\pi^+2\pi^-$ Decay using Quantum Correlated $D\bar{D}$ Pairs at CLEO-c, and Real-time Alignment of the LHCb RICH optical Systems, 2017.
Thesis, University of Bristol.

[70] R Aaij et al.

Observation of double charm production involving open charm in pp collisions at $\sqrt{s} = 7$ TeV.
JHEP, 06:141, 2012.
[Addendum: JHEP 03, 108 (2014)].

[71] Roel Aaij et al.
A study of CP violation in $B^{\mp} \to Dh^{\mp}$ $(h = K, \pi)$ with the modes $D \to K^{\mp}\pi^{\pm}\pi^{0}$, $D \to \pi^{+}\pi^{-}\pi^{0}$ and $D \to K^{+}K^{-}\pi^{0}$.
Phys. Rev. D, 91(11):112014, 2015.

[72] Roel Aaij, Jessica Prisciandaro, Ricardo Vazquez Gomez, Vasileios Syropoulos, Helder Lopes, Francesco Dettori, Sascha Stahl, Johannes Albrecht, Kevin Dungs, Diego Martinez Santos, et al.
Optimization of the muon reconstruction algorithms for LHCb Run 2.
Technical report, 2017.

[73] Philippe d'Argent, Nicola Skidmore, Jack Benton, Jeremy Dalseno, Evelina Gersabeck, Sam Harnew, Paras Naik, Claire Prouve, and Jonas Rademacker.
Amplitude Analyses of $D^{0} \to \pi^{+}\pi^{-}\pi^{+}\pi^{-}$ and $D^{0} \to K^{+}K^{-}\pi^{+}\pi^{-}$ Decays.
JHEP, 05:143, 2017.

[74] Tatiana Likhomanenko, Philip Ilten, Egor Khairullin, Alex Rogozhnikov, Andrey Ustyuzhanin, and Mike Williams.
LHCb Topological Trigger Reoptimization.
J. Phys. Conf. Ser., 664(8):082025, 2015.

[75] Pascal Geurts and Gilles Louppe.
Learning to rank with extremely randomized trees.
Journal of Machine Learning Research - Proceedings Track, 14:49–61, 01 2011.

[76] Wouter D. Hulsbergen.
Decay chain fitting with a Kalman filter.
Nuclear Instruments and Methods in Physics Research Section A: Accelerators, Spectrometers, Detectors and Associated Equipment, 552(3):566–575, nov 2005.

[77] R. L. Workman et al.
Review of Particle Physics.
PTEP, 2022:083C01, 2022.

[78] LHCb Collaboration.
LHCb Doxygen: Ibackgroundcategory class reference.
`https://lhcb-doxygen.web.cern.ch/lhcb-doxygen/davinci/latest/df/d88/class_i_background_category.html`.

[79] Andreas Hocker et al.
TMVA - Toolkit for Multivariate Data Analysis.
3 2007.

[80] Lucio Anderlini et al.
The PIDCalib package.
2016.

[81] Roel Aaij et al.
Selection and processing of calibration samples to measure the particle identification performance of the LHCb experiment in Run 2.
EPJ Tech. Instrum., 6(1):1, 2019.

[82] D. Cervenkov and et al.
PIDCalib2.
`https://gitlab.cern.ch/lhcb-rta/pidcalib2`, 2021.

[83] R. Aaij et al.
A study of *CP* violation in the decays $B^{\pm} \to [K^+K^-\pi^+\pi^-]_D h^{\pm}$ $(h = K, \pi)$ and $B^{\pm} \to [\pi^+\pi^-\pi^+\pi^-]_D h^{\pm}$.
arXiv:2301.10328, 1 2023.

[84] Roger J. Barlow.
Extended maximum likelihood.
Nucl. Instrum. Meth. A, 297:496–506, 1990.

[85] Wouter Verkerke and David P. Kirkby.
The RooFit toolkit for data modeling.
eConf, C0303241:MOLT007, 2003.

[86] Wouter Hulsbergen.
Cruijff PDF Class.
`https://www.slac.stanford.edu/BFROOT/www/doc/workbook_backup_010108/examples/ex1/workdir/PARENT/RooFitBabar/RooCruijff.cc`, 2008.

[87] Roel Aaij et al.
Measurement of *CP* observables in $B^{\pm} \to DK^{\pm}$ and $B^{\pm} \to D\pi^{\pm}$ with two- and four-body D decays.
Phys. Lett. B, 760:117–131, 2016.

[88] Roel Aaij et al.

Measurement of CP observables in $B^\pm \to D^{(*)}K^\pm$ and $B^\pm \to D^{(*)}\pi^\pm$ decays using two-body D final states.
JHEP, 04:081, 2021.

[89] M. Kenzie and et al.
GammaCombo: A statistical analysis framework for combining measurements, fitting datasets and producing confidence intervals.
https://gammacombo.github.io/, 2021.